ArF EXCIMER LASER CORNEAL ABLATION: EFFECTS OF LASER REPETITION RATE AND FUNDAMENTAL LASER-TISSUE COUPLING

By

LEIA MEGAN SHANYFELT

A DISSERTATION PRESENTED TO THE GRADUATE SCHOOL
OF THE UNIVERSITY OF FLORIDA IN PARTIAL FULFILLMENT
OF THE REQUIREMENTS FOR THE DEGREE OF
DOCTOR OF PHILOSOPHY

UNIVERSITY OF FLORIDA

2008

To my husband Dan Shanyfelt

ACKNOWLEDGMENTS

First and foremost, I thank my husband for making my transition back to the University of Florida possible. Mostly, I thank him for his patience and support during less than ideal living circumstances. I am also grateful to my parents for always insisting upon excellence in my academic career.

I am thankful to Dr. Hahn for allowing me to return to his laboratory to obtain my PhD under his advisement. I am appreciative to all of my lab mates for their assistance and friendship over the last few years. So thanks go out to Soupy Dalyander, Prasoon Diwaker, Phil Jackson, Bret Windom and Cary Henry. I would like to specifically thank Cary Henry for his help in harvesting bovine eyes, a less than pleasurable task. Also, I am obliged to Soupy Dalyander for all of her Matlab help and to Prasoon Diwaker for his patient help with the imaging study.

Additionally, I am appreciative to Dr. Pam Dickrell for her many hours of assistance with the white-light interferometry measurements and to Dr. Greg Sawyer for the use of his interferometer and mass spectrometer. I am also indebted to Dr. Hank Edelhauser for his creation of the microscopy images. Also thanks go out to Dr. George Pettit and Alcon for supporting this research with resources, algorithms, discussion and input.

TABLE OF CONTENTS

page

LIST OF TABLES

LIST OF FIGURES

LIST OF ABBREVIATIONS

amu	Atomic Mass Units
APD	Ablative Photodecomposition
ArF	Argon Fluoride Laser
ECM	Extracellular Matrix
H&E	Hematoxylin and Eosin
LASIK:	Laser Assisted In-Situ Keratomileusis
MMA	Methyl Methacrylate
PET	Poly(Ethylene Terephthalate)
PMMA	Poly(Methyl Methacrylate)
ppb	Parts Per Billion
PRK:	Photo-Refractive Keratectomy
SEM	Scanning Electron Microscopy
TEM	Transmission Electron Microscopy
TC	Tropocollagen
UV	Ultraviolet

Abstract of Dissertation Presented to the Graduate School
of the University of Florida in Partial Fulfillment of the
Requirements for the Degree of Doctor of Philosophy

ArF EXCIMER LASER CORNEAL ABLATION: EFFECTS OF LASER REPETITION RATE AND FUNDAMENTAL LASER-TISSUE COUPLING

By

Leia Megan Shanyfelt

August 2008

Chair: David Hahn
Major: Mechanical Engineering

Several topics in excimer laser corneal ablation remain unresolved, ranging from fundamental to practical. The roles that photothermal and photochemical processes play in the mechanism of corneal ablation remain a topic of research, including laser-tissue coupling below the ablation threshold. Goals of the present work are to investigate the mechanism of photoablation and to assess whether bovine corneal ablations generated at laser repetition rates up to 400 Hz are comparable to ablations performed at current clinical rates (60–100 Hz).

A combination of experiments was implemented, including ablation plume dynamics, corneal ablation profiles and high-resolution microscopy. Using white-light interferometry analysis, no statistical difference was found between corneal ablation profiles created at 60 Hz and 400 Hz. Using plume imaging and transmission studies, the bulk ablation plume was found to dissipate on a time-scale less than the pulse-to-pulse separation for repetition rates up to about 400 Hz. A persistent, diffuse component of the ablation products was observed to be comparable at both rates. Microscopy did not reveal signs of thermal tissue damage for repetition rates up to 400 Hz. Ablations performed on PMMA did not reveal repetition rate effects. Ablation pattern algorithm reversal and plume extractor addition were analyzed for potential effects on the clinical outcome. Increasing laser repetition rates for clinical applications appear feasible.

Sub-ablative fluences utilizing 193-nm and 355-nm perturbations yielded insight into photochemistry of collagen and amino acids. Amino acid solutions were not permanently altered by either wavelength. For collagen solutions, an average of 28 photons at 193 nm was required to break a peptide bond. 355-nm perturbations resulted in an average of 508 photons required to break a peptide bond. A dynamic photobleaching occurs in both amino acid and collagen solutions at both wavelengths and is greater at 193 nm than at 355 nm, resolving by more than tens of nanoseconds but less than tens of seconds. Permanent changes induced in the collagen samples are due to scission of peptide bond. Mass spectrometry experiments analyzed the ablation products in the ablation plume. The experiments indicate a primarily photochemical ablation mechanism with peptide bonds being the primary chromophore.

CHAPTER 1
BACKGROUND

Excimer Laser Refractive Surgery

Excimer laser refractive surgery is a technique that is used with a goal of permanently correcting an individual's vision by reshaping the eye's cornea, thus reducing or eliminating dependence on corrective lenses. Over the past two decades, this type of surgery has grown immensely in popularity. To date, more than 8 million procedures have been performed nationally and more than 17 million have been performed globally. Currently excimer laser refractive surgery is the most popular option for surgically correcting poor visual refraction [1].

Human Cornea

The cornea is the curved structure overlaying the pupil and iris of the eye. The cornea (1/6 of the outer tunic), together with the sclera (5/6 of the outer tunic), forms the outer fibrous tunic (covering) of the eye, which provides support and protection for the eye. The iris is the part of the eye that gives it its color. The iris can tense or relax to vary the amount of light that is allowed through the pupil, which is the dark central region of the eye. When the iris relaxes, the pupil dilates, and more light is allowed into the eye. When the iris tenses, less light is allowed into the eye. Behind the iris and pupil is the lens. The cornea focuses light through the pupil and onto the lens of the eye, which in turn focuses light onto the retina. Together, the cornea and the lens provide the refractive properties of the eye, with the majority of the refraction being performed by the cornea. The optic nerve transmits the visual information to the brain. The cavity of the eye behind the lens is filled with vitreous humor which retains ocular pressure [2, 3]. Figure 1-1 is a schematic of the general placement of the cornea, pupil, iris, lens, sclera, vitreous humor and optic nerve of the human eye [4].

The cornea is a sensitive, transparent (from 400 nm to 1200 nm wavelengths), avascular structure whose anterior (front) surface remains smooth and clean via the lacrimal (tear) glands and blinking action. The corneal geometry is asymmetric; the average horizontal diameter is 12.6 mm, while the average vertical diameter is 11.7 mm. Additionally, the posterior surface is less spherical than the anterior surface, thus the cornea ranges in thickness from approximately 500 microns at the center of the cornea to approximately 700 microns at the edge of the cornea. The approximate radius of curvature is 8 mm [2, 3].

The cornea itself is made up of five distinct layers. From anterior (front) to posterior (back) they are the epithelium, Bowman's layer, stroma, Descemet's Membrane, and endothelium. These layers are shown in Figure 1-2 [4]. The epithelium and the endothelium are the anterior and posterior membranes, respectively. The epithelium is a protective cellular layer that is a barrier between the cornea and the external environment. Bowman's layer consists of densely packed collagen fibers arranged parallel to the corneal surface. This layer is thought to provide additional structural integrity to the cornea. The stroma, which makes up 90% of the corneal thickness, also consists of collagen fibers, though less densely packed than in Bowman's layer. Descemet's membrane and the endothelium provide posterior protection for the eye. The endothelium prevents fluid from within the eye from entering the cornea [2, 3].

As explained above, the main target for corneal tissue removal in photorefractive surgery is the stromal layer. The corneal stroma is made up of approximately 80% of water and about 20% collagen. The collagen and water make up a complex composite material, the extracellular matrix (ECM), which gives the cornea its structural integrity [5]. The collagen matrix structure consists of regularly-spaced collagen fibrils which are of approximately equal diameter, arranged in layers of parallel lamellae. The stroma is made up of about 300–500 lamellae (bundles) of

parallel fibrils, with each bundle of fibrils arranged parallel to the adjacent bundle [2, 3, 6]. The reported values of the diameter of the fibrils ranges considerably, namely from 20 to 34 nm. The center-to-center spacing of the fibrils is 64–67 nm [5].

In the central region of the cornea, the diameter is considered independent of corneal hydration [2, 3, 6, 7]. The characteristic thicknesses of the lamellae are approximately 1–2 μm [5].

The detailed composition and morphology of the corneal tissue dictate the optical properties of the tissue, which in turn establish the internal volumetric distribution of energy of incident laser pulses. Collagen is a right-handed triple helix structure, as shown in Figure 1-3, obtained from [5]. Each strand of the helix is made up of amino acids bonded in series by peptide (C–N) bonds into a left-handed helix. The three strands are bonded together by covalent cross-links into the tropocollagen (TC) molecule. The TC molecules are 1.51 nm in diameter and 290 nm long. The TC molecules organize to form the microfibril, which is approximately 3.5 nm in diameter and made up of 6 TC molecules bound by covalent cross-links. The microfibrils then organize to form the collagen fibrils of the ECM [5, 8].

For corneal collagen, each strand of the helix is made up of an amino acid chain which generally repeats itself. The amino acid glycine ($C_2H_5NO_2$) appears about every third amino acid, as shown in Figure 1-3. Generally, the amino acids proline ($C_5H_9NO_2$) and hydroxyproline ($C_5H_9NO_3$) occur every third amino acid as well; however, trace acids may appear in their stead. Generally, corneal collagen ($C_{12}H_{17}N_3O_4$) can be considered to be a repeating structure of glycine-proline-hydroxyproline. A single repeating unit is modeled in Figure 1-4 [5, 8].

When ablated, the immediate underlying stroma becomes disrupted and may become thermally damaged. Notably, at temperatures above approximately 60^{o}C, coagulation and

denaturing of collagen can occur. Denaturing of collagen occurs when the temperature rise increases the kinetic energy of the collagen molecules such that weak hydrogen bonds and Vander Waals interactions are overcome. This results in destabilization of the right-handed helix of the TC molecule. These effects can be observed using TEM microscopy. The denatured collagen fibril is longitudinally shorter and has thicker cross-sections. Disruptions in the collagen structure occur, and a "pulling together" of fibrils can be seen. This causes the inter-fibriller distance at the ablation surface to become shorter, and thus the density of collagen fibrils would be expected to increase [3, 5, 9]. The level of disorganization and fiber densification observed with high-resolution microscopy may therefore be considered a measure of thermal damage to the underlying tissue [9].

Thermal denaturation of collagen depends on both the tissue temperature and time of exposure. For short thermal exposure times (ns–ms range), it has been found that the temperature to denature collagen is in excess of 100^{o}C [5]. Venugopalan and co-workers attempted to model the effect of various laser parameters, including pulse duration and laser irradiance, to determine the zone of thermal energy as a function of the Péclet number [10]. Unfortunately, a lack of knowledge of the ablation mechanism limited the model, as acknowledged by the authors. A model of thermal damage induced by 193-nm irradiation that takes into account current understandings, including dynamic optical properties and Beer-Lambert law deviation, still remains unavailable. Thermal damage should be considered in the context of higher laser repetition rates, as less time is available between laser shots for energy to dissipate via conduction within the corneal stroma. Thus energy may accumulate for each laser pulse, and result in higher nearby tissue temperatures, which may result in greater underlying tissue damage.

Clinical Implementation

Since the first procedure in 1988, refractive vision surgery using laser ablation (removal) of tissue has become very popular [11]. Approximately 45% of Americans have poor refraction, with 25% of those being myopic (nearsighted), 20% being hyperopic (farsighted) and 35% being astigmatic [12]. Photorefractive keratectomy (PRK) and laser *in situ* keratomileusis (LASIK) are methods of visual correction known as refractive surgery. Both PRK and LASIK are forms of keratomileusis, a technique that uses a laser to reshape the cornea about the optical axis to obtain the correct corneal geometry, thereby changing the corneal refractive properties to achieve optimal vision for the patient [3]. Myopic individuals have corneas that are too steep, resulting in a visual focal point in front of the retina. In order to correct for this, the laser is used to flatten the corneal surface. Conversely, Hyperopic individuals have corneas that are too flat, resulting in a visual focal point behind the retina. Hyperopia is corrected by using the laser to steepen the cornea [4].

Though the principles of PRK and LASIK surgeries are generally the same, the two differ in their application. In PRK application, the epithelium over the ablation area is removed chemically, mechanically (scraped or brushed away) or by the laser itself, and the exposed corneal tissue is ablated. Both Bowman's layer and the stroma are ablated in this operation. In LASIK, suction is applied to the anterior surface of the cornea, and a microkeratome is used to cut an anterior corneal "flap" that includes both the epithelium and Bowman's layer. The flap is moved aside, and the underlying stromal tissue is ablated, and the corneal flap is then replaced [12]. It is noted that while the epithelium regenerates quickly, Bowman's layer does not regenerate at all following PRK surgery. This difference results in an advantage of LASIK over PRK, since there is less scarring and regression when Bowman's layer is preserved [11]. One study of six myopic patients determined that the absence of Bowman's layer after PRK does not

hinder re-epithilialization, which is typically completed during the first post-operative week [13]. Some advantages of LASIK compared to PRK include less scarring, quicker results, less pain, and less post-operative medication [4].

A wide range of reported experimental ablation rate data has been summarized and plotted (Figure 1-5) by Fisher *et al.*, and indicates laser fluences ranging from about 25 to 700 mJ/cm^2 with corresponding ablation rates from threshold to about 1.4 μm/pulse [14–23]. A review of current FDA-approved LASIK systems reveals a wide variety of average laser fluences on the current market, ranging from about 100 to 250 mJ/cm^2, although the peak fluence with Gaussian beams may be in excess of 500 mJ/cm^2 [24].

As demand for the procedure has increased, the surgical procedures and devices have evolved, and laser photorefractive surgery continues to be studied for ways to improve clinical outcome and convenience. Accordingly, accuracy and precision, as well as patient comfort, must be considered in these endeavors.

Clinical Issues

While much work has been done to improve excimer refractive surgery over the last two decades, many issues are as yet unresolved:

- The surgical process is a closed-loop system. The number of shots to achieve a specified correction is programmed into the computer prior to surgery, and no feedback loop exists to correct for actual conditions. The number of shots delivered by the excimer laser is based on an average amount of tissue removed for all people, including all races, both sexes and all ages. Of course, everyone's physiology is unique, so using such a general parameter is not ideal. Introduction of system that uses actual conditions, particularly corneal hydration, to adjust the prescribed number of shots would be useful. Hydration is known to affect the etch depth per incident laser pulse. Specifically, cornea dehydration leads to an increase in laser ablation rate [25–27]. Fisher and co-workers used a confocal Raman spectroscopy apparatus to assess corneal hydration in bovine eyes, noting significant changes in clinically-relevant time scales of minutes [28].

- The mechanism of corneal tissue removal is not fully understood. A detailed knowledge of the photoablation of corneal material could lead to improvements in surgical lasers, algorithms and post-operative care. This topic is discussed in detail in a later section.

- Using faster laser repetition rates to reduce overall procedure time is an obvious advantage from a patient perspective. Much of the present research is devoted to this topic, as one cannot simply increase the laser repetition rate without investigating the prospective consequences. These include potential changes in the ablation rate and increases in the damage to underlying and surrounding tissue due to a possible increase in underlying tissue temperature.

- The algorithms used to generate the laser patterns used to remove corneal tissue are not yet perfected. The basic model used to develop ablation algorithms was the blow-off model, which is based on the Beer-Lambert law. Inherent in the blow-off model are the assumptions that Beer-Lambert applies, that there is a finite threshold fluence, and that material removal begins after the laser pulse is concluded. The second two assumptions are known to be valid for the case of corneal ablation by an ArF laser. The blow-off model predicts the following etch depth:

$$\delta = \frac{1}{\mu_a} \ln\left(\frac{\Phi_o}{\Phi_{th}}\right) \tag{1-1}$$

  In the above equation, δ is the etch depth, μ_a is the absorption coefficient, Φ_O is the incident fluence, and Φ_{th} is the threshold fluence [5]. A group in Spain has devoted much effort to identifying and resolving potential influences on the guiding algorithms, including Beer-Lambert law applicability, beam profile considerations, non-normal beam incidence, reflection losses and laser polarization. It was discovered that ablation does not follow Beer-Lambert's law, which is fundamental in the blow-off model, and that corrections should be implemented in surgical algorithms to correct for this deviation. Additionally, loses in energy due to reflection and non-normal incidence were found to reduce the predicted ablation depth [29–33]. Recently, Fisher & Hahn developed a more current model that takes into account a dynamic tissue absorption coefficient and predicts the variation in etch depth with corneal hydration [14]. Improving algorithms may result in better outcomes than the current national norm of approximately 90% of patients achieving 20/40 vision or better and approximately 65% achieving 20/20 vision or better [34].

- The healing process after the surgery could also be improved. Eiferman and co-workers noted in an early study that there are no adverse effects on the eye caused by the laser itself. It is noted that the high absorption coefficient of the cornea for 193-nm radiation limits the penetration of the incident pulse to within a cellular layer of the ablated tissue. They also determined that endothelial cell counts an intraocular pressure remained unchanged from pre-surgery conditions and important observation because endothelial cells do not regenerate like their

epithelial counterparts. Also, contrast sensitivity and brightness acuity were not degraded at 3- and 6- months post-operative [13]. Corneal haze, one of the more common side effects of laser ablation, may appear after PRK or LASIK, and usually dissipates during the first 12 months post-operative. Other complications include glare, halo and decreased contrast. Healing is generally faster after LASIK than PRK, and development of corneal haze is less common [12]. Much research has been devoted to the topic of corneal haze, which occurs when keratocytes in the cornea become fibroblastic and lose their transparency and act as light scattering centers within the cornea. Haze is a common post-operative occurance in the first four months following surgery, and typically diminishes over time [11, 35–37].

- In many cases the first refractive surgery results in under-correction, and a second surgery is needed to complete the refraction [12]. The larger the refractive change required, the greater the chance that a secondary surgery will be required. This fact couples into the closed-loop system discussion above. Any errors in the algorithm and number of shots prescribed will grow with the length of the surgery. Also, hyperopic individuals are more likely to require enhancement than myopic individuals. As it can take several months for one's vision to settle into an outcome; hence, enhancement surgeries are typically not performed for 3–6 months. Ideally, secondary surgeries to refine the results would be unnecessary in all cases [34, 38].

Polymer Ablation

It is also useful to study the larger body of polymer ablation to gain additional insight into tissue ablation. In 1983, Srinivasan at the IBM Research Center pioneered the technique he coined "ablative photodecomposition", or APD, which eventually led to photorefractive surgery as we know it. This new etching technology, which was made possible by the advent of the UV excimer laser in the late 1970's, uses ultraviolet (UV) radiation to sculpt the targeted material with great precision. Excimer lasers have diatomic species – Ar_2^*, Kr_2^*, Xe_2^*, ArF, ArO, KrF, KrCl, XeCl and XeF, for example – as the active medium inside the laser cavity. The term excimer laser comes from "excited dimer". Technically, excited dimers are homonuclear, such as Ar_2^*. Many excimer lasers are actually "excited exciplex" lasers which are heteronuclear, such as ArF; however, the term excimer is used for both dimer and exciplex varieties. These gas lasers are ultraviolet pulsed lasers with pulses on the order of nanoseconds with powers ranging from 1 to 100 W [39, 40].

APD was and is still attractive due to its high spatial resolution and lack of thermal damage to surrounding material. The early work on the topic was performed on organic polymers, particularly poly(ethylene terephthalate), or PET; polyimide, trademark name Kapton; and poly(methyl methacrylate), or PMMA. It was first noted how cleanly far-UV laser light etched the surfaces of these organic polymers, and early investigations focused on determining the etch rate (material depth removed per shot) of these materials. From these beginning experiments, interest in the topic boomed and deepened, with identified potential applications in microfabrication, microsurgery and art restoration.

The question of exactly how the photodecomposition occurs has since been debated. Experimentalists have examined the effects of UV ablation with a wide variety of parameters such as environment, laser wavelength, laser pulse width and laser pulse energy on the specific ablation mechanisms of PET, Kapton, PMMA and others. Additionally, many different types of excimer lasers have been used in these studies, including KrF (248 nm), KrCl (222 nm), ArF (193 nm) and XeCl (308 nm). With the variety in UV radiation source comes a spread of laser fluence, excitation wavelength and pulse duration. This is an extremely large array of experimental conditions.

The first proposed mechanism for APD with 193-nm light on PMMA was a photochemical one which predicted that after reaching a threshold energy (fluence) required for smooth etching, the laser pulse energy causes bonds to break within the polymer strands, thus increasing the specific volume of the material. The excess energy remaining from the photon after the bonds are broken vibrationally, rotationally and translationally excites the polymer fragments, which are ejected from the polymer surface [39]. Additional investigators contended that the mechanism is entirely thermal, and not photochemical at all [41]. Still more presented mechanisms are reported

to involve both thermal and photochemical interactions [42–44]. These disagreements among early authors were indicative of a prolonged difficulty in specifying the exact mechanism of APD.

Over the next two decades the argument has continued with no resolution. The mechanism of ablation of polymers by UV radiation is still unknown. Many groups, including chemists and physicists, across the globe have studied the topic using a vast array of techniques including laser-induced fluorescence, mass spectrometry, emission spectra and Raman spectroscopy. Still no agreement on the mechanism of ablation has been reached [45, 46].

Current theories include photochemical and photothermal mechanisms. In the case of photochemical theories, photon excitation directly results in bond breaking. Both single and multi-photon absorption models have been proposed. In the case of photothermal theories, photon excitations lead directly to thermal breakdown of the polymer bonds. Many other theories incorporate combinations of these two [45, 46]. Part of the difficulty is the vast array of parameters that alter the experiments. It is generally agreed that changes in excitation wavelength, pulse duration, laser fluence, and the properties of the specific polymer studied, including refractive index and molecular weight all influence the precise mechanism of ablation.

In the experiments presented in the current study, a 193-nm ArF laser was used to etch PMMA. PMMA is a polymer created of monomer units of MMA. The arrangement of a PMMA molecule is depicted with two of the repeating monomers in Figure 1-6 below [47].

PMMA has successfully been used in the past as a surrogate model for laser refractive surgery. Past studies have employed the polymer to predict the impact of surgery on corneal shape and to estimate post-operative corneal surface roughness. Consider the algorithm limitations outlined by Jimenez and co-workers as described above. Variations based on things

such as reflection loss and non-normal incidence are expected to have the similar impact on PMMA as on a human cornea [26, 48].

It is important to note the differences between the ablation characteristics of the two materials, namely polymers and corneal tissue. First is the ablation threshold. Ablation in the human cornea begins between 40 and 60 mJ/cm^2, while ablation in PMMA begins around between 35 and 80 mJ/cm^2 for ns-pulsed ArF excimer lasers. Additionally, the ablation rates (amount of material removed per laser pulse) are unequal. One study found the ratio to be 1.8 microns of corneal material removed per 1.0 micron of PMMA removed by comparing overall ablation depths generated on PMMA by a flying spot laser system with the published corneal overall ablation depths provided by the vendor. It is important to keep these factors in mind when comparing ablation patterns created on the different materials; accordingly, one would expect a corneal ablation profile to be slightly wider and much deeper than a profile created on PMMA using the same algorithm [48, 49]. For a comparable laser system as that used in the current experiments, the ablation rate of PMMA was measured to be 0.47 μm/pulse [50].

The ablation of PMMA is non-linear as a function of fluence. The semi-log plot of depth verses fluence has a “lazy S” shape with three distinct zones. In the first zone at lower fluences, the etch rate increases slowly with fluence, as the threshold value for ablation is reached. The second zone is a linear region where etch rate increases consistently with increased fluence. At high fluence, this linear regime ceases, and the etch rate begins to level off, or even decrease. An example plot of this behavior obtained from Srinivasan and Braren is presented in Figure 1-7 [49].

Corneal Ablation

Very soon after APD was described for polymers, ablation of tissue by UV lasers began to be investigated for possible applications, including corneal refraction correction. A thorough understanding of the physics and mechanisms of corneal ablation and the potential role of laser repetition rate remains a topic of research [5, 28, 31, 51–54]. As the exact mechanisms of photoablation remain unidentified, it is critical to verify that increasing the laser repetition rate does not reveal any differences in surgical outcome or underlying corneal pathology. The laser-tissue interaction may be generalized as a dynamic process during which the corneal optical properties are perturbed by the laser beam during the time-course of the ablating laser pulse. In the context of a photochemical ablation process, photocleavage of collagen bonds leads to subsurface expansion of the corneal tissue matrix and subsequent stress that drives the ablated tissue from the surface in the form of the well-known ablation plume [14, 55–59].

As previously described, the human cornea is comprised of mainly collagen and water. For corneal ablation, a main parameter is the tissue absorption coefficient. The tissue absorption coefficient dictates how strongly the incident laser energy is absorbed into the tissue and how deeply the energy will penetrate. In corneal ablation, where light scattering by the transparent tissue is negligible, the optical penetration depth of the incident radiation is defined as the reciprocal of the absorption coefficient. The optical penetration depth is the depth to which the laser energy will travel, and which the tissue is affected. In order to understand ablation of corneal tissue, the absorption coefficient for both collagen and water must be understood. At room temperatures, absorption by water of 193 nm is negligible as compared to that of collagen. The absorption of collagen at 193 nm is significant, with an absorption coefficient of approximately 2–4 x 10^4 cm^{-1}. The most important chromophore at 193 nm is the peptide bond which separates the constituent amino acids. The peptide bond absorption peaks roughly at 190

nm. The absorption of laser light by collagen is highly sensitive to wavelength, as the absorption of collagen-based tissues drops at least 100 times when wavelengths of 240–290 nm are used as compared to 193 nm [5, 51].

The energy supplied by the ablation laser causes thermal and mechanical changes in the corneal tissue, which result in significant changes to the tissue optical properties. In fact, the absorption coefficients of both water and collagen are enhanced by addition of the laser energy to the tissue. The absorption coefficient of water is enhanced as the absorption band (peak) normally located at 160 nm shifts to longer wavelengths, resulting in a non-negligible absorption coefficient of water during the ablation process. For a volumetric energy density of 2 kJ/cm^3, the absorption coefficient may reach 10^4 cm^{-1} [60]. The absorption of collagen was found to be increased by exposure to laser energy at 193 nm for times up to 10^{-4} seconds after the laser pulse [61, 62]. Pettit and Ediger found that the absorption coefficient at 193 nm of stromal tissue to be 40,000 +/- 10,000 cm^{-1}, a value 10 times higher than previously reported values [63]. Fisher and Hahn found the value to be 16,000 cm^{-1}, Yablon *et al*. found the value to be 19,000 cm^{-1} and Munnerlyn *et al*. found the value to be 37,800 cm^{-1}, all confirming the work of Pettit and Ediger, namely that the absorption coefficient is significant and maby be enhanced during the ablation process [8, 64, 65].

The ArF excimer laser ablation of corneal tissue is considered to entail considerable bond breaking and the ejection of molecular fragments. The dissociation energies (eV) of selected molecular bonds in tissue are identified in Table 1-1. These energies may be compared to the 6.4 eV photon energy (E = hν) of the 193-nm ArF excimer laser used in photorefractive surgery. The energy of a single photon of ArF irradiation is sufficient to break all of the molecular bonds of Table 1-1, with the exception of C=O, as adapted from Vogel & Venugopalan, 2003. The

photon energy of the ArF excimer laser is also larger than that of other UV lasers, such as the KrF excimer (5.0 eV) and the XeCl excimer (4.0 eV). In order for bond breakage by the excimer laser to be the primary means of photodecomposition, the rate of bond breakage by the UV laser must exceed the rate of recombination by the broken bonds in the decomposed species [5].

The decomposition of collagen into fragments results in a larger volume of material, which in turn generates a local stress within the cornea. This internal stress then results in the ejection of the fragmented corneal material. As previously indicated, the peptide bonds that link the constituent amino acids of the collagen are the primary chromophores, and is thus the primary candidate for the specific corneal bonds that are broken due to exposure to the excimer laser energy. It is thought that this is an important piece of the mechanism of tissue removal in corneal photorefractive surgery; however, this does not form the complete picture. It is also generally thought that photothermal (or thermal) effects play a role in the ablation mechanism. Energy exceeding the bond energies increases the kinetic energy of the tissue, resulting in temperature increases of the dissociated products. A portion of this energy may also transfer to the water in the cornea, increasing its temperature and thus allowing it to become a greater chromophore as its absorption coefficient rises. Vaporization of water may then occur [5]. Others found that the corneal surface temperature exceeded 100^{o}C when ablated with an ArF with a fluence of 80 mJ/cm^2, further indication of significant thermal contributions [66]. However, due to the brief nature of the laser pulse (tens of nanoseconds), thermal diffusion to surrounding tissues is minimized. This coupled with the short penetration depth lead to minimal thermal damage of the underlying stroma [5].

Another important feature of corneal ablation is the ablation threshold. At low energies, by definition the laser exposure does not ablate the cornea. At a specific radiant exposure

(approximately 30–60 mJ/cm^2), known as the ablation threshold, tissue removal begins. At higher energies, the etch depth of the ablation increases with radiant exposure [5, 17, 48]. For a comparable laser system as that used in this experiment, the ablation rate of bovine corneas was measured to be 0.90 μm/pulse [50].

Additionally, Fisher and Hahn reported values of the absorption cross section of peptide bonds and amino acids in collagen solutions. The overall absorption coefficient for collagen was found to be 1.19E-17 cm^2, while the contribution by peptide bonds was calculated as 1.14E-17 cm^2 and that by amino acids was calculated to be 4.74E-19 cm^2 [8]. Another parameter of interest is the quantum yield. The quantum yields and relative concentrations of collagen components can be used to determine a probability of photochemical damage. This probability has been reported as 300–500 cm^{-1}M^{-1} for peptide bonds, 4.7 cm^{-1}M^{-1} for glycine and 2.5 cm^{-1}M^{-1} for proline. These numbers were generated on the assumption that glycine made up 33% of the collagen and proline made up 13% of the collagen. The probability for photochemical damage is much greater for peptide bonds than for amino acids. The same study also determined that 60% of peptide bonds within corneal collagen may be destroyed with each incident laser pulse. This, along with the probabilities, supports the supposition of a photochemical mechanism [51].

Experimental Methods and Studies

Plume Dynamics

With each incident excimer laser pulse, the ablated corneal material is ejected from the eye surface to form the ablation plume. It is essential to examine the dynamics of this plume to determine if the physical removal of tissue during ablation is altered as the laser pulse rate is increased to values higher than current clinical rates. Excess material lingering over the surgical plane may alter the ablation process, notably by attenuating (shielding) the laser pulse energy and thus decreasing the amount of corneal tissue removed. Also, the excess material could settle

back down onto the corneal surface, also resulting in under-ablation of the cornea. This phenomena is generally associated with wide beams [5, 65, 67]. Accordingly, it is desirable that the ablation rate provide adequate time for the ablation plume from one shot to sufficiently dissipate before the next laser shot occurs.

The ablation plume is made up of the material ejected from the ablation site, and may include water vapor, water droplets, gaseous organic products and particulate tissue fragments. Hahn and co-workers found water droplets to be the dominant constituent present in corneal ablation plumes [68]. There is a delay between the incident laser pulse and the beginning of the ejection of the plume, which has been measured as 70 ns for ArF ablation of corneal tissue. The velocity at which the plume ejects is over 600 m/s for fluences in the range of 300 mJ/cm^2 to 1 J/cm^2, and exerts a recoil stress upon the cornea. After 500 ns, the plume slows to approximately 350 m/s [5].

The ejected material rises from the entire ablated surface area and immediately "necks" into a typical mushroom cloud. This effect is due to Bernoulli's law that requires that the sum of the static pressure and the dynamic pressure (the product of one-half the density) and the square of the flow velocity be constant. As the velocity of the flow is quite large, the pressure in the flow relative to the surroundings becomes small; thusly, the flow from the corneal surface immediately condenses to a tighter diameter. The mushrooming at the top then occurs due to turbulent eddy formation [5].

One way to analyze plume dynamics is by imaging the plume as it is ejected from the corneal surface using a camera [67, 69]. The resulting pictures allow the plume to be visually analyzed, including time-evolution of the plume. A second way to analyze the plume is with

transmission studies [70]. Figure 1-8 shows a typical transmission experiment setup. In general terms, the transmission is defined as

$$\tau = \frac{I(\ell)}{I_0}, \tag{1-2}$$

where I(ℓ) is the intensity of the laser light after passing through the plume path length, ℓ , and I_0 is the incident laser intensity. A 100% transmission measurement corresponds to an optically transparent sample. Therefore, when no material in the sample is present, the transmission would be equal to unity. As more material is added inside the pathlength, the transmission measurement will decrease. In the case of plume dynamics, the plume itself is the "probed sample".

White-Light Interferometry

An important tool for analysis of ablation craters is the white-light interferometer. There are two main types of interferometers: Fabry-Perot and Michelson. Only a Michelson interferometer was used for the present study. The Michelson interferometer, invented by Albert Abraham Michelson, is a "division of amplitude" interferometer, meaning that the incident white light beam is split into two separate beams that interfere with each other [71, 72]. A basic Michelson interferometer is diagramed below in Figure 1-9.

The incident beam (source) is split using a partially-reflective plate (beam splitter), such that part of the incident beam passes straight through the plate toward the fixed mirror, and part of the incident beam is reflected at 90^o toward the movable mirror. The compensator is an optical piece of the same material and thickness of the plate, and is used to ensure that both beams pass through the same material thickness. Without this piece, one beam would pass through the plate material once, while the other would pass through it three times. Both portions of the beam recombine at the plate and reflect onto the detector. The recombined light has a pattern of interference fringes, because the two beams of light have traveled different distances [71, 72].

The interference is a function of the phase difference of the two beams. In the case of a monochromatic light source, the out-of-phase difference distance t can be related to the pathlength difference x. The distance t is the physical difference between the image plane from the stationary mirror image and the image plane of the movable mirror image. The distance x can be varied by moving the movable mirror parallel to itself. Moving this mirror changes the pathlength difference of the two beams by twice the distance that the mirror is moved. The relation between t and x is therefore given by the following equation:

$$x = 2t = m\frac{\lambda}{2} \tag{1-3}$$

When the value of m is an even number, the images interfere constructively. Likewise, when m is an odd number, the images interfere destructively. This makes intuitive sense if one think about the wave behavior of light. If the two image waves come in together in-phase, the amplitude of the wave will be doubled (constructive interference). If the images come in together exactly out-of-phase ($\lambda/2$ phase difference), the amplitude of the waves will cancel each other out (destructive interference) [71, 72].

White-light interferometry is more complex; however, the general concepts are the same as that with a monochromatic source. In the experiments performed in this study, a Zygo NewView scanning white-light interferometer was used to determine detailed surface geometry of various samples. This specific interferometer scans vertically by using a piezoelectric transducer to move the microscope objective, rather than using the "movable mirror" discussed in the basic interferometer setup. The traditional "movable mirror" is stationary in this device. Realize that this type of movement can be related to moving the "movable mirror", as the pathlength increase of the side beam will be double that of the increase of the main beam. The NewView reflects light off of the sample to be measured and off of a high quality reference surface. Both of these

reflections are recombined onto a solid-state camera. The NewView System itself converts the white-light interference fringes into useful distance variations and creates a three-dimensional profile of the measured sample [73]. White-light interferometry has been successfully used to study ablation crates created by a photorefractive surgery laser system [50].

Mass Spectrocsopy

Mass spectrometry has been used to identify ablation plume products. Two studies have analyzed the products from ablated human corneas. Unfortunately, these studies are dated. The technology has progressed in the last decade, as has the understanding of the ablation process [74, 75].

Kermani and co-workers examined the ablation plume from ablating human corneas with an ArF (193 nm) excimer laser and a KrF (248 nm) excimer laser at fluences from 5–80 mJ/cm^2 at 1–2 Hz. The intent of their study was to use mass spectrometry analysis of the ablation plume to glean information about the difference in corneal ablation performed at different wavelengths and different energies. There are two distinct limitiations in their experiment. First, they had available old laser technology that resulted in poor-quality beams with uneven energy distribution. Second, the mass-spectrometry apparatus involved pulling a vacuum on the eye prior to and during ablation. The authors noted that the vacuum (10^{-7} Torr) dehydrated the eye prior to ablation, as during the evacuation process, the mass spectrometer registered water in the system. This causes two distinct problems. It is now well-known that corneal ablation is affected by corneal hydration, affecting the ablation rate of tissue. It is has also been discovered that water droplets and vapor are constituents of the ablation plume. Therefore, by dehydrating the tissue prior to ablation, the ablation is altered and the mass spectrometric analysis is incomplete. With today's knowledge and technology, these limitations can be overcome [25–28, 68, 75].

Kahle and co-workers examined the ablation plume from ablating human corneas with an ArF (193 nm) excimer laser and a Er:YAG (2.94 μm) solid-state laser at a fluences of 180 mJ/cm^2 and 2.7 J/cm^2. The ArF excimer laser had a beam width of 3.5 mm and a repetition rate of 10 Hz. The second experiment was subject to the same limitations as that of Kermani, *et al*. An air pump was used to pull the samples through to the mass spectrometer through a moisture absorber. It is unclear from the description of the experiment if the eye was dehydrated due to the pull of the pump. However, the same argument related above regarding dehydrated plume samples is applicable [74].

Kermani and co-workers found low-amu (less than 20 amu) components in the ablation products, including H_2, C, CH, CH_2, CH_3 and NH_2 and higher-amu components including COH, CH_2NH_2, CH_2OH. In contrast, Kahle and co-workers found $C_{10}H_{23}ON$, $C_{11}H_{24}$, $C_{12}H_{26}$, $C_{14}H_{30}$, $C_{14}H_{24}O_3$, $C_{20}H_{38}$, $C_{20}H_{14}O_3$ and $C_{21}H_{24}$ in the ablation products. The results of the two studies are not in agreement [74, 75].

As with other ablation experiments, plume analysis via mass spectrometry has been performed on polymers. Some examples are provided here. Grivas and co-workers used time-of-flight mass spectrometry to study the dynamics of polyarylsulfone films, which are used in microelectronics. Tsunekawa and co-workers used mass spectrometry to study laser ablation of PMMA and PS at 308 nm to study the mechanism of polymer ablation. Hansen used time-of-flight mass spectrometry to study the ablation products of several polymers, including PMMA. Thus, the use of mass spectrometry as a tool for ablation plume analysis has been proven [76–78].

Objectives of the Present Work

There are several topics in the field of excimer laser corneal ablation that remain unresolved. These topics range from the fundamental to the practical. The specific mechanism of corneal ablation is not fully understood to date. For example, the roles that photothermal and photochemical processes play remain a topic of research, including the laser-tissue coupling at and below the ablation threshold fluence. A goal of the present work is to investigate the mechanism of photoablation. Another goal of the present work is to assess whether bovine corneal ablations generated at laser repetition rates of up to 400 Hz are comparable to ablations performed at rates consistent with current clinical laser systems (60 to 100 Hz). Increases in laser repetition rate will reduce surgical procedure time and are therefore beneficial. Specific research tasks in this proposal are as follows:

- Plume Dynamics
- Ablation Profiles
- Histology
- Sub-Ablative Study
- Mass Spectrometry of Ablation Plume

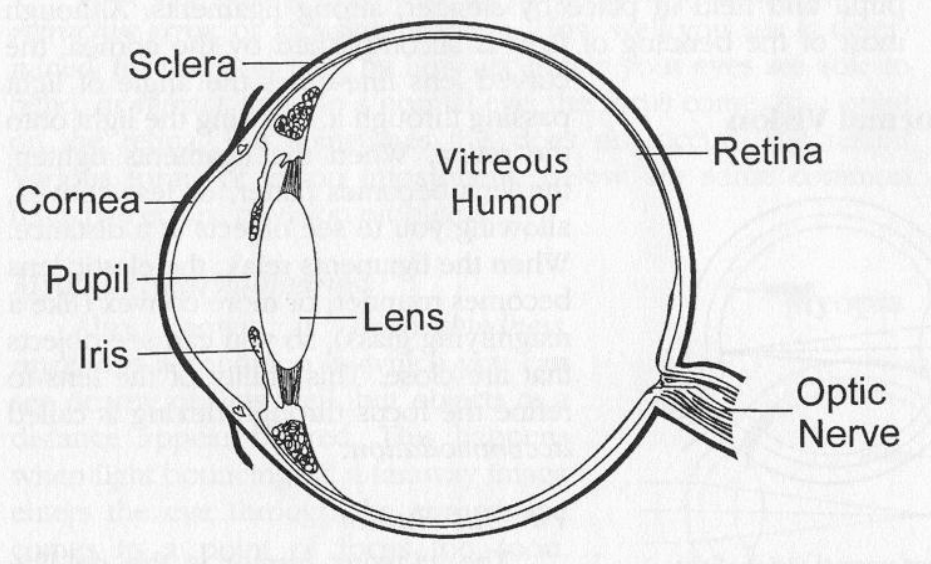

Figure 1-1. Schematic of the human eye, taken from reference 4

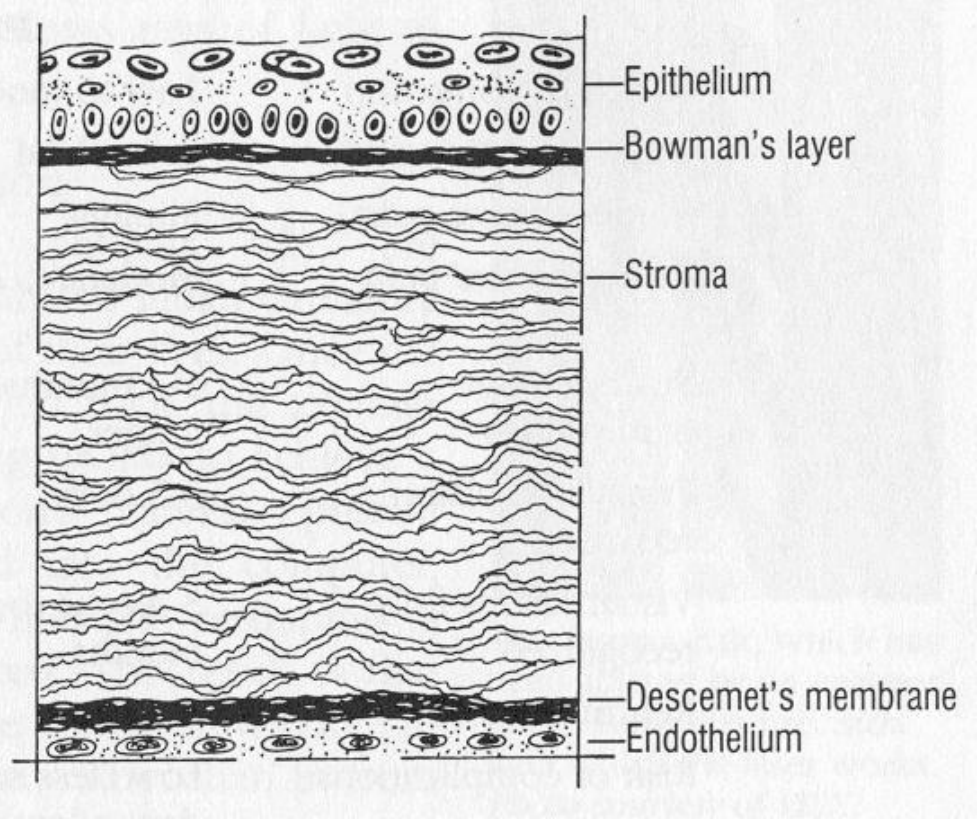

Figure 1-2. The five layers of the human cornea, taken from reference 4

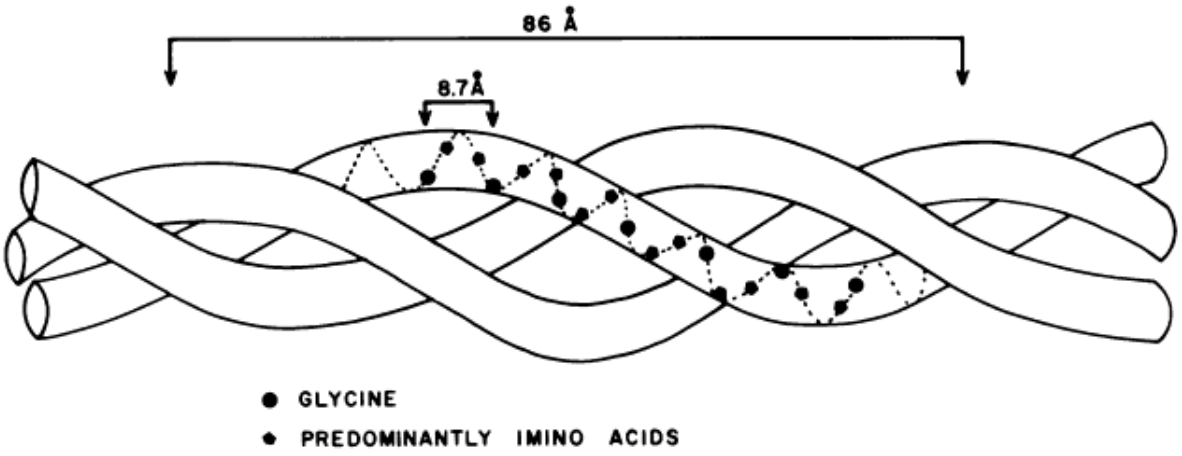

Figure 1-3. Schematic of the triple-helix structure of collagen, taken from reference 5

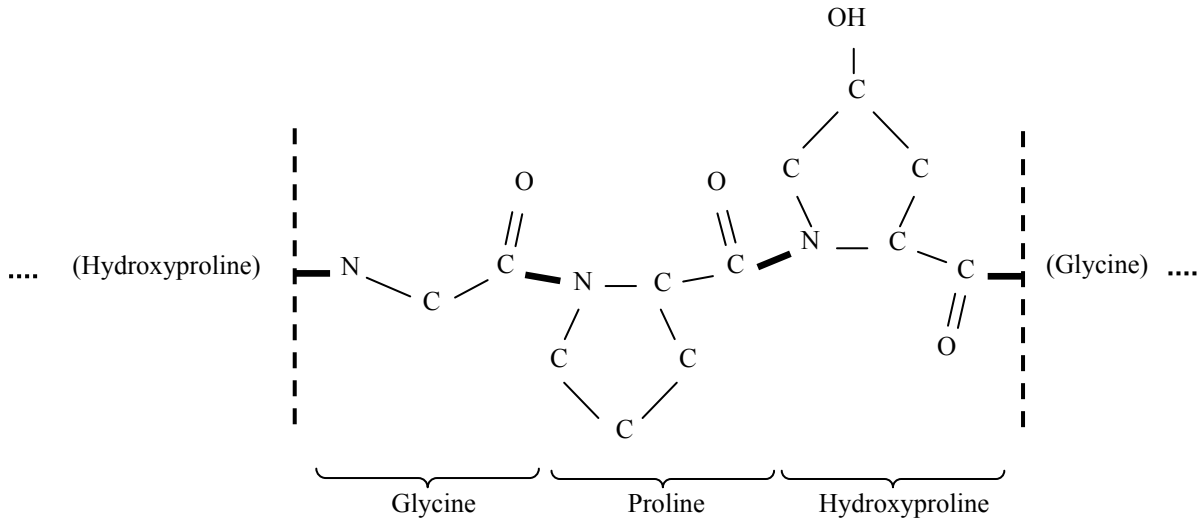

Figure 1-4. Simplified collagen structure of the human cornea, taken from reference 8

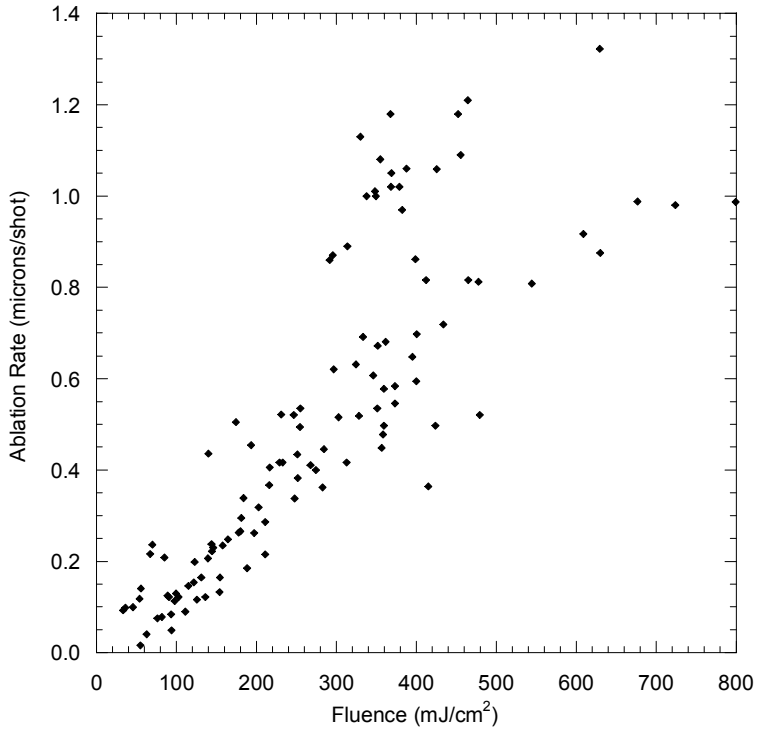

Figure 1-5. Ablation rate (microns/shot) verses Fluence (mJ/cm2) summary of reported values in the literature, taken from reference 14

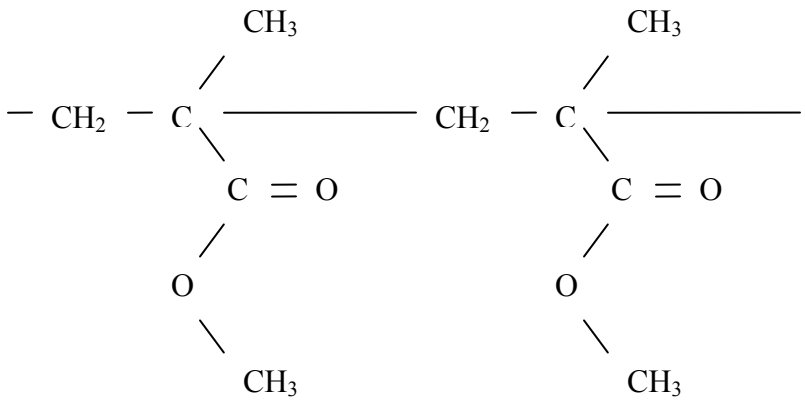

Figure 1-6. PMMA molecule, adapted from reference 47

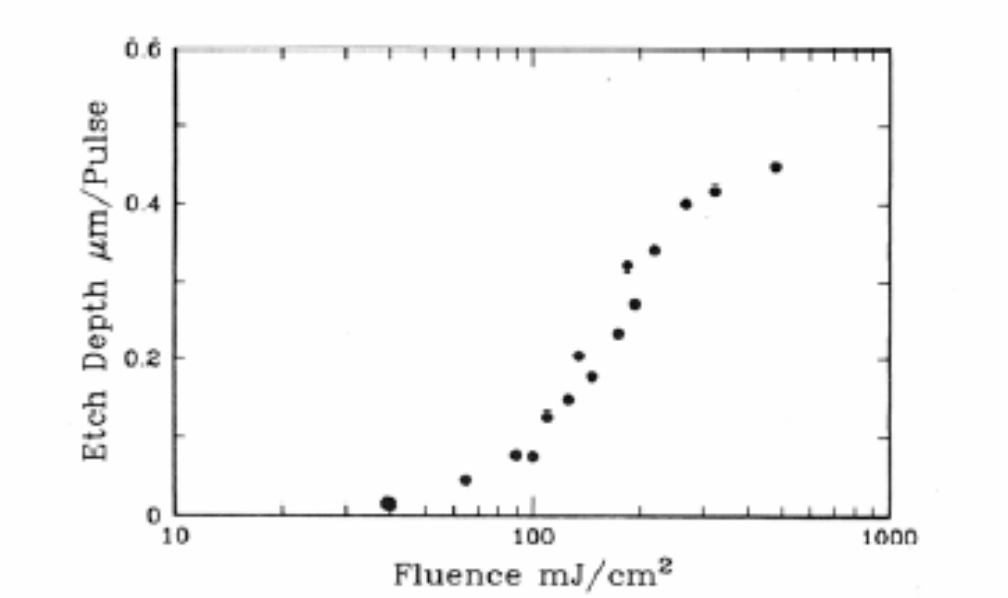

Figure 1-7. Semi-log plot of etch depth verses fluence in PMMA at 193 nm, taken from reference 49

Table 1-1. Selected molecular bonds in tissue and their dissociation energies (eV), adapted from reference 5

Molecular bond	Dissociation energy (eV)	Molecular bond	Dissociation energy (eV)
C = O	7.5	N – H	4.1
C =C	6.4	C – O	3.6
O – H	4.8	C – C	3.6
C – H	4.3	C – N	3.0

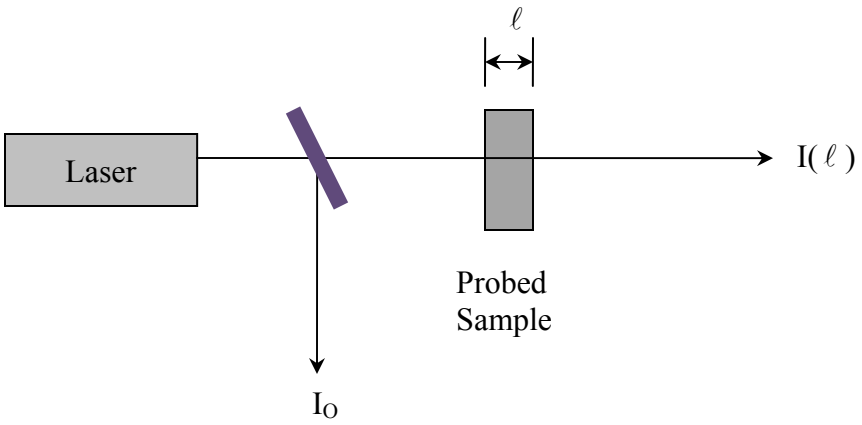

Figure 1-8. A typical transmission experiment setup

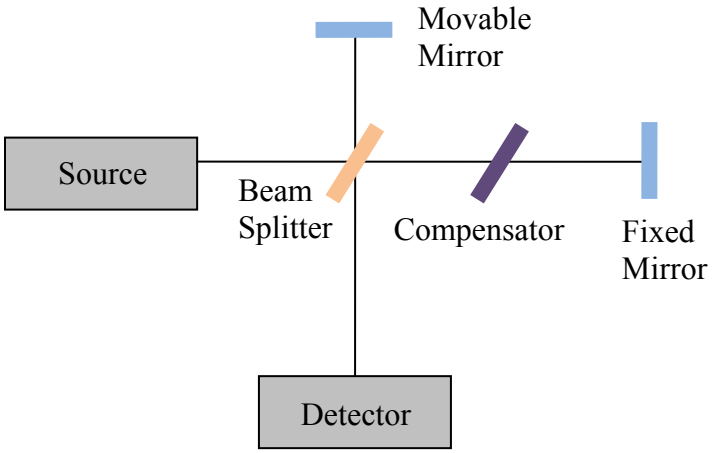

Figure 1-9. The setup of a traditional Michelson interferometer

CHAPTER 2
PLUME DYNAMICS

The dynamics of the corneal ablation ejection plume are outlined and discussed in this chapter. The experiments presented include both plume imaging and transmission measurements which are used together to understand possible effects of increasing laser repetition rate on the corneal tissue ablation process.

Experimental Setup and Methods

In all experiments involving bovine eyes, the specimens were obtained with IUCAC approval (#B220) from the University of Florida Animal Sciences Department slaughterhouse. Whole eye globes were extracted immediately following sacrifice (less than 20 minutes) and placed in sealed, buffered saline solution-filled plastic bags and kept at room temperature. Experiments were always performed within several hours following animal sacrifice. Prior to all ablations, the corneal surface was mechanically de-epithelialized using a scalpel edge.

In all studies, the TUI (Santa Clara, CA) ArF excimer laser output energy was nominally 3 mJ per pulse at the corneal eye plane and the focal spot size was approximately 0.83 mm. The laser is capable of producing laser repletion rates from 1 Hz to above 400 Hz. Alcon proprietary software controlled the delivery of a specified refractive correction over a 6-mm treatment zone using a flying spot spiraling algorithm. As in clinical settings, the laser beam was oriented downward onto the bovine eye. The surgical 193-nm ArF excimer laser beam (Laser 1 in Figures 2-1 and 2-2) passes through a beam homogenizer, a focusing lens and a pinhole before entering the scan cube. The scan cube contains two orthogonal mirrors that move in concert to generate a correction profile at the corneal plane. After exiting the scan cube, the beam then passes through a second focusing lens and two mirrors and is projected downward onto the corneal surface. The

bovine eye globe was held in a specially designed holder to keep it static and taut during the procedure.

Plume Imaging

To assess the ablation plume dynamics, planar laser light scattering measurements were performed. An Andor iStar iCCD camera (1024 X 1024 pixels) was used to record images of the plume. For imaging, a Nd:YAG pulsed solid-state laser (Laser 2) at 532 nm was used to illuminate the ablation plume, as shown in Figure 2-1. A cylindrical lens was used to create a vertical sheet of light which passed above the corneal surface normal to the camera.

Using digital delay generators, the pulsed Nd:Yag light was synchronized to the ablating excimer laser pulse. Due to internal delays in the system, the minimum delay between Laser 1 and Laser 2 shots was 121.3 μs. The jitter in the system was approximately +/- 50 ns, an order of magnitude lower than the timescales examined in these experiments. By adjusting the delay between the two lasers, the temporal evolution of the ablation plume was imaged for delays ranging from approximately 121 μs to 40 ms following the excimer laser pulse, noting that a delay time of zero corresponds to coincident laser pulses. The method of using scattered light to image an ablation plume is well documented and dates back to the pioneering work of Puliafito and co-workers [67, 69, 70].

Plume Transmission

To further analyze the ablation plume evolution, transmission measurements through the plume were analyzed. For this experiment, a secondary 193-nm ArF laser beam was used to probe the ablation plume, including interactions with solid phase (i.e. particulate) and gas phase components.

The path of the surgical ArF laser (Laser 1) for these studies was identical to that described above. The GAM (Orlando, Florida) excimer laser beam (Laser 3) was split into two paths, considered the incident and transmitted, using a glass quartz flat as a beam splitter. The incident beam path passes through the quartz flat, then through a set of neutral density filters to ensure signal linearity, an aperture to minimize stray light, a 193-nm line filter to eliminate any laser-induced fluorescence signal, and finally into the detector (200-ps rise-time photodiode). The transmitted beam path follows a similar path of optics but is passed through the center of the ablation plume at a height of 2 mm above the corneal surface. Figure 2-2 demonstrates the configuration used for this set of experiments. This general method has been successfully implemented in the analysis of ablation plume dynamics [70].

The incident probe signal was compared to the transmitted signal to determine the transmission. The ratio of the integrated transmitted signal to the integrated incident signal normalized to the ratio with no plume present defines the transmission. In general terms, the transmission is defined as

$$\tau = \frac{I(\ell)}{I_0}, \tag{2-1}$$

where $I(\ell)$ is the intensity of the laser light after passing through the plume path length, ℓ, and I_0 is the incident laser intensity. Thus, the normalized ratio (i.e. plume/no plume) is the transmission through the ablation plume. Using digital delay generators, the transmission of the plume was determined as a function of time with respect to Laser 1, as in the plume dynamics study above, for delays ranging from 0 μs to 40 ms.

The transmission of light through the ejected plume couples with the plume images to assess whether the material removal mechanism is altered by residual plume material from previous laser shots. Recalling that the probe laser passes at a distance of 2 mm above the

ablation plane, the period of minimum transmission should correlate to the brightest spot in the scattering image (temporally) at this location. Likewise, as the transmission recovers towards unity, the plume should be dissipating into the environment.

Plume Dynamics Results

Plume Imaging

Two full sets of images following the temporal evolution of the plume were recorded with the imaging laser (Laser 2) running at 2 Hz. Each image set was performed on a fresh bovine eye. Both sets begin at approximately 120 μs and end at over 30 ms with respect to the ablating laser. This recorded temporal evolution of the ablation plume shows the behavior of the plume ejection and time scale of plume dissipation. This evolution is pictured in Figure 2-3. Each image is a single capture from the iCCD camera. The time scale represents the delay of the image with respect to the surgical laser (Laser 1) pulse. From these images, one can see the "mushroom cloud" of the plume initiate and then dissolve into the surrounding environment. As observed in the figure, a column of ablated material ejects above the surface, and side vortices develop and expand with time. The column grows, and the vortices rise and spread as the plume travels away from the ablation surface, due to the ejection velocity.

An important question concerns the potential plume effect resulting from increasing the laser repetition rate from 60 to 400 Hz. To answer the question of shot-to-shot plume effects, the evolution of the plume at 1/60 (16,7 ms) and 1/400 seconds (2.5 ms) are compared. Plume images at long times (2.5 ms and 9 ms) are shown in Figure 2-4. At these long time frames, it is difficult to glean an obvious difference between the plumes (particularly in the central region, which corresponds to the surgical beam path).

To further analyze the plumes in a quantitative manner, the average scattering intensity was calculated at each time frame. The average scattering intensity was determined by dividing

the sum of the intensity at all pixels by the total number of pixels, then subtracting off the average intensity of the background (i.e. image with no plume present). The results of these calculations for both sets of data are plotted in Figure 2-5.

The average scattering intensity decays rapidly in the first 5 ms after the plume ejection, then begins to level off into a slow decay. This plot correlates well with the images themselves, which show a similar trend. The data indicate a threshold of about 2–3 ms, beyond which one would anticipate negligible interaction of the incident laser beam with the ablation plume from the previous pulse. At 400 Hz laser repetition rate, the pulse-to-pulse spacing is 2.5 ms, which is consistent for this time scale, hence no significant effects are expected from interactions of the laser pulse with the bulk ablation plume for laser repetition rates up to about 400 Hz.

Plume Transmission

To further corroborate the imaging studies, transmission measurements were performed to ensure that the laser energy of the ablation beam is not truncated by excess plume material lingering in the beam path. Transmission experiments were repeated on six bovine eyes. The delay range of the experiment began at 171.3 μs up to 1 ms. Three transmission measurements were taken at each delay time per eye. The average transmission of the 193-nm probe laser is plotted in Figure 2-6 as a function of delay time following the ablating laser pulse (time=zero), hence the time axis represents the delay of the probe excimer beam (Laser 3) with respect to the ablation pulse (Laser 1). The error bars on the plot represent one standard deviation.

The transmission profile shows a minimum of about 91% at a delay time between 120–250 μs, which corresponds to the passage of the bulk ablation debris through the probe beam at the probe beam height of 2 mm above the corneal surface, as shown in the plume imaging study. After the bulk of the plume evolves away, the transmission steadily climbs to 98.4%, rather than

100%. Examination of Figure 2-6 reveals that the transmission value of about 98.4% is persistent at the earliest delay times as well, namely between 1 and 10 μs. It is noted that these early times are well before the arrival of the bulk ablation plume.

In order to examine the cause of this overall decrease in transmission, the ArF probe beam experiments were preformed again, but without a target at the ablation laser focal plane. This experiment was designed to determine if environmental factors, namely a build-up of ozone in the ablation area, are the cause of the observed transmission loss. These control transmission measurements were determined in the same way as their corneal counterparts, but with no target present. A shutter was placed between the Alcon laser (Laser 1) and the target area. The ratio of probe laser transmission was calculated by normalizing the transmission with the Laser 1 shutter open to the transmission with the Laser 1 shutter closed by alternatively opening and shutting the shutter. Just as with the corneal target, these experiments were performed at various delays. As the probe laser passes through the Alcon laser path at different delay times, any effect of enhanced absorption (e.g. Ozone formation) responsible for the ~2% transmission drop noted above should be apparent. If ozone formation is responsible for the transmission loss, a maximum transmission of approximately 98% should be achieved. The results in Figure 2-7 do not show such a drop in transmission, indicating that ozone is not the source for the transmission loss. Therefore, additional measurements were pursued.

A final set of experiments was performed to further assess the transmission loss of the ArF probe laser through the ablation plume under ablative conditions. Because the 2% drop in transmission appears to be long lived, one goal was to explore the possible effects of ablation rate; hence measurements were recorded at 60 Hz and 400 Hz. As the ability to synchronize the ablating laser and probe laser was not possible at 400 Hz, the transmission measurements were

done without any laser-laser synchronization. The ablating laser was run at either 60 Hz or 400 Hz, and the probe laser was run at a constant rate of 50 Hz. This setup does not have the capability to study the temporal evolution of the transmission, but rather yields an average transmission. This average transmission of 20 probe laser pulses was repeated for six ablation sites for each bovine eye samples.

These measurements were performed in quiescent air and then repeated with addition of a nitrogen purge cross flow jet. The cross flow was achieved by placing a piece of rigid tube 1 cm from the ablating laser pulse, aligned at the height of the probe laser, as shown in Figure 2-8. A flow of dry nitrogen (10 liters per minute) formed the cross-flow jet. The tube was orthogonal to the direction of the probe laser, with both the tube and probe laser in the same plane, approximately 2 mm above the target surface. With this configuration, the transmission measurements were repeated. At each repetition rate and flow condition, 2 bovine eye samples were used.

It was observed that by adding a cross flow of dry nitrogen to purge the beam path allowed the transmission to reach unity at a time scale of 1.25 ms. Transmission measurements were recorded for both laser repetition rates (60 and 400 Hz) with cross flow added. The results are shown in Figure 2-9, for both 60 and 400 Hz. With the nitrogen purge flow, the transmission is increased to 100.4% (σ=0.49%) and 99.9% (σ=0.95%) for the 60- and 400-Hz experiments, respectively. Together, the data suggest that a diffuse, gas-phase component accumulates above the ablation surface and slightly attenuates the incoming laser pulse. However, no significant laser repetition rate effect is observed for this diffuse plume component. Clinically, this diffuse component is most likely diminished by the exhaust systems (i.e. plume extractors) that are

present on commercial refractive systems, although the degree to which it might exist is difficult to predict.

The average probe transmission value of the 60 Hz ablation with no flow is again statistically indistinguishable from that at 400 Hz ablation with no flow.

Plume Dynamics Summary

Qualitatively, the bulk of the ablation plume is observed to dissipate on a time-scale of about 3 ms to about 98% transmission. Likewise, the average scattering intensity decays rapidly in the first few ms after the plume ejection, then begins to level off into a slow decay. At 400 Hz laser repetition rate, the pulse-to-pulse spacing is 2.5 ms, which is consistent for this time scale, hence no significant effects are expected from interactions of the laser pulse with the bulk ablation plume for laser repetition rates up to 400 Hz.

The transmission profile shows a minimum of about 91% at a delay time between 120–250 μs, which corresponds to the passage of the bulk ablation debris through the probe beam at the probe beam height of 2 mm above the corneal surface, as shown in the plume imaging study. After the bulk of the plume evolves away, the transmission steadily climbs to 98.4%, rather than unity. With the addition of nitrogen purge flow, the transmission for both 60 and 400 Hz resolves to unity. This data corroborates the conclusion that a long-lived component of gaseous-phase (or very fine aerosol phase) ablation products appear to blanket the target during ablation. This component is easily blown away from the ablation area. This component does not have a rate effect, and is likely mitigated by plume evacuators present on many clinical systems. Given the current findings, no rate dependence is expected over the range of 60 to 400 Hz examined here.

Direct comparisons with previous plume dynamics studies are difficult, as each study uses a specific set of experimental conditions, namely fluence, wavelength and laser beam diameter

(spot size). However, the trends noted here are consistent with the literature. The early images of Puliafito and co-workers show a similar plume evolution scheme with quicker dissipation than was noted here, which is expected due to the higher laser fluence used [69]. The time-scales are also very consistent with the plume velocities on the order of 10 m/s reported by Hahn *et al*. for an average (full-beam) fluence of 100 mJ/pulse [68]. Noack and co-workers reported that laser shielding by build-up of plume material is significant for large beams, noting that plumes generated by smaller-diameter laser beams, such as 1 mm, dissipate much quicker than their large-diameter counterparts [67]. The current study has found that laser shielding is insignificant for ablation with a 1-mm spot size at rates up to approximately 400 Hz. Pettit and Ediger found that the transmission through the ablation plume and excised cornea combined was minimized at 30 μs at a value of 40% [79]. It is not expected that the reported transmission values match those determined here, as their probe wavelength was 355 nm and the pathlength included the actual cornea itself, which is highly absorbing in the UV region. However, the evolution of transmission over time is consistent with the current findings. From their data, it appears that they also observed the lack of resolution of transmission to 100% at longer time scales.

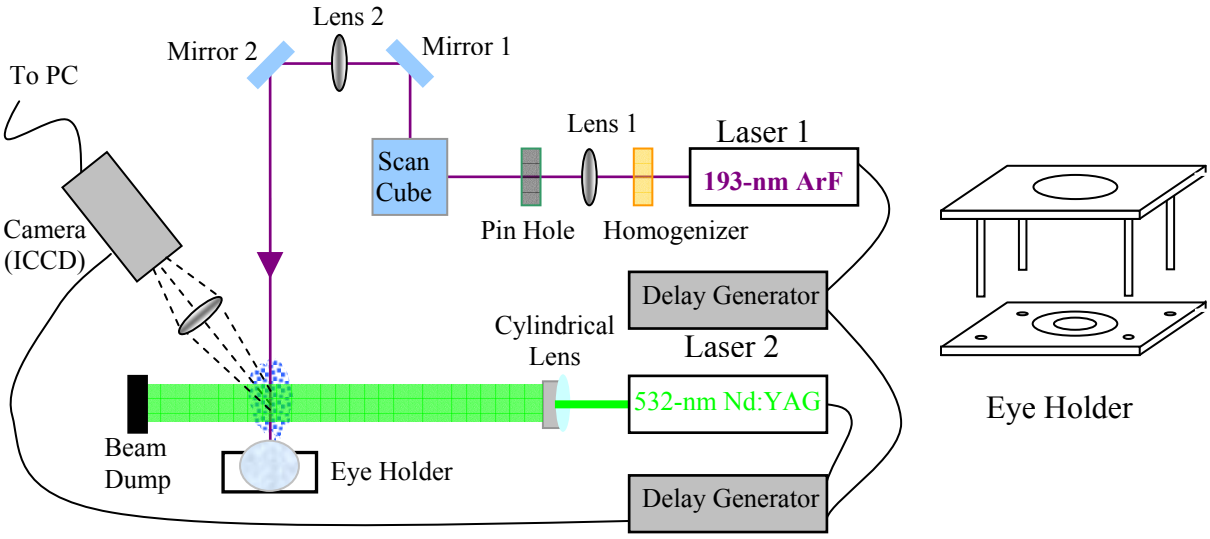

Figure 2-1. Experimental set-up for measuring ablation plume dynamics

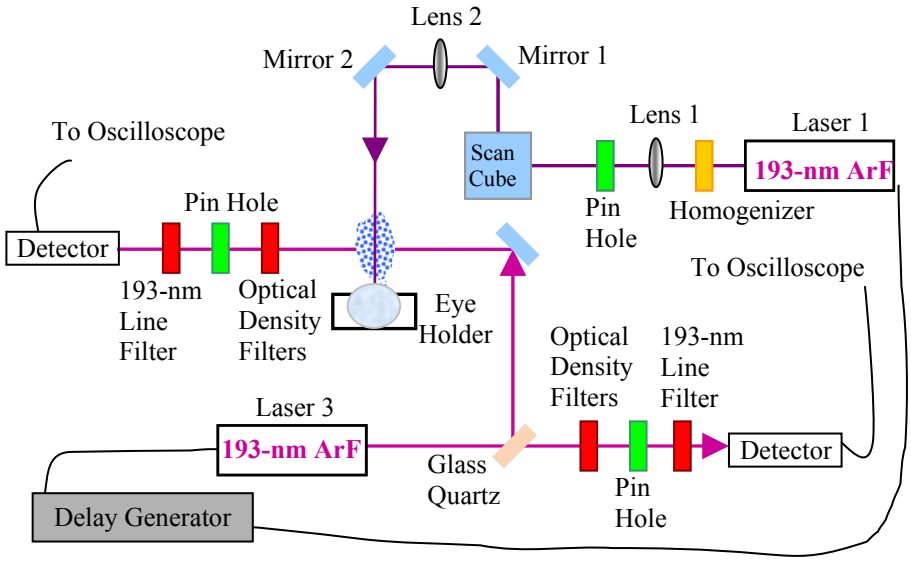

Figure 2-2. Schematic of the transmission studies setup

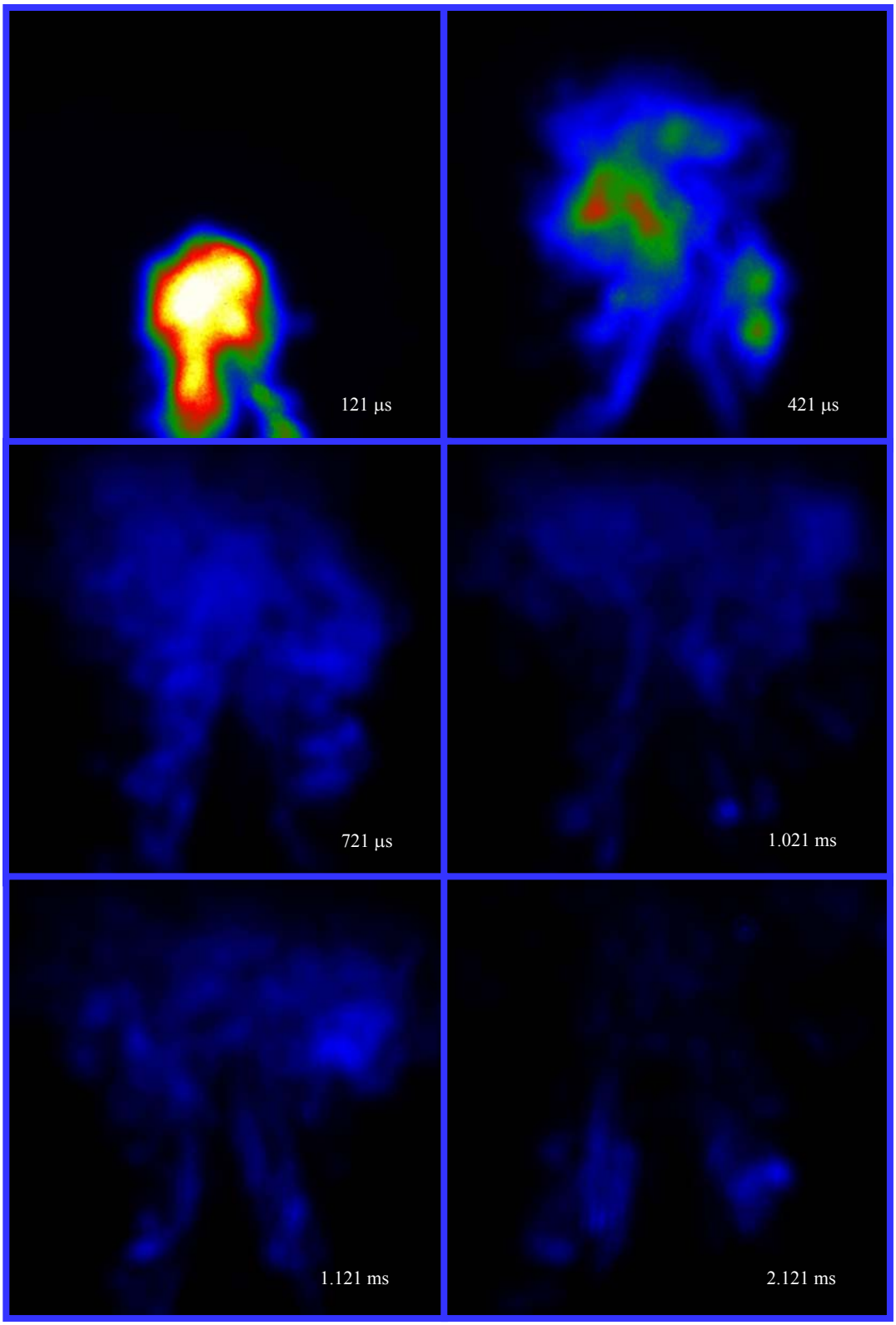

Figure 2-3. Ablation plume images as a function of time following the ablating laser pulse. All images have the same intensity scale.

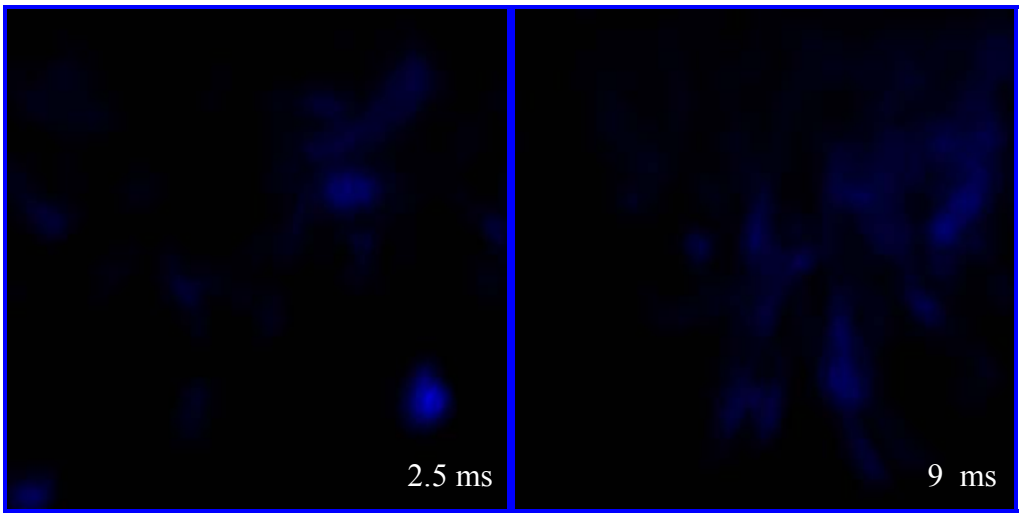

Figure 2-4. Long time scale ablation plume images. All images have the same intensity scale.

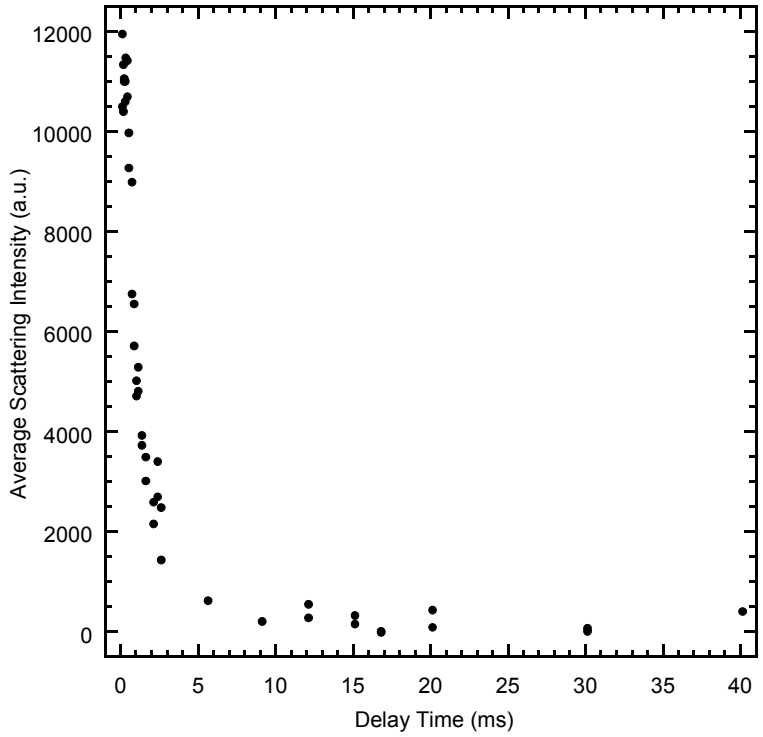

Figure 2-5. The average scattering intensity (full-image) of the ablation plume images as a function of time following the ablating laser pulse with a 2 Hz repetition rate

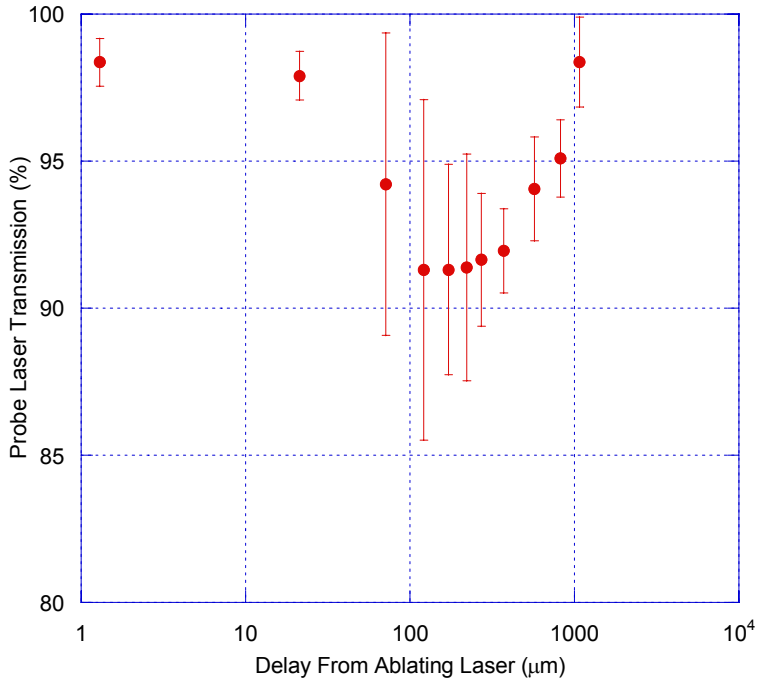

Figure 2-6. ArF probe laser transmission through the ablation plume as a function of time following ablation. Transmission was recorded at a fixed height of ~2 mm above cornea surface. Error bars are equal to one standard deviation.

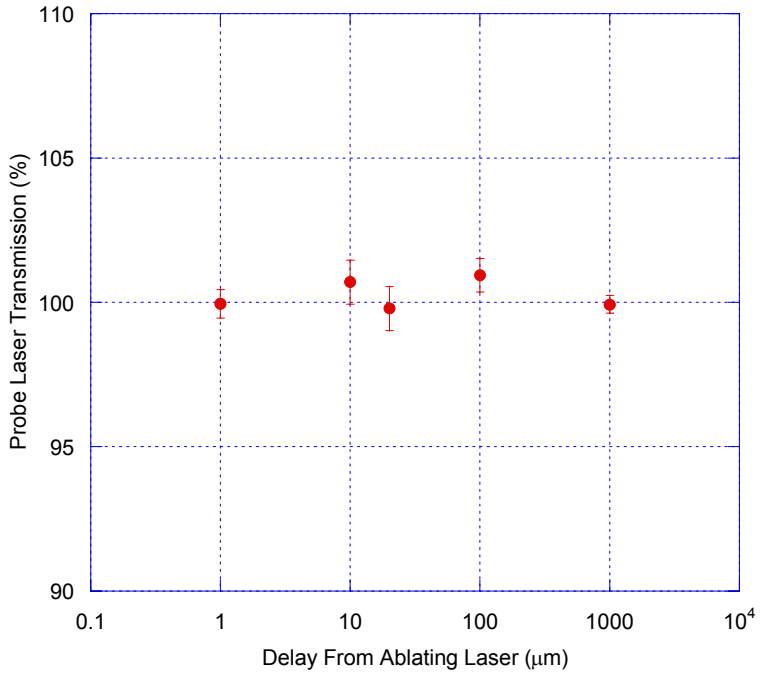

Figure 2-7. Transmission of ArF probe beam through non-ablating beam path. Error bars represent one standard deviation.

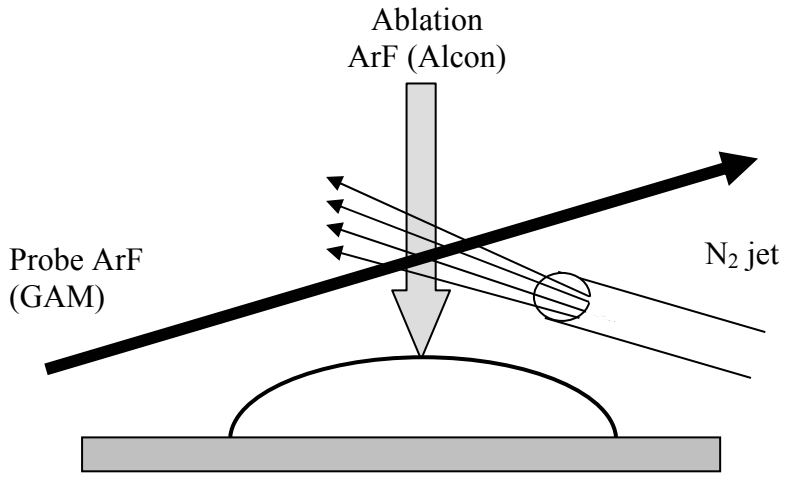

Figure 2-8. Configuration of the nitrogen purge jet for the transmission loss experiment

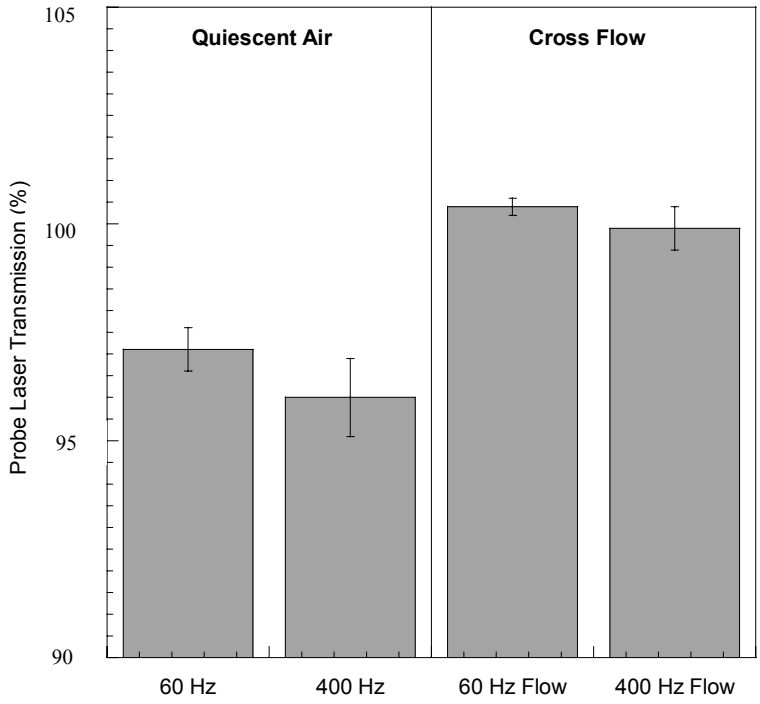

Figure 2-9. Average transmission of the ArF probe laser at a fixed delay of 1.25 ms and fixed height of ~2 mm. Error bars are equal to one standard deviation.

CHAPTER 3
ABLATION PROFILES

When varying surgical parameters, such as laser repetition rate, it is essential that the geometry of the corneal resculpting remain the same. In this chapter, the possible impact of laser repetition rate upon ablation profiles is analyzed.

Experimental Setup and Methods

In all cases, the TUI (Santa Clara, CA) ArF excimer laser output energy was nominally 2.7–3.0 mJ per pulse at the corneal eye plane and the spot size was approximately 1 mm. The laser is capable of producing laser repletion rates from 1 Hz to above 400 Hz. Alcon proprietary software controlled the delivery of a specified refractive correction over a 6-mm treatment zone. As in clinical settings, the laser beam was oriented downward onto the treated material.

Wax Ablation Profiles

To ensure successful clinical outcome, it is crucial that the overall ablation profiles generated at the relevant laser repetition rates are statistically identical for a given refractive correction. The ablation depth generated by a particular system is a function of the incident laser fluence, with higher fluences producing deeper ablation depths.

In order to assess any variations in the profiles generated by varying the laser repetition rate, corneal tissue ablation craters were analyzed. Two types of ablation were performed. For the initial set of experiments, a straight bore ablation was executed, where each successive shot was directed to the same spot on the cornea. A second set of experiments was completed using a scanning operation in which ablation craters were generated by superimposing a 25-shot sequence in the center of a 3-diopter, 6-mm zone ablation. The treatment was performed with the laser operating at rates of either 60 and 400 Hz using paired eyes from each bovine. Hence, one eye received the treatment at 60 Hz, and the second eye received the treatment at 400 Hz. Using

superimposed shots on a standard profile provided a more clinical representation than a simple static laser beam because in clinical applications the time between laser pulses at a given location is significantly greater than the pulse-to-pulse firing time due to the scanning algorithm employed by the laser system. The system used to generate these patterns is sketched in Figure 3-1. The surgical 193-nm ArF excimer laser beam (Laser 1) passes through a beam homogenizer, a focusing lens and a pinhole before entering the scan cube. The scan cube contains two orthogonal mirrors that move in concert to generate a correction profile at the corneal plane. After exiting the scan cube, the beam then passes through a second focusing lens and two mirrors and is projected downward onto the corneal surface. The bovine eye globe was held in a specially designed holder to keep it static and taut during the procedure. The intraocular pressure was not measured in this set of experiments; however, the weight of the top of the eye holder was used to keep a consistent pressure on all eyes. The purpose of keeping the eye surface taut was to prevent aberrations in the ablations from shriveling of the bovine eyes, which naturally occurs following excision. Not shown in the figure are two alignment lasers. The first is a diode laser that runs through the center of the cavity of Laser 1 and allows the beam of Laser 1 to be centered on the target (cornea). The second is a diode laser that is set to a height matching the ablation plane (the plane at which the spot of Laser 1 is minimized) and allows the target to be set in the ablation plane.

In all experiments, whole bovine eye globes were extracted immediately following sacrifice (less than 20 minutes) and placed in sealed, buffered saline solution-filled plastic bags and kept at room temperature. Experiments were always performed within several hours following animal sacrifice. Prior to all ablations, the corneal surface was mechanically de-epithelialized using a scalpel edge.

Immediately following completion of the ablation, impressions of the craters were prepared using single drops of paraffin wax as previously documented [50]. Once the wax was thoroughly solidified, the impression was inverted and transferred to a microscope slide. A Zygo NewView white-light interferometer was then used to examine the impressions to obtain 3-dimensional images of the full craters. The interferometer was outfitted with a 5X Michelson objective with a 0.5X magnification setting resulting in a net 2.5X surface view. Five eyes were analyzed at each laser repetition rate (10 eyes total). Figure 3-2 is a representative three-dimensional model of a straight-bore ablation impression. Figure 3-3 is a representative three-dimensional model of a scanning ablation impression. At this stage, it virtually impossible to distinguish the two ablation algorithms apart.

In order to process the images, six 2-dimensional cross sections were extracted from each 3-dimensional interferogram using a star pattern such that each cross-section bisected the center of the ablation crater as shown in Figure 3-4 for a wax impression of a straight-bore ablation and Figure 3-6 for a wax impression of a scanning ablation. The corresponding cross-sections are shown in Figure 3-5 and Figure 3-7, respectively. Figures 3-2 through 3-7 were all obtained from the MetroPro software that accompanies the Zygo New View interferometer. The cross-sections were then exported from MetroPro as text files for further processing in Microsoft Excel.

Parabolic trend lines, which provided good approximations of the corneal surface near the ablation site ($r^2 > 0.9$), were used to subtract the overall corneal surface curvature from each cross section, yielding the ablation profiles. The necessity of this can be seen by examining Figure 3-5. There is an overall curvature to the cross-section that is not negligible. Without this subtraction, the ablation profiles obtained would be artificially low. Also, the cross-sections would be skewed in varying directions, as centering the ablation impression on the interferogram

is difficult to do on a curved sample. The six subtracted cross sections were then combined and smoothed to yield the final ablation profile for each treated cornea. The parabolic trendlines represent the geometry of the cornea in the case of the straight-bore ablations. In the case of the scanning ablations, the trendlines represent the overall 3-diopter myopic correction geometry, as the few millimeter field of view of the interferometer is less than the 6-mm correction zone. The overall steepness of the wax impression is less in Figure 3-7 than in Figure 3-5. This is the anticipated outcome, as a myopic correction (-3 diopters in this case) flattens the cornea in the ablation zone.

Plastic Ablation Profiles

Ablations were performed on PMMA samples as well as corneal samples. PMMA remains static post-ablation, eliminating the requirement of wax samples. Instead, white-light interferometry was performed directly on the PMMA surface. This allows for cleaner interferometry images of the samples for three reasons. First the wax samples contain voids associated with the solidification process, although such effects were shown to be minimal [50]. Second, in the case of PMMA, interferometry is performed on the sample directly, as opposed to an impression of the sample. This eliminates transfer errors associated with the mold process. Finally, the PMMA samples are flat, leading to clearer interferometry, as there is no drop-out associated with the linear height range of the instrument. As PMMA has been successfully used to model corneal ablation behavior, PMMA experiments can be used to confirm the results of the corneal ablation profile study, as well as to investigate other topics.

The same experimental setup described in the above section for corneal ablation profiles (Figure 3-1) was utilized for examining plastic ablation profiles. The PMMA samples were placed on top of the eye holder, which was used to adjust the top surface of the polymer into the surgical (focus) plane. Once the ablations were performed, the PMMA samples were examined

with white-light interferometry in the same manner as the corneal samples. Both straight-bore and scanning ablations were performed on the PMMA samples. Figures 3-8 and 3-10 show representative three-dimensional scans of ablation craters on PMMA for straight-bore and scanning ablations, respectively. Figures 3-9 and 3-11 show the corresponding cross-sections for straight-bore and scanning ablations, respectively.

The three-dimensional scans from PMMA can be compared with those from the wax impressions (Figures 3-2 and 3-3). The PMMA scans are much smoother as expected. One notable exception that differentiates the PMMA analysis from the wax impression analysis is obvious from Figure 3-9. Since the surface of the PMMA is flat, parabolic trendlines for the overall geometry is no longer applicable. Thus, in the case of straight-bore ablation of the PMMA samples, linear trendlines were used. Note that the cross-sections in Figure 3-11 are similar to those in 3-9, as anticipated, as the same -3 diopter correction for myopia was performed in both cases. What separates these two figures is the smoothness of the cross-sections in Figure 3-11.

Imaged Ablation Profiles

An entirely separate imaging technique was also developed implemented to determine corneal ablation profiles. The ablations were performed in the same way as in the wax ablation studies, with the addition of two imaging cameras. A Princeton iCCD camera (model 7489-0001) was used to center the curvature of the cornea in the direction orthogonal to the second camera. When the cornea is properly centered on this alignment camera, the ablation will be performed on the apex of the cornea. This is essential to the measurements in these experiments. The second camera was used to record images of the corneal profile pre and post-operatively. The experimental setup is outlined in Figure 3-12.

The concept of this technique is straightforward: a profile image of the cornea is taken with an Andor iCCD camera both pre- and post-operatively, and the pre image is subtracted from the post image. This difference between the two ablation profiles is the ablation profile. Each saved image was an average of 10 exposures. Figure 3-13 is an example image from the Andor camera. There is a clear definition between the eye (bottom section of the frame) and the surroundings (top section of the frame). In order to quantify this border, an edge finding technique was employed using MatLab. Text files from the Andor camera were manipulated using MatLab to determine the location of the corneal surface. The individual vertical pixel vectors have three distinct zones: a low flat line representing the eye, a transition zone, and a high flat line representing the surroundings. The low and high lines were averaged over several pixels to determine values for the eye and surroundings, respectively. These values were averaged, and the resulting value is considered the surface of the eye. This operation is performed for each horizontal pixel location. Shown on Figure 3-13 is a dark line that represents the edge found using this algorithm. The line is nicely consistent across the entire profile. The MatLab codes used to achieve the edge profiles are in Appendices A and B. The ablations were performed at 92 Hz.

Ablation Profile Results

Wax Ablation Profiles

The straight-bore ablation experiments will be discussed first, then the scanning ablation experiments. The straight-bore ablations of bovine corneal tissues were performed at nominally 3.0 mJ/pulse. The laser repetition rate was varied while the number of shots remained a constant 20 shots. Ablations were performed on seven bovine eyes. Four ablations were performed on each eye. Each ablation was performed on a separate corneal site, one at each of the following laser repetition rates: 1, 10, 50 and 300 Hz. This experiment will ascertain whether or not the

ablation rate (overall depth removed per laser pulse) varies with the laser repetition rate. Not every wax impression of the straight-bore ablations was viable. In some cases, voids in the wax sample were located over the ablation impression. Four usable interferograms were obtained for the 1 Hz samples, while three usable interferograms were obtained for each of the remaining laser repetition rates. The overall depths (the depth at the center of the profile) and corresponding standard deviations for each interferogram are listed in Table 3-1. The final ablation profiles obtained from each interferogram for each laser repetition rate were combined and smoothed to yield the final profile for each rate, as shown in Figure 3-14. The overall and corresponding standard deviations for each laser repetition rate are listed in Table 3-2.

The width of the profiles in Figure 3-14 is constant as the laser repetition rate increases. Also, the overall ablation depth is also consistent across the profile. The profile created at 1 Hz is slightly deeper than that of the other repetition rates. This is quantified in Table 3-2. This is likely due to unstable laser energy at 1 Hz, which is well below the intended operation range of the Alcon system. Finally, the average ablation rate (overall depth removed per laser pulse) was calculated to be 0.98 μm/shot, based on the 10, 50 and 300 Hz data, which is consistent with Fisher & Hahn, 2004b.

Scanning ablation experiments were also performed on bovine corneas. This set of experiments had two purposes. First, ablations at 60 and 400 Hz were compared for potential rate effects. Second, a plume evacuator created by and borrowed from Alcon was temporarily put into place to determine if the ablation profile is affected by slight vacuum suction. The vacuum suction applied by the plume evacuator was so slight, that it could not be felt, nor did it disturb tissue paper placed on the cornea. The intent of the evacuator is to remove plume material from the ablation area in order to reduce the odor associated with surgery. Five bovine corneas each

were ablated using 60 Hz ablations and 400 Hz ablations without the plume evacuator in place. Three bovine corneas were ablated using 400 Hz ablations with the plume evacuator in place. All ablations were performed at laser energy of 2.7 mJ/pulse. As in the straight-bore ablations, not every wax impression was viable. In some cases, voids in the wax sample were located over the ablation impression. Two usable interferograms were obtained for the 400 Hz samples with vacuum applied, while for usable interferograms were obtained for both of the laser repetition rates without vacuum applied. The overall depths (the depth at the center of the profile) and corresponding standard deviations for each interferogram are listed in Table 3-3. The final ablation profiles obtained from each interferogram for each laser repetition rate were combined and smoothed to yield the final profile for each rate, as shown in Figure 3-15. The overall and corresponding standard deviations for each laser repetition rate and vacuum condition are listed in Table 3-4.

The width of the profiles in Figure 3-15 is constant as the laser repetition rate increases with the number of shots. Also, the overall ablation depth is also consistent across the profile. This is quantified in Table 3-3. No differences in the profiles or ablation depths are noted between 60 Hz and 400 Hz. Additionally, the presence of the plume evacuator does not appear to alter the ablation profile or overall ablation depth. This result is anticipated based on the plume imaging and transmission studies above, as the plume has developed beyond the immediate vicinity of the laser pulse. Finally, the average ablation rate (overall depth removed per laser pulse) was calculated to be 0.95 μm/shot, which is consistent with Fisher & Hahn, 2004b.

Plastic Ablation Profiles

The straight-bore ablation experiments will be discussed first, then the scanning ablation experiments. First, the number of shots applied in a single ablation was varied as the number of

shots remained a constant 1 Hz. Two ablations were performed for each of the following number of shots: 5, 10, 15, 20 and 25. This experiment will ascertain whether or not the ablation rate (overall depth removed per laser pulse) varies with the number of shots. The two final ablation profiles for each number of shots were combined and smoothed to yield the final profile for each number of shots, as shown in Figure 3-16. The overall depths (the depth at the center of the profile) are shown in Figure 3-17 with a linear trendline applied for easy visual comparison. The equation of the linear regression line is $y = 0.173x + 0.107$ with an R value of 0.996. Finally, the ablation rates (overall depth removed per laser pulse) were calculated as shown in Figure 3-18.

It can be seen from the above three figures that the ablation rate (μm/shot) is a constant 0.18 μm/shot (σ=0.009) from 5-25 laser pulses at 1 Hz. No incubation effects are present after 5 pulses of the laser. Also, it is interesting to examine the growth of the ablation shown in Figure 16. The width of the profile is constant as the depth increases with the number of shots. The progression of the profile is in the depth only.

An Ophir Beamstar-FX-33 beam profiler was used to record the laser beam profile for comparison with the ablation profiles observed in the PMMA samples. Figure 3-19 shows the fluence profile (mJ/cm^2) of the Alcon excimer laser beam recorded with Ophir's Beamstar program.

The ablation profiles in Figure 3-16 and the fluence profile in Figure 3-19 can be combined to determine the ablation rate verses fluence across the entire crater. In order to do so, as both plots are scatter graphs of discrete data points, linear interpolation was utilized. The resulting data are shown in Figure 3-20.

For the second straight-bore experiment performed, the number of pulses was kept constant at 25 shots, while the laser repetition rate was varied. Three ablations were performed

for each of the following laser repetition rates: 1 Hz, 60 Hz, 230 Hz and 400 Hz. This experiment will ascertain whether or not the ablation rate (overall depth removed per laser pulse) varies with the laser repetition rate. The three final ablation profiles for each number of shots were combined and smoothed to yield the final profile for each laser repetition rate, as shown in Figure 3-21. The overall depths (the depth at the center of the profile) are shown in Figure 3-22.

First, it is interesting to note that the ablation profiles for 60, 230 and 400 Hz are indistinguishable from one another. However, at 1 Hz, the ablation profile is shallower than the other three. This observation is quantified by examination of the overall ablation depth. It can be seen from the figures that the ablation depth (μm/shot) is a constant 4.65 μm (σ=0.16) for 60 to 400 Hz for 25 shots. The ablation depth at 1 Hz, 4.33 μm (σ=0.1), is within two standard deviations of the mean depth for the other three rates. that the ablation depth (μm/shot) is a constant 4.57 μm (σ=0.22) for 1–400 Hz laser repetition rates for 25 shots. The corresponding ablation rate is 0.183 μm/shot, which compares well with the ablation rate obtained from varying the number of laser pulses (0.18μm/shot).

The ablation profiles in Figure 3-21 and the fluence profile in Figure 3-19 were also combined to determine the ablation rate verses fluence. The result is in Figure 3-23.

After the straight-bore set of experiments were performed, experiments were performed using the scanning algorithm. The scanning experiments have a dual purpose. First, ablations were performed at various rates to compare with the bovine eye studies. Second, an issue was raised by Alcon regarding the ablation algorithm. The original algorithm (stretched spiral) employs a counter-clockwise spiraling “flying spot” that moves from the center of the cornea to the edge of the ablation zone. For some systems, the algorithm was reversed (reverse spiral) to employ a clock-wise spiraling “flying spot” that moves from the edge of the ablation zone to the

center of the cornea. Given this change in algorithm, it was desirable to ensure that similar ablation results were obtained. PMMA ablations were performed for each algorithm to study the problem.

Three stretched spiral ablations and three reverse spiral algorithm ablations were performed for each of the following ablation rates: 60 Hz, 92 Hz and 400 Hz. The same general analysis techniques used for the straight-bore ablations above were used in these experiments as well. Figures 3-24 through 3-26 show the resulting ablation profile results for each laser repetition rate. The stretched and reverse spiral algorithms in Figure 3-24 are nearly impossible to distinguish from one another. The stretched (S) and reverse (R) spiral algorithms in Figure 3-25 and 3-26 are identified with arrows for clarity.

The overall ablation depths were compared to determine any rate effects or changes due to algorithm reversal. The average depths and standard deviations for each ablation (interferogram) are presented in Table 3-5. These results are presented in Figure 3-27 and Figure 3-28. Figure 3-27 is arranged for easy visual comparison of the stretched spiral and reverse spiral algorithms. Figure 3-28 is arranged for easy visual comparison of the laser repetition rates.

From this data, it is easily concluded that the algorithm does not alter the overall ablation depth of the 9-diopter correction. Particularly, this is very visible from the overlapping error bars in Figure 3-27. Also, the average overall ablation depth from all three laser repetition rates for stretched spiral and reverse spiral are 4.35 μm (σ=0.18) and 4.19 μm (σ=0.24). These values are within one standard deviation of each other. A student's t-test was performed for confirmation, and the samples may statistically be considered to have the same mean within a 95% confidence interval. Thusly, the stretched spiral and reverse spiral ablation profiles were combined and

smoothed to generate single ablation profiles and overall ablation depths for each of the three ablation rates, as shown in Figures 3-29 and 3-30.

The overall ablation depth for ablations generated at 60, 92 and 400 Hz are 4.27 μm (σ=0.16 μm), 4.36 μm (σ=0.18 μm) and 4.17 μm (σ=0.28 μm), respectively. This experiment confirms the result the scanning ablation experiments conducted on bovine corneas; increasing the laser repetition rate up to 400 Hz does not alter the ablation profile or the overall ablation depth. The ablation profiles and the fluence profile in Figure 3-19 were also combined to determine the ablation rate verses fluence. The result is in Figure 3-31.

The ablation rates of Figures 3-20, 3-23 and 3-31 (nm/shot) are consistent with the data from Srinivasan & Braren, 1989 depicted in Figure 1-7. At a fluence of 200 mJ/cm^2, the ablation rate obtained from the PMMA experiments presented in this section is approximately 90–100 nm/shot, while the published data indicates a rate of approximately 250 nm/shot. It is unclear if the graphed fluence in Figure 1-7 is the peak fluence or the average fluence. The average fluence is generally half that of the peak fluence, which would explain difference between the values.

Additionally, one can determine the threshold fluence for PMMA as approximately 25 mJ/cm^2, which is in agreement with the value of approximately 35 mJ/cm^2 obtained from Figure 1-7 [49].

Imaged Ablation Profiles

Figures 3-32 and 3-34 are examples of pre-ablation iCCD images. Figure 3-33 is the post-ablation profile of the same eye as that of Figure 3-32. Likewise, Figure 3-35 is the post-ablation profile of the same eye as that of Figure 3-34. The edge as found by the MatLab program in Appendix A is also diagrammed in the figures. The axes of the figures are pixels, and each pixel represents 5.1 microns.

Seven paired bovine eyes were analyzed. From each bovine, one eye was ablated using the stretched spiral pattern, and the second was ablated using the reverse spiral pattern. Representative ablation profiles for each algorithm are shown in Figure 3-36. For analysis, first, the pixel numbers of the reverse spiral pattern was subtracted from those of stretched spiral pattern. Using the calibration of 5.1 μm/pixel, the number of pixels composing the difference was converted to actual dimensions. Figure 3-37 is a representative differential ablation profile. Table 3-5 contains the maximum ablation depth for each bovine eye and ablation algorithm. At the bottom of the table, the averages and standard deviations for each algorithm are listed.

The maximum ablation depths are nearly identical (164.62 and 163.55 μm, for stretched spiral and reverse spiral, respectively), and the standard deviations are quite large (31.14 and 21.91 μm, for stretched spiral and reverse spiral, respectively). At this juncture it is difficult to tell any difference between the ablations generated by the stretched spiral and the reverse spiral algorithms. For further analysis, the differential ablation profiles of all seven eyes were then averaged for a final average profile. Lastly, ten pixels at each end of the profiles were averaged and the slope between them was used to subtract a baseline from the averaged profile. The final result is presented in Figure 3-38.

The differential ablation profiles show a clear pattern, similar to that of each individual ablation. However, the precision of this method is still an issue. It is very difficult to line up the cornea such that it is exactly centered on the two iCCD cameras. This challenge explains the large variation in the ablation depths, as slight translation off of the apex of the cornea will significantly alter the measured ablation depths. However, failure to achieve sufficient alignment does not affect the trend of the ablation profile trend. As such, it is impossible to clearly state (using this method) whether or not algorithm reversal has an effect on the ablation geometry.

Ablation Profile Summary

The main results come from the wax impressions and PMMA studies. From these experiments, we can clearly state that the laser repetition rate does not significantly alter the geometry of the ablation profile. The width of the ablation profiles in bovine eyes was found to be constant as the laser repetition rate increases and as the number of shots increases. Also, the overall ablation depth is also consistent across the profile for varying laser repetition rates. The average bovine cornea ablation rate (overall depth removed per laser pulse) was calculated to be 0.98 μm/shot, in the straight bore experiments and 0.95 μm/shot in the scanning experiments.

The PMMA experiments indicate that reversing the ablation algorithm does not alter the ablation geometry. These experiments also concluded that there is no statistical difference in the ablation profiles as the laser repetition rate is increased from 60 to 100 Hz. The ablation rate for PMMA was found to be approximately 0.17 μm/shot. It is very important to note here that this rate cannot be compared to the bovine cornea rate. In the literature review, it was pointed out that a conversion of 1.8 μm of corneal tissue is removed per 1.0 μm of PMMA. The laser was tuned by Alcon between the bovine corneal studies and the PMMA studies. At that time, the fluence profile of the laser beam was changed from maxing out at approximately 650 mJ/pulse to approximately 475 mJ/pulse. One would anticipate that at an equal laser output energy, the ablation depth created by the laser to decrease with decrease in peak fluence. Thus, it is not unexpected that the PMMA ablation rate relative to the corneal ablation rate is lower than expected based on the literature. Additionally, the molecular weight of PMMA is known to affect the mechanism of PMMA ablation, and thus the ablation rate [80]. This is partially responsible for the large range of reported PMMA thresholds, as well. Additionally it was determined that, in PMMA, reversal of the ablation algorithm does not affect the geometry of the ablation.

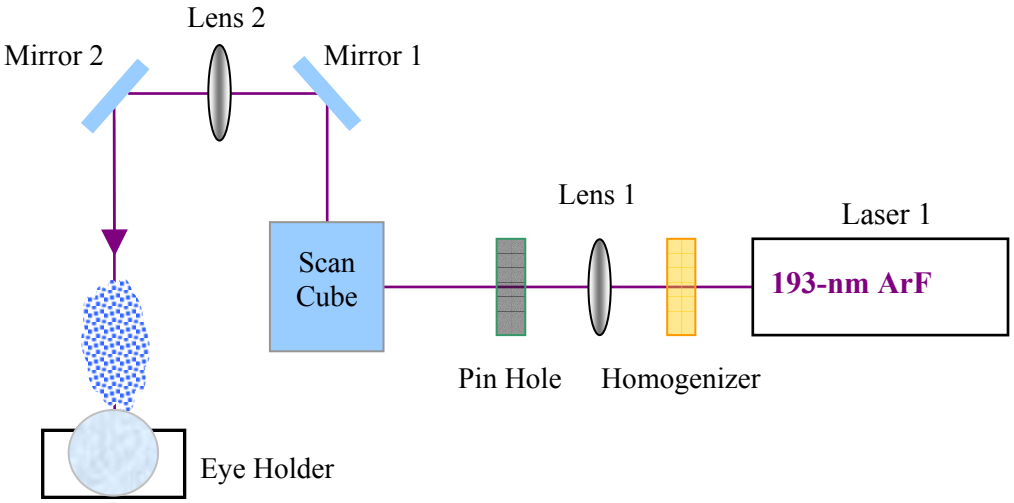

Figure 3-1. Experimental set-up for ablation of bovine corneas

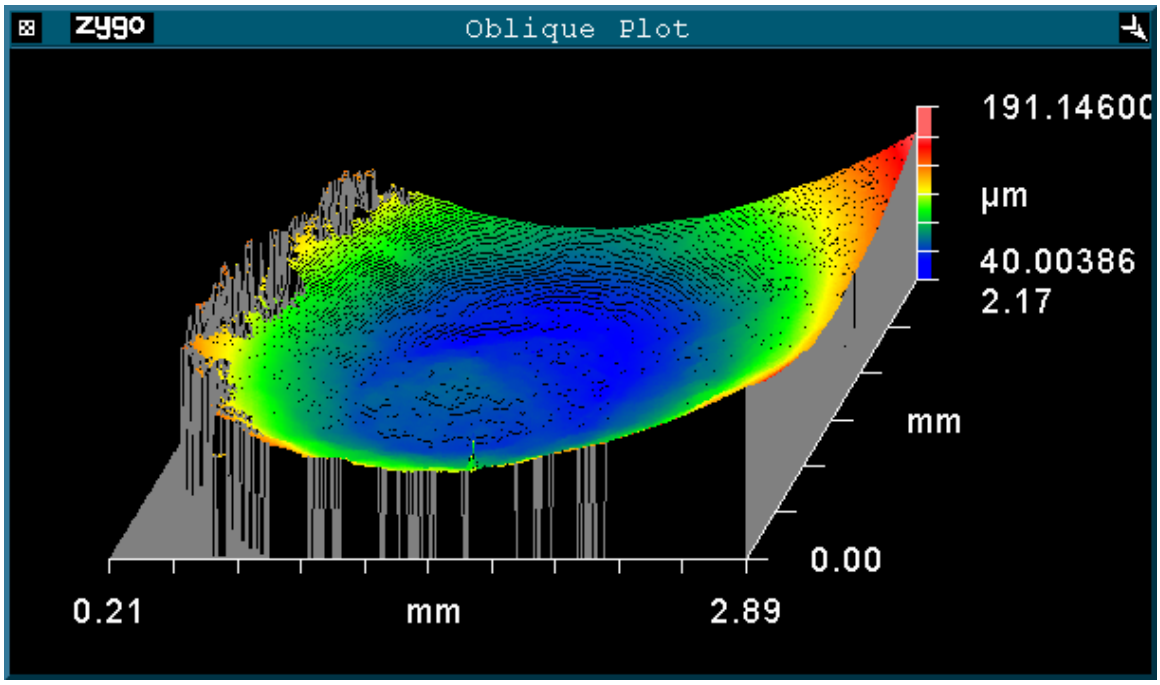

Figure 3-2. White light interferometry 3-dimensional profile of a wax impression of a straight-bore ablation crater

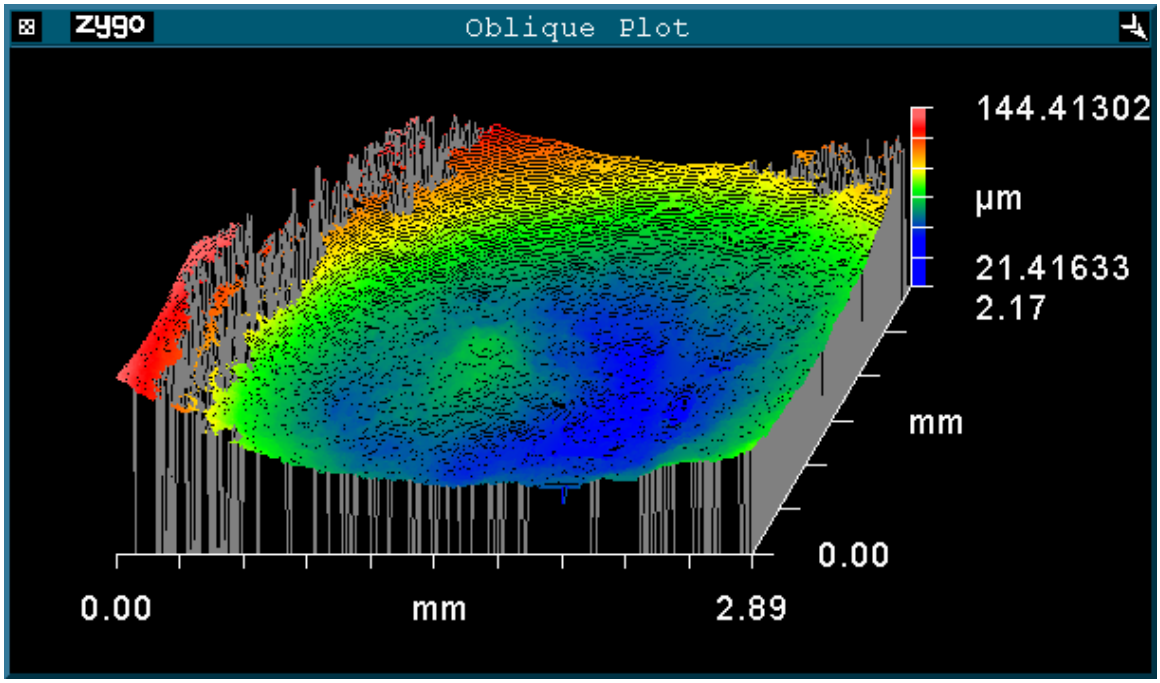

Figure 3-3. White light interferometry 3-dimensional profile of a wax impression of a scanning ablation crater

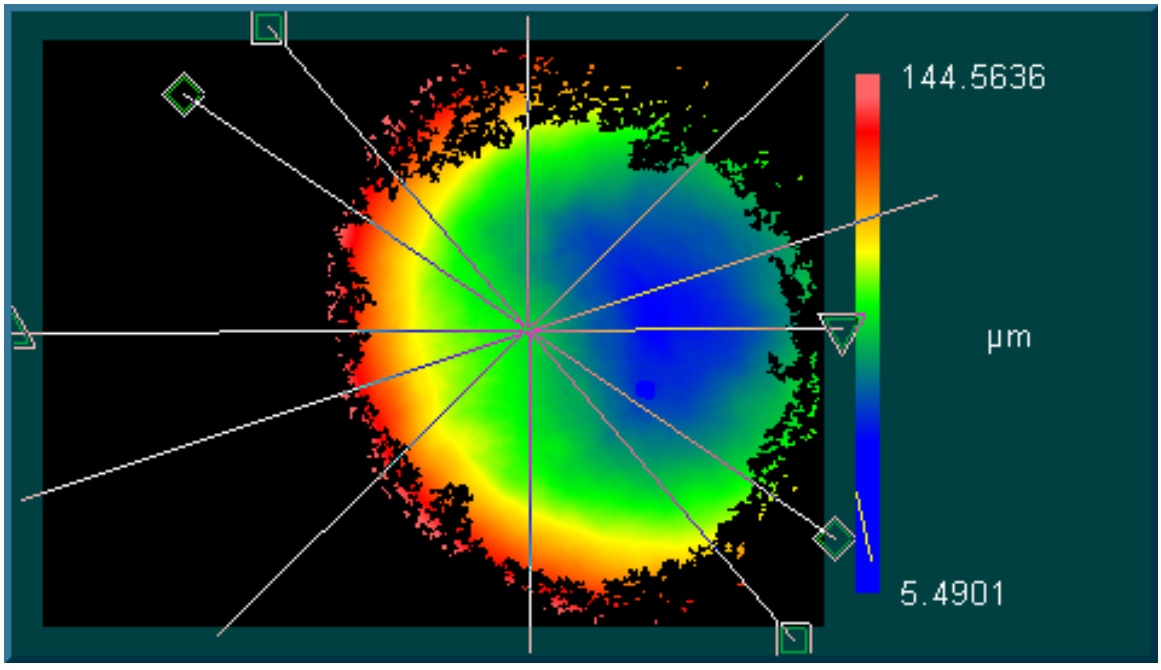

Figure 3-4. White light interferometry 2-dimensional profile of a wax impression of a straight-bore crater

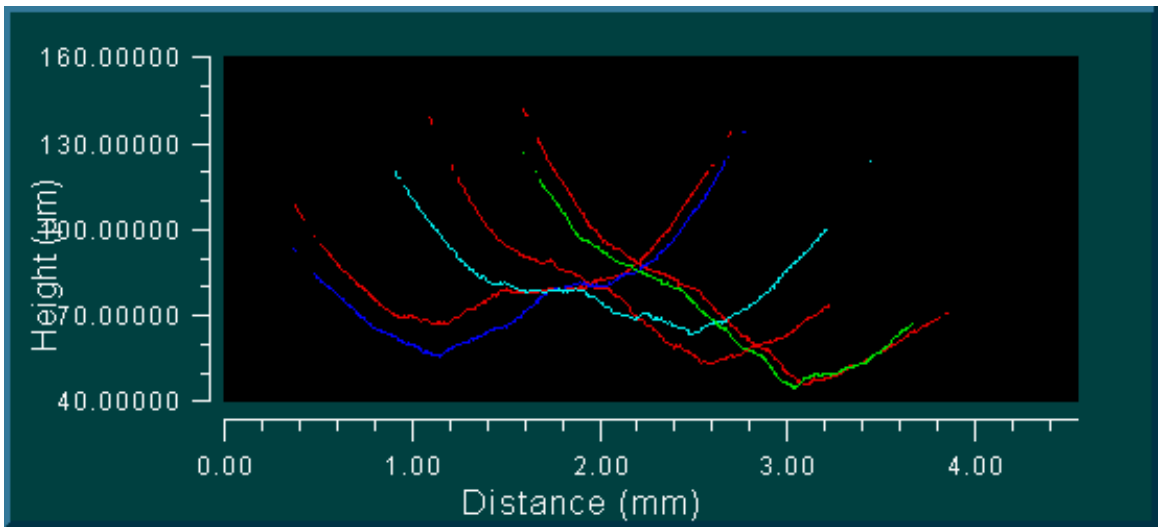

Figure 3-5. White light interferometry 2-dimensional cross sections of a wax impression of a scanning crater

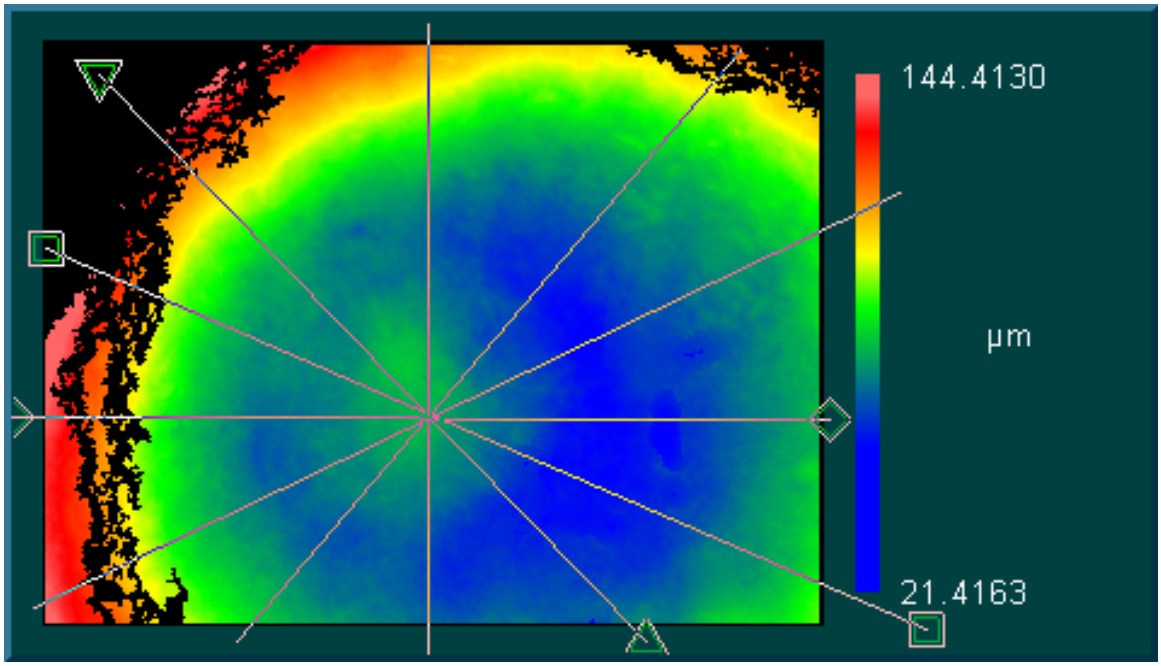

Figure 3-6. White light interferometry 2-dimensional profile of a wax impression of a scanning crater

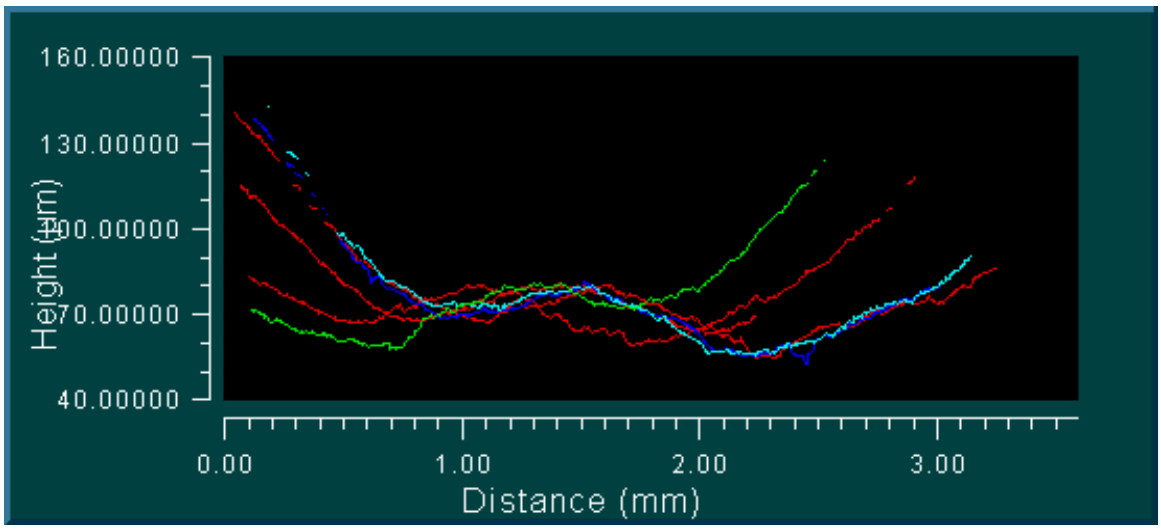

Figure 3-7. White light interferometry 2-dimensional cross sections of a wax impression of a scanning crater

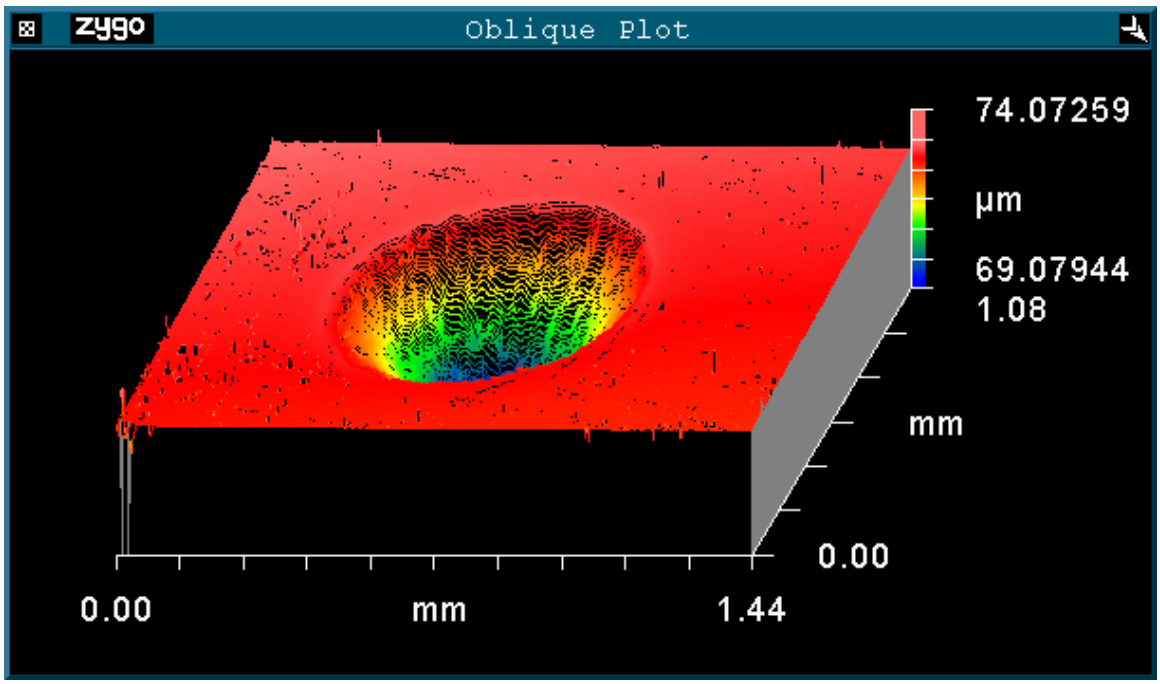

Figure 3-8. White light interferometry 3-dimensional profile of a straight-bore ablation crater on PMMA

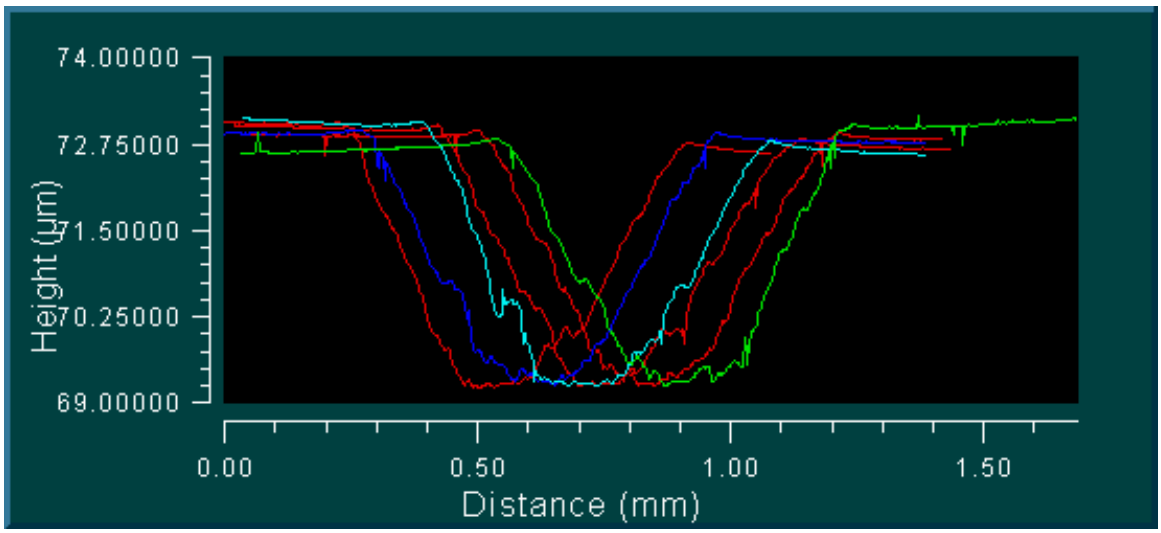

Figure 3-9. White light interferometry 2-dimensional cross sections of a straight-bore ablation crater on PMMA

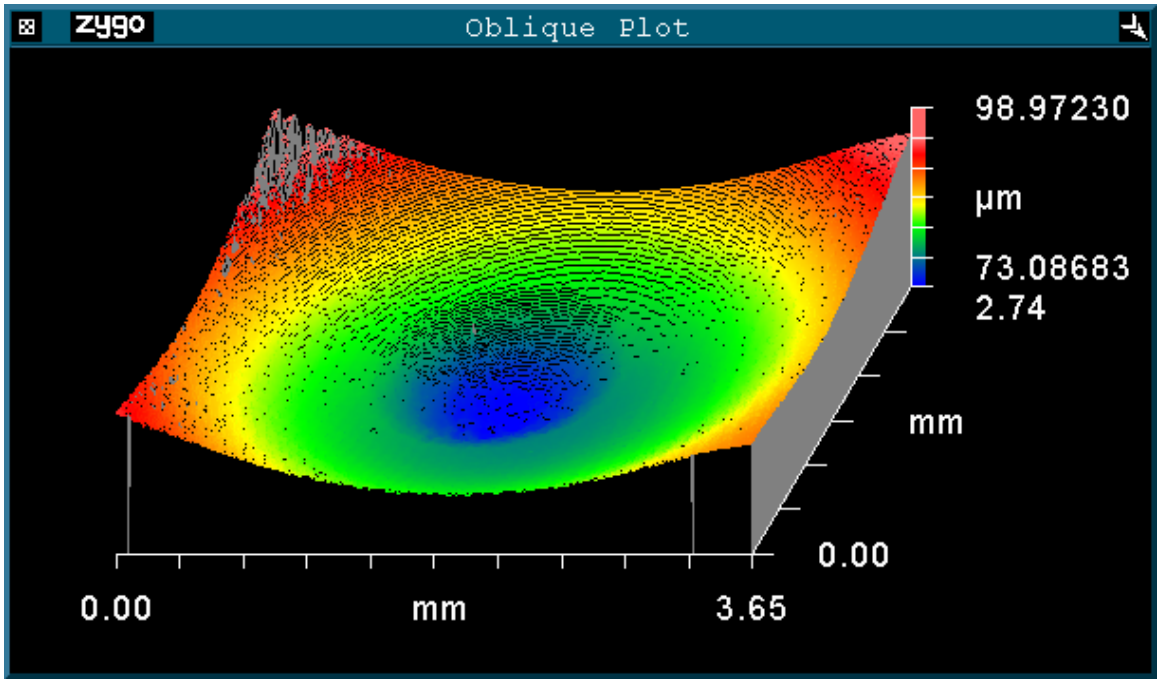

Figure 3-10. White light interferometry 3-dimensional profile of a scanning ablation crater on PMMA

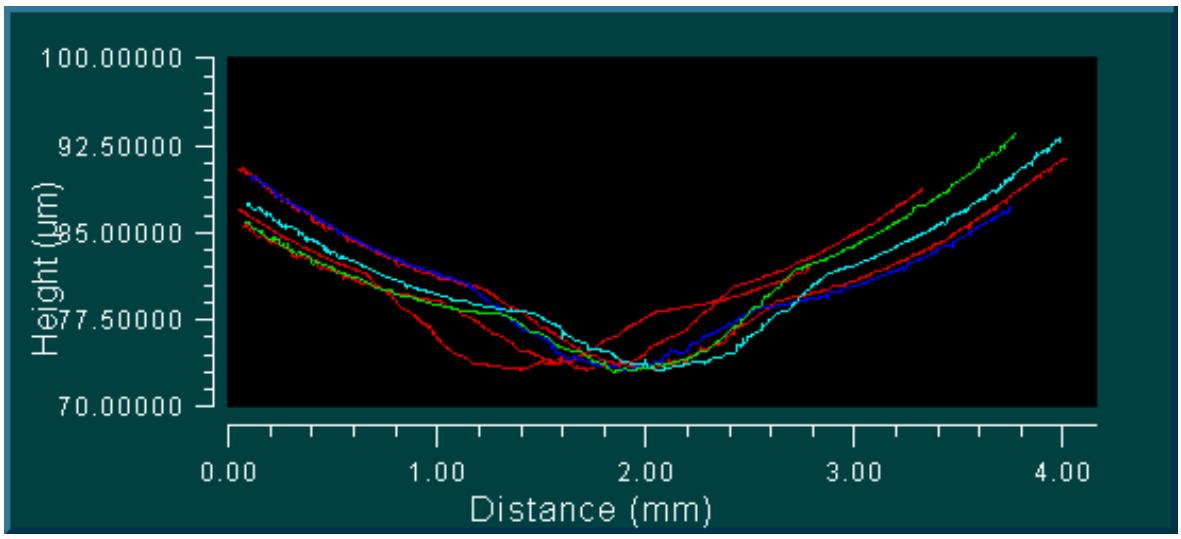

Figure 3-11. White light interferometry 2-dimensional cross sections of a scanning ablation crater on PMMA

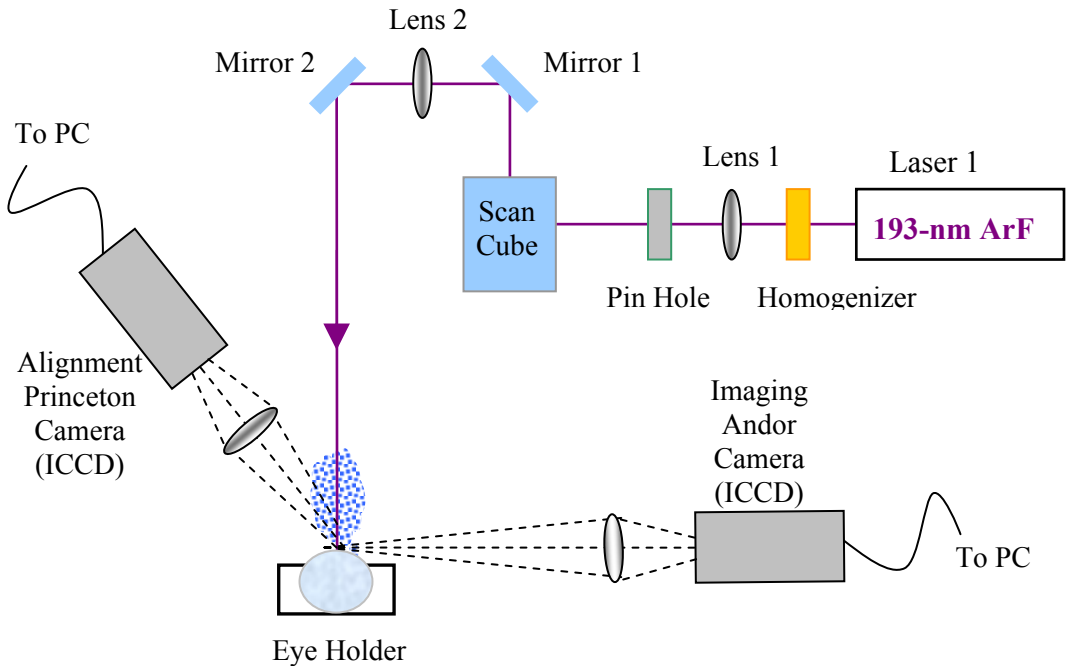

Figure 3-12. Experimental set-up for imaging ablation plume profiles

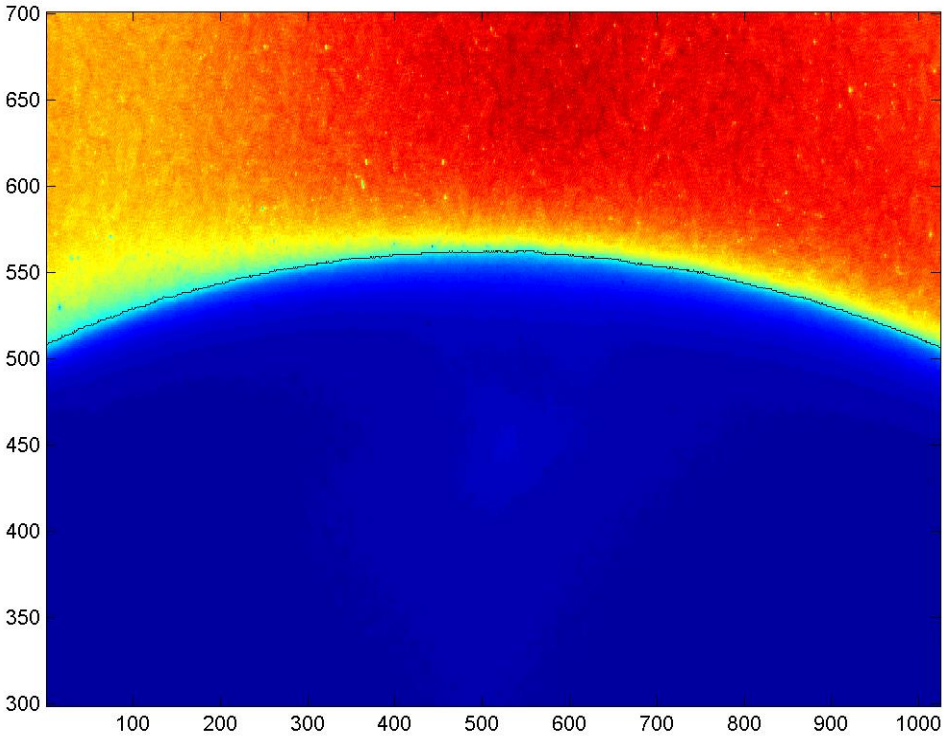

Figure 3-13. Representative profile image of a bovine eye showing the clear definition between the eye and the environment. Both axes are camera pixel numbers. An edge profile is also shown.

Table 3-1. Overall ablation depths (μm) for bovine straight-bore ablations for each interferogram for various laser repetition rates

1 Hz		**10 Hz**		**50 Hz**		**300 Hz**	
Average	Standard deviation	Average	Standard deviation	Average	Standard deviation	Average	Standard deviation
23.06	3.88	21.70	2.19	21.12	2.43	17.93	0.77
19.88	2.07	16.76	3.35	19.75	1.30	22.00	3.46
24.30	1.51	20.66	0.54	20.83	1.53	16.96	1.55
21.11	4.04						

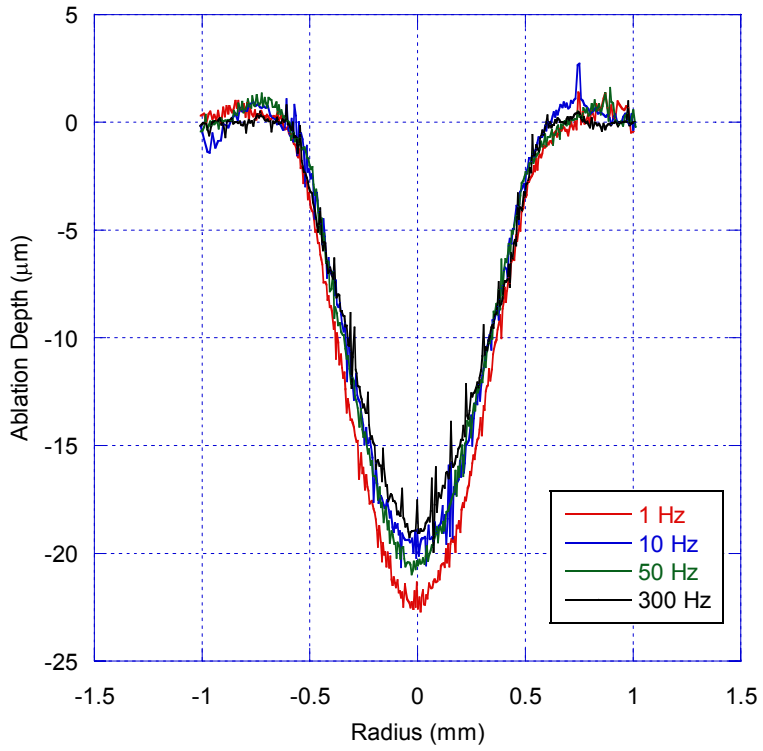

Figure 3-14. Straight-bore ablation crater profiles created on bovine corneas using 20 shots at various laser repetition rates

Table 3-2. Overall ablation depths (μm) for bovine straight-bore ablations for each laser repetition rates

Rate	Average	Standard deviation
1 Hz	22.18	3.33
10 Hz	19.50	3.07
50 Hz	20.44	1.81
300 Hz	18.91	3.07

Table 3-3. Overall ablation depths (μm) and standard deviations for bovine scanning ablations for each interferogram for various laser repetition rates

Without evacuator				**With evacuator**	
60 Hz		400 Hz		400 Hz	
Average	Standard deviation	Average	Standard deviation	Average	Standard deviation
22.49	1.74	24.79	4.23	23.85	1.17
20.95	1.58	20.95	0.99	24.48	2.34
26.08	2.44	26.78	1.13		
24.71	2.10	23.58	1.74		
23.76	0.77	19.47	2.03		

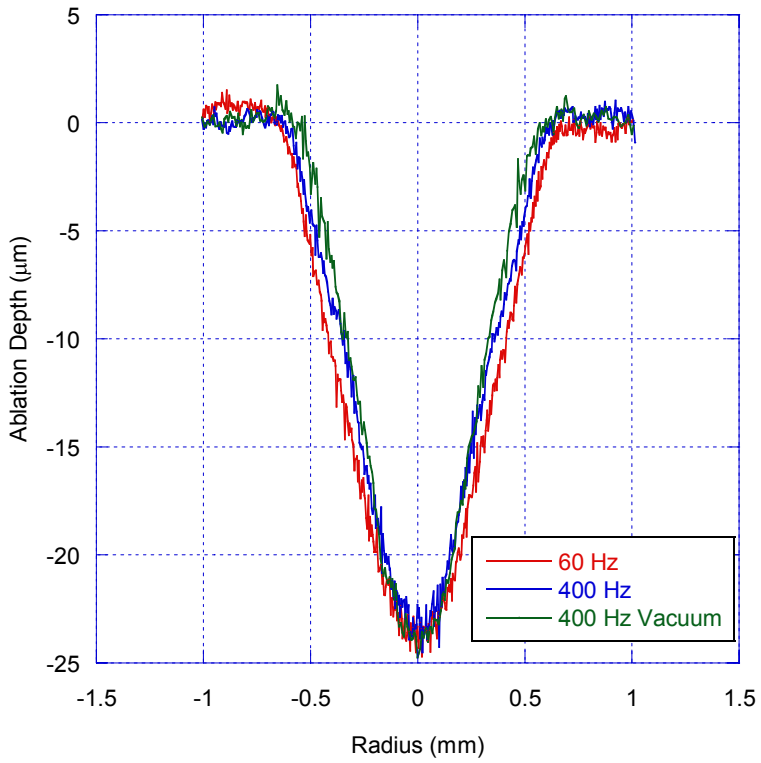

Figure 3-15. Scanning ablation crater profiles created on bovine corneas using 25 shots at various laser repetition rates

Table 3-4. Overall ablation depths (µm) for bovine scanning ablations for each laser repetition rates

Rate	Average	Standard deviation
60 Hz	23.64	2.47
400 Hz	23.16	3.37
400 Hz (with evacuator)	24.07	1.79

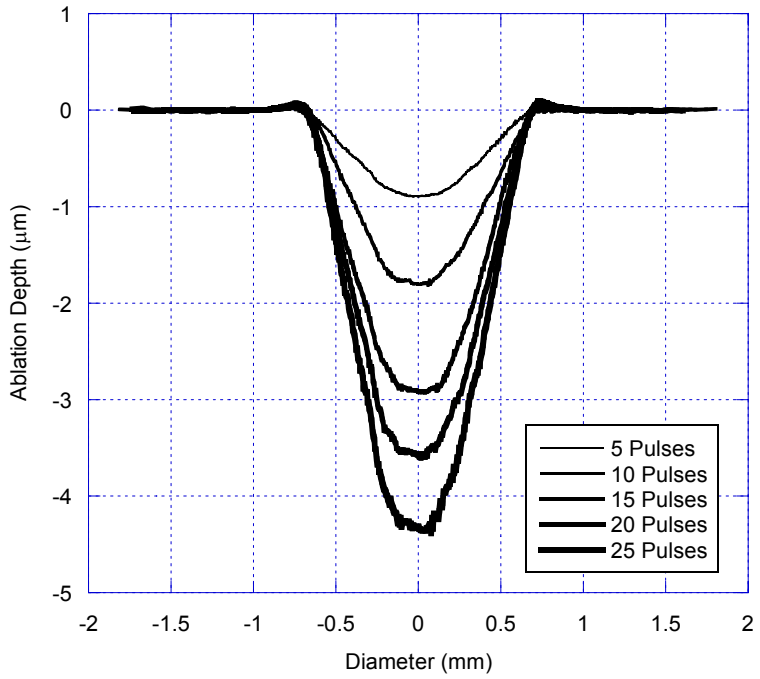

Figure 3-16. Ablation profiles in PMMA created at 1 Hz for various numbers of laser pulses

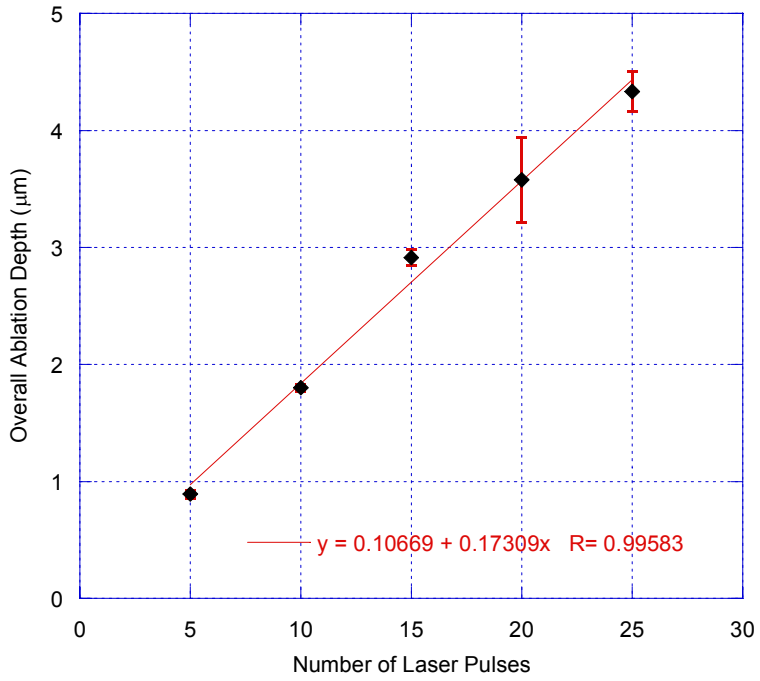

Figure 3-17. Ablation depths (μm) in PMMA created at 1 Hz for various numbers of laser pulses. The error bars represent one standard deviation.

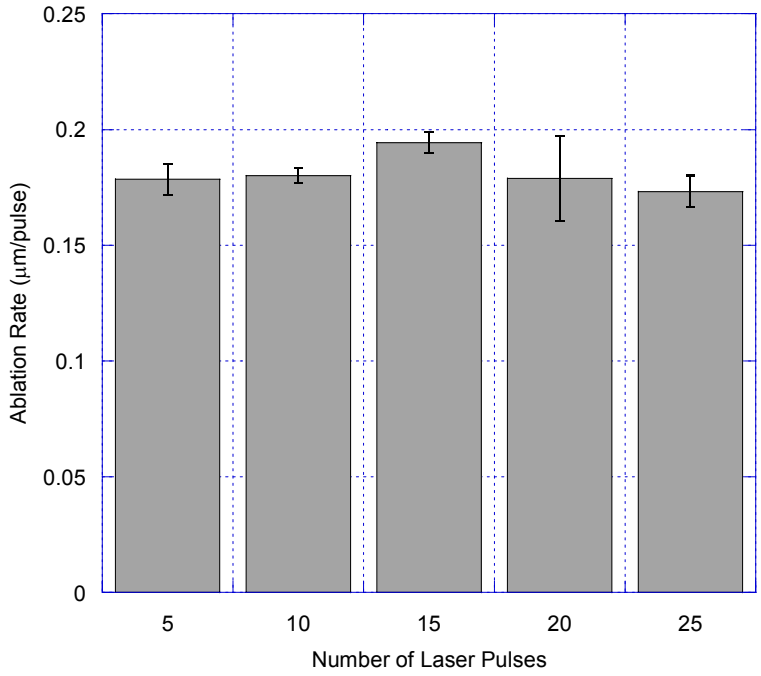

Figure 3-18. Average ablation rates (µm/shot) in PMMA created at 1 Hz for various numbers of laser pulses. The error bars represent one standard deviation.

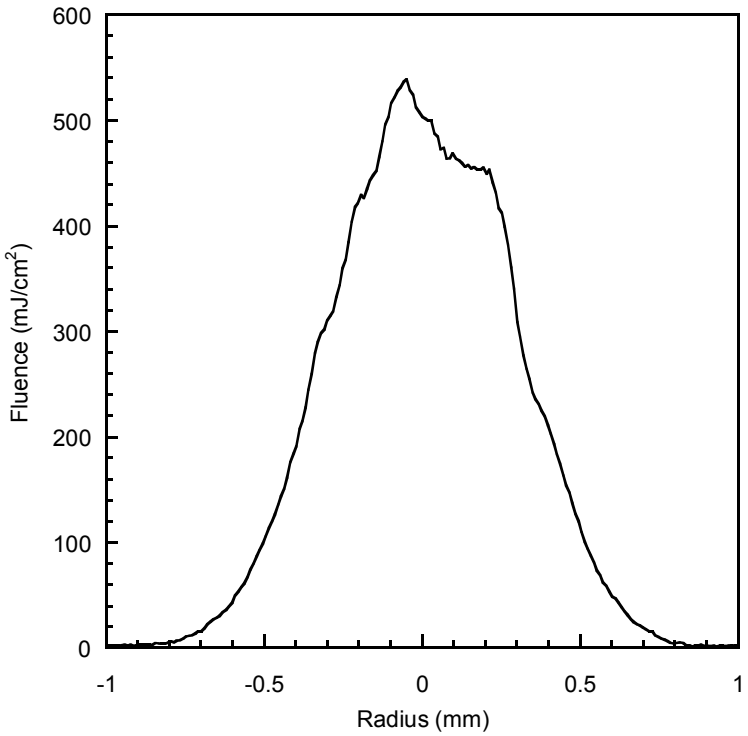

Figure 3-19. Fluence profile of the Alcon laser beam in mJ/cm^2

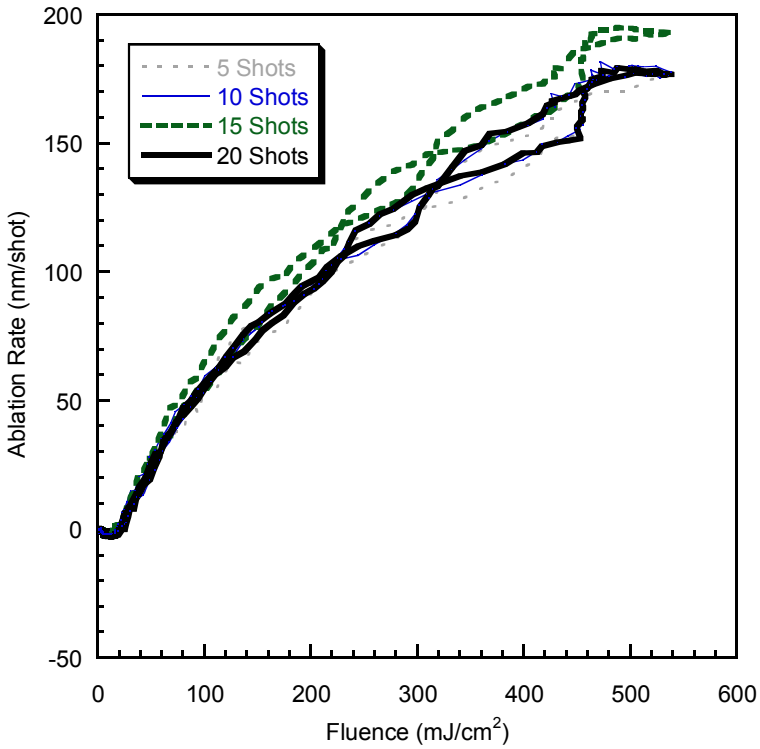

Figure 3-20. PMMA ablation rate (nm/shot) verses laser fluence (mJ/cm^2) for various numbers of laser pulses

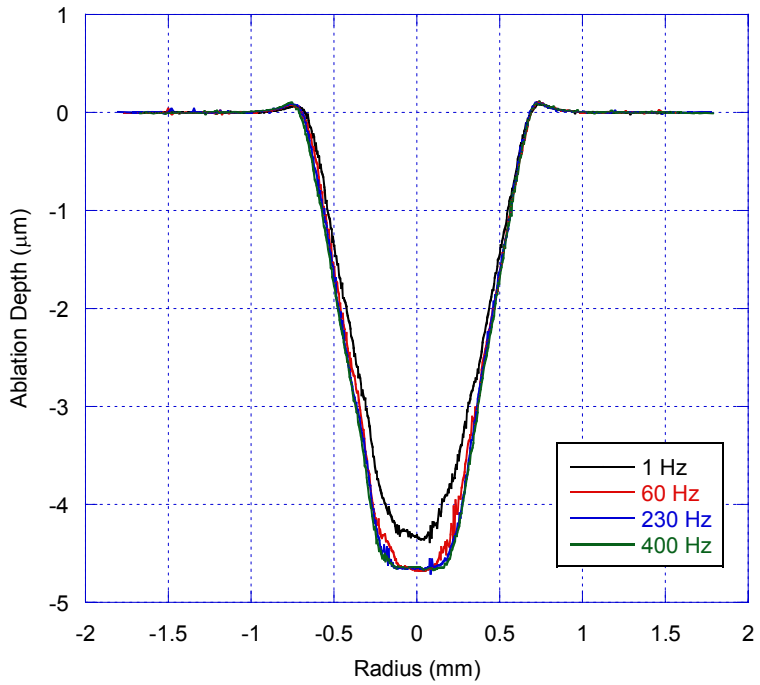

Figure 3-21. Ablation profiles in PMMA created with 25 laser pulses for various laser repetition rates

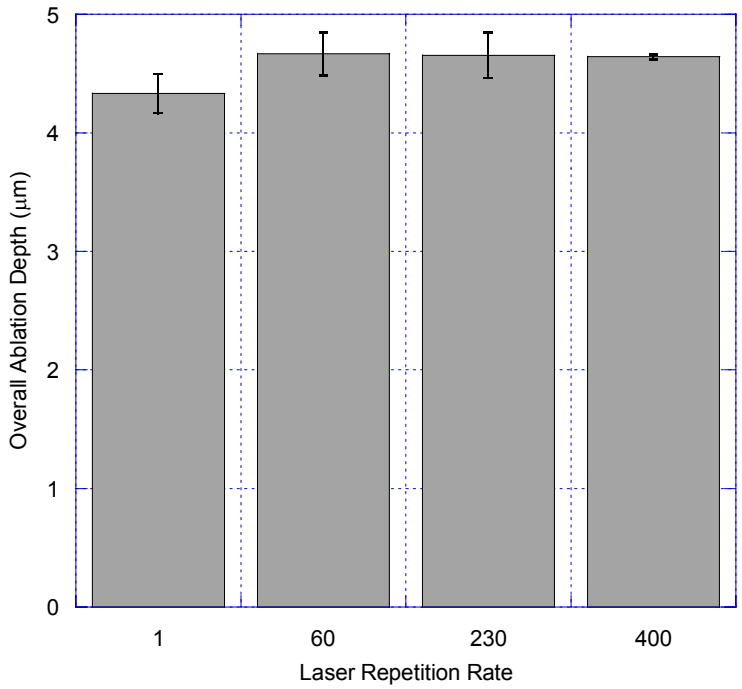

Figure 3-22. Ablation depths (μm) in PMMA created with 25 laser pulses for various laser repetition rates. The error bars represent one standard deviation.

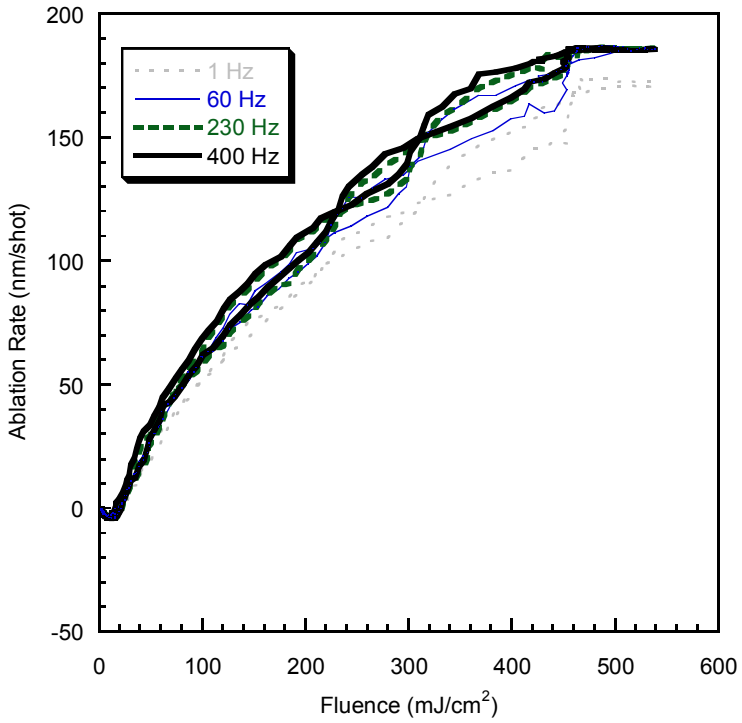

Figure 3-23. PMMA ablation rate (nm/shot) verses laser fluence (mJ/cm^2) for various laser repetition rates

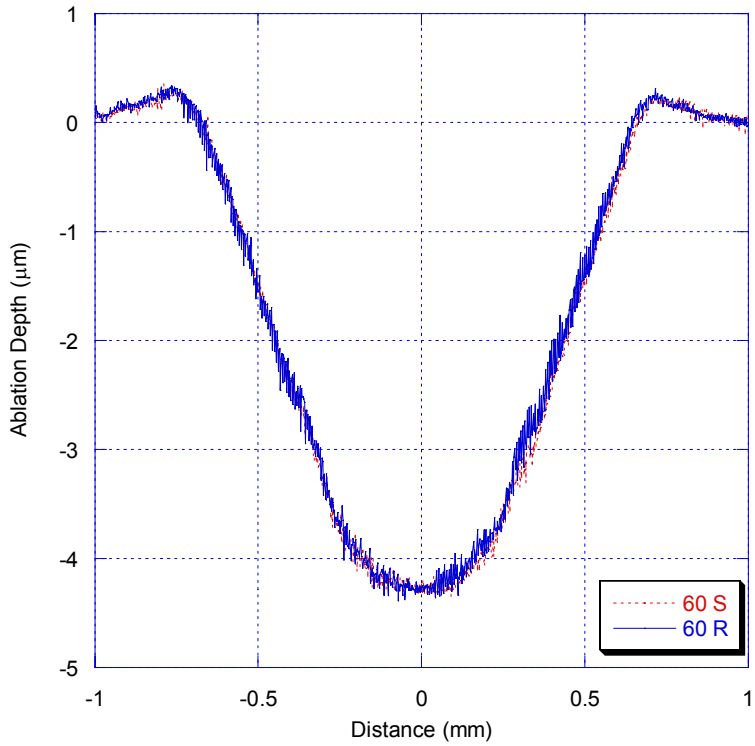

Figure 3-24. PMMA stretched spiral (S) and reversed spiral (R) ablation profiles at 60 Hz

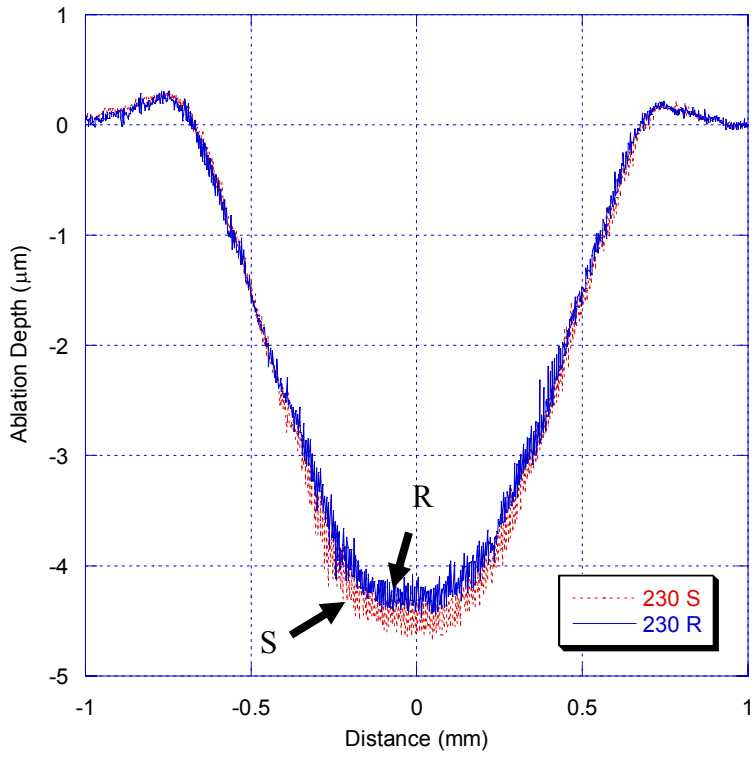

Figure 3-25. PMMA stretched spiral (S) and reversed spiral (R) ablation profiles at 230 Hz

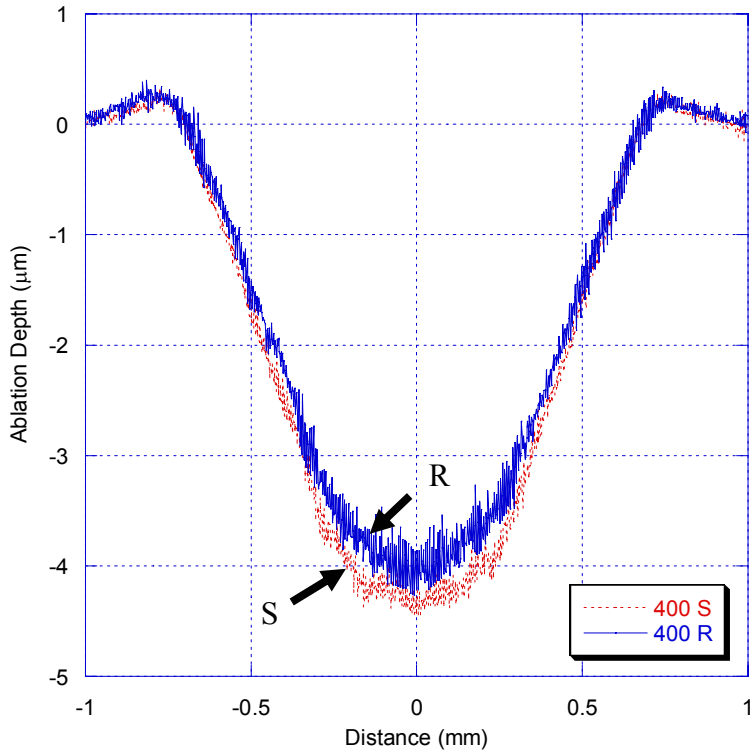

Figure 3-26. PMMA stretched spiral (S) and reversed spiral (R) ablation profiles at 400 Hz

Table 3-5. PMMA ablation depths (µm) and standard deviations (µm) for the stretched spiral and reverse spiral algorithms and ablation rates of 60, 92 and 400 Hz

Ablation	Rate	Pattern	Average	Standard deviation
A1	60	Stretched	4.25	0.19
A2	60	Reverse	4.28	0.20
A3	60	Stretched	4.30	0.09
A4	60	Reverse	4.28	0.21
A5	60	Stretched	4.25	0.18
A6	60	Reverse	4.28	0.15
A7	92	Stretched	4.60	0.09
A8	92	Reverse	4.38	0.11
A9	92	Stretched	4.38	0.12
A10	92	Reverse	4.16	0.20
A11	92	Stretched	4.32	0.07
A12	92	Reverse	4.31	0.17
A13	400	Stretched	4.42	0.15
A14	400	Reverse	4.22	0.19
A15	400	Stretched	4.31	0.18
A16	400	Reverse	3.97	0.20
A17	400	Stretched	4.28	0.23
A18	400	Reverse	3.85	0.25

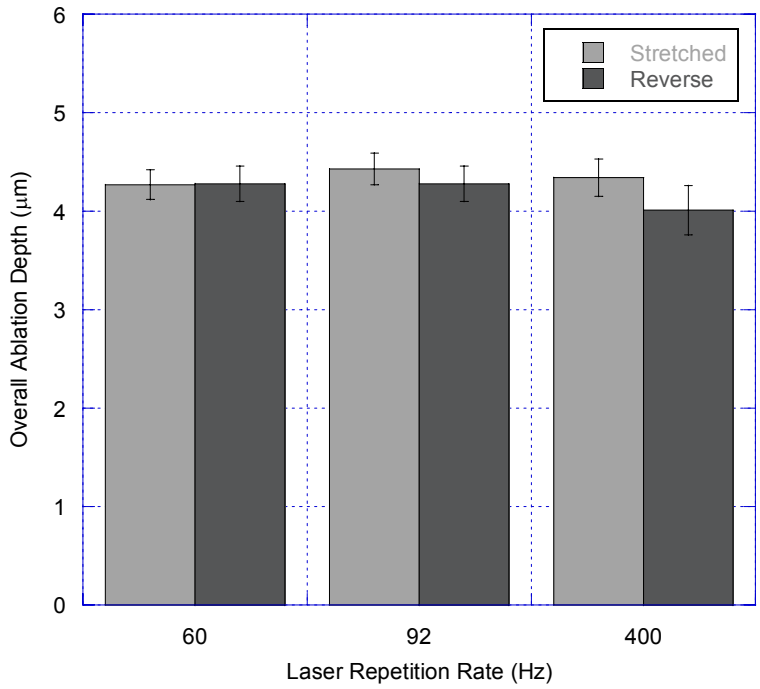

Figure 3-27. PMMA ablation depths (µm) for the stretched spiral and reverse spiral algorithms at each ablation rate. Error bars represent one standard deviation.

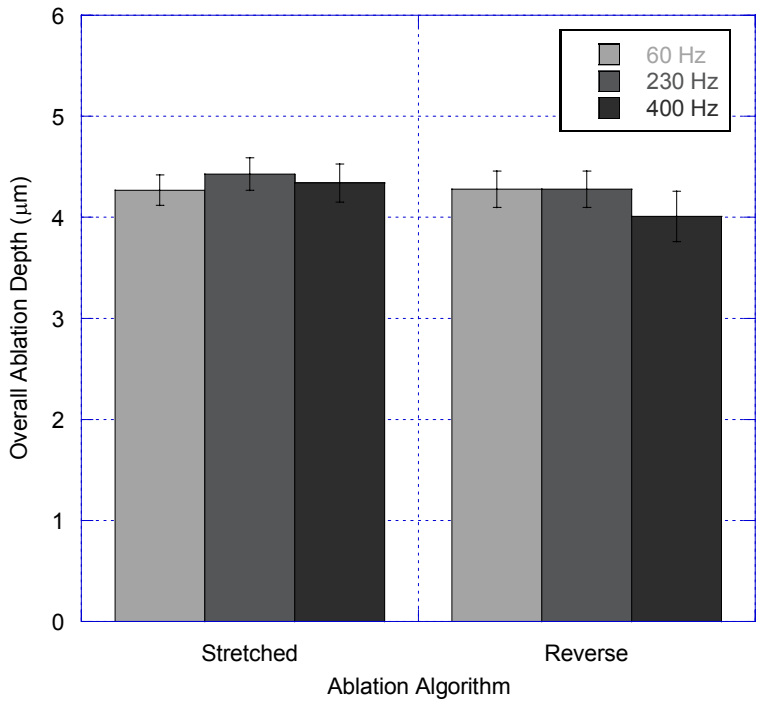

Figure 3-28. PMMA ablation depths (µm) for 60, 230 and 400 Hz for each algorithm. Error bars represent one standard deviation.

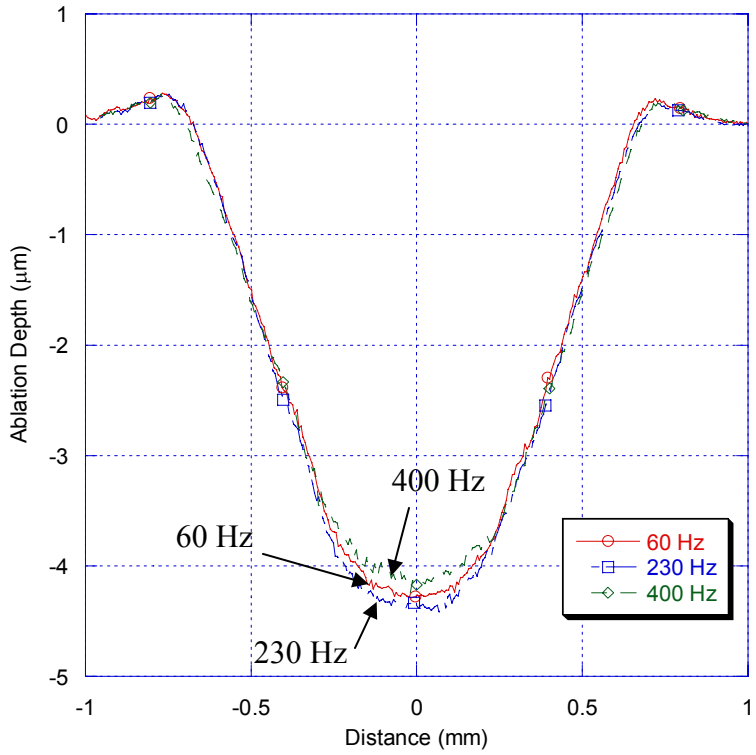

Figure 3-29. PMMA combined ablation profiles for 60, 230 and 400 Hz

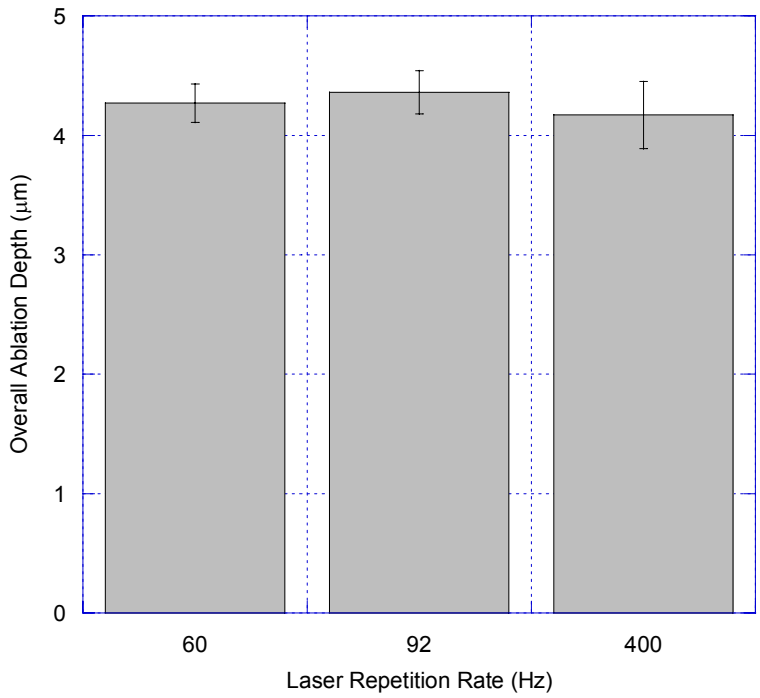

Figure 3-30. PMMA combined overall ablation depths (μm) for 60, 230 and 400 Hz. Error bars represent one standard deviation.

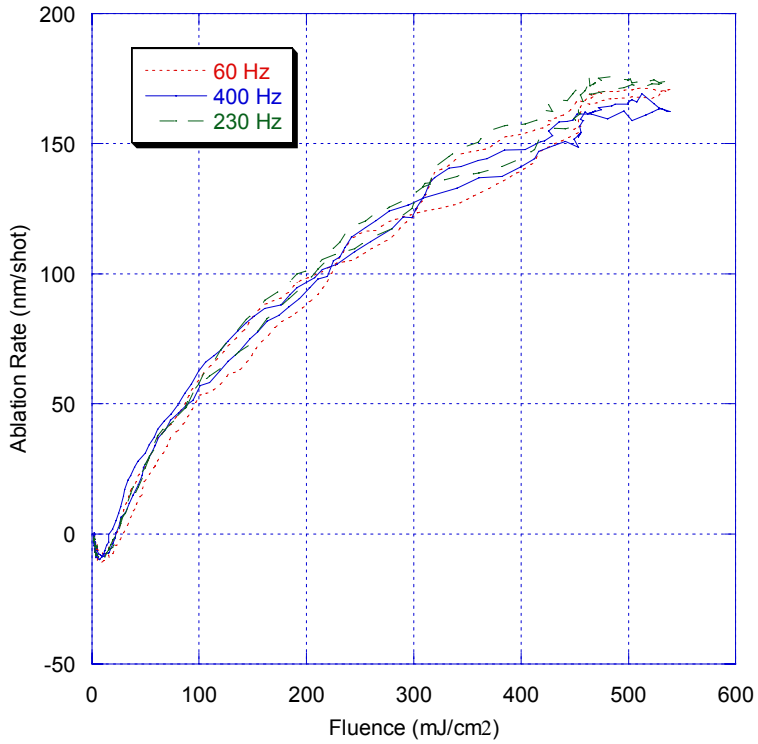

Figure 3-31. PMMA ablation rate (nm/shot) verses laser fluence (mJ/cm^2) for various laser repetition rates

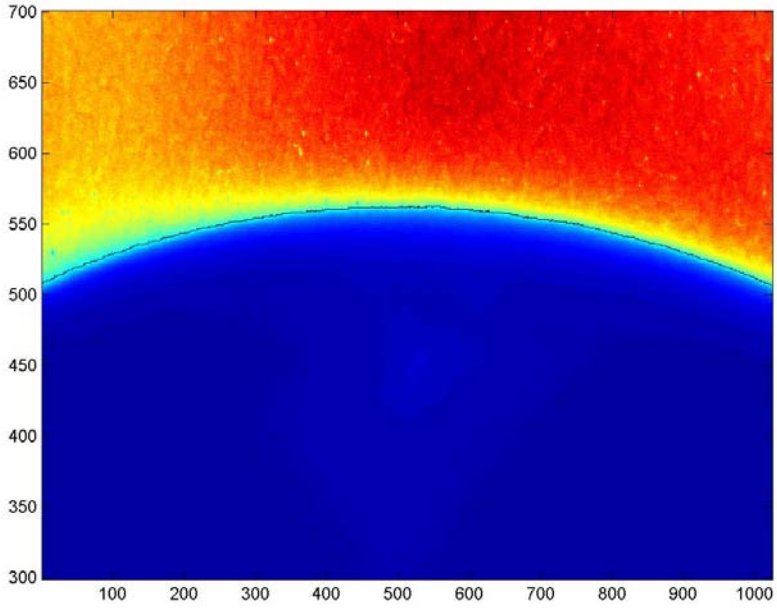

Figure 3-32. Representative pre-ablation profile image of a bovine eye. Both axes are camera pixel numbers. The edge profile is also shown.

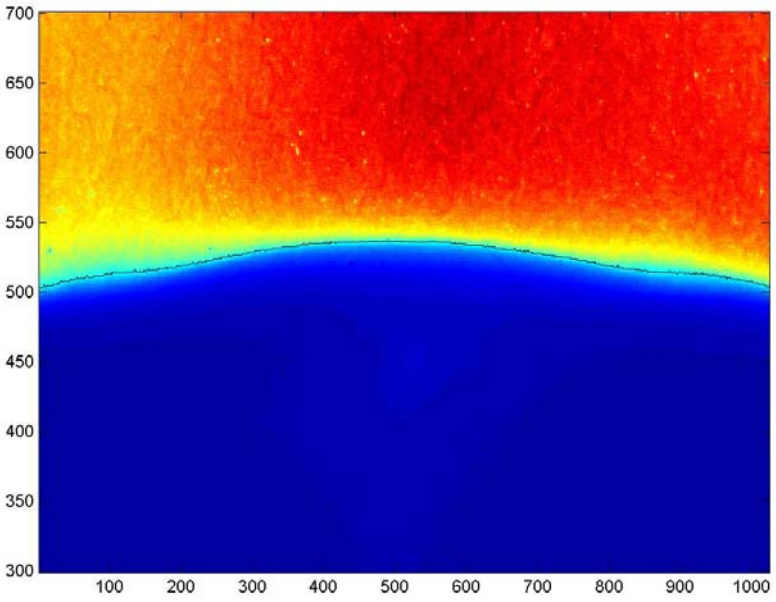

Figure 3-33. Representative post-ablation profile image of a bovine eye. Both axes are camera pixel numbers. The edge profile is also shown.

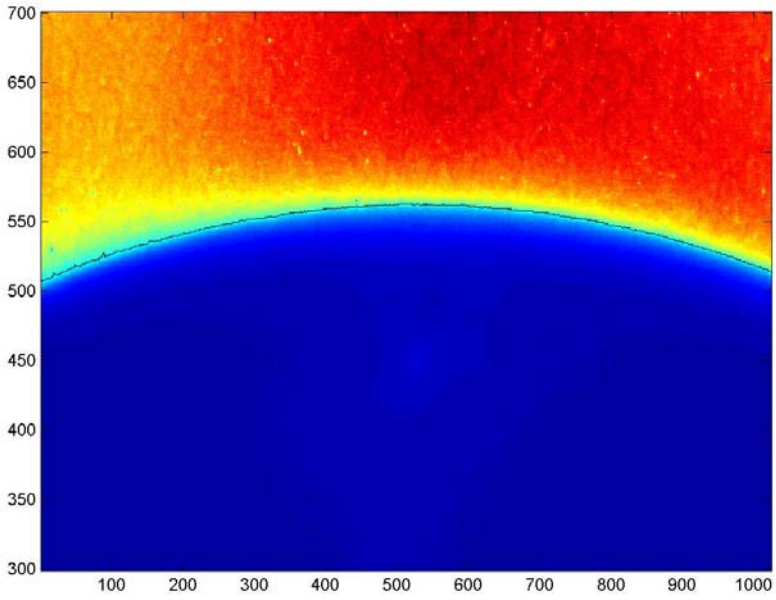

Figure 3-34. Representative pre-ablation profile image of a bovine eye. Both axes are camera pixel numbers. The edge profile is also shown.

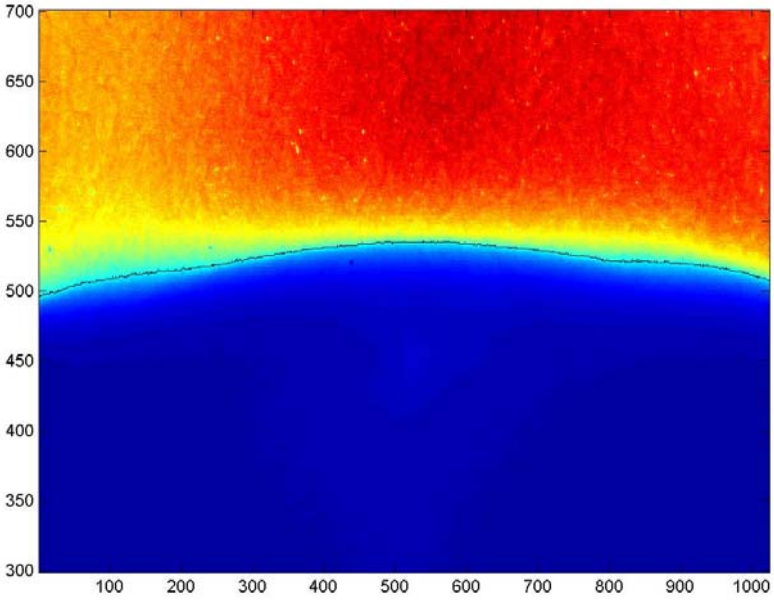

Figure 3-35. Representative post-ablation profile image of a bovine eye. Both axes are camera pixel numbers. The edge profile is also shown.

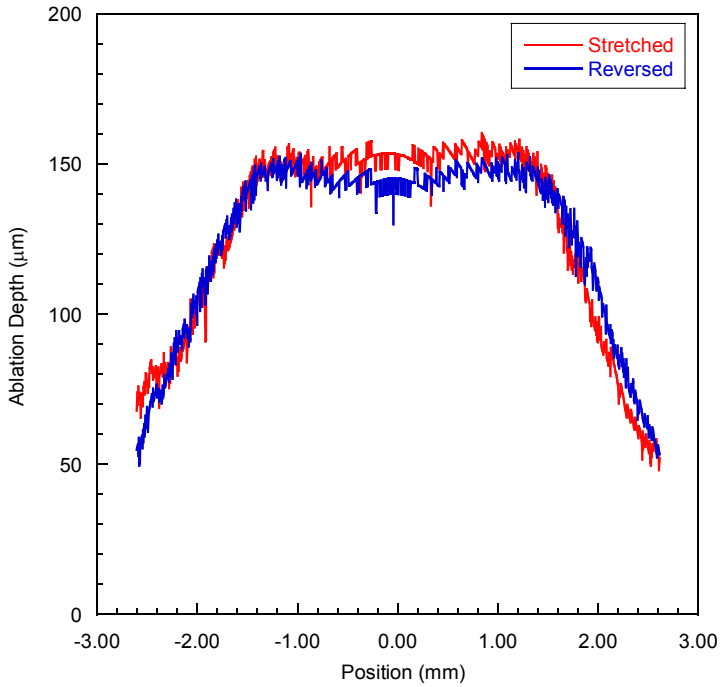

Figure 3-36. Representative stretched spiral and reverse spiral ablation profiles for a paired set of eyes

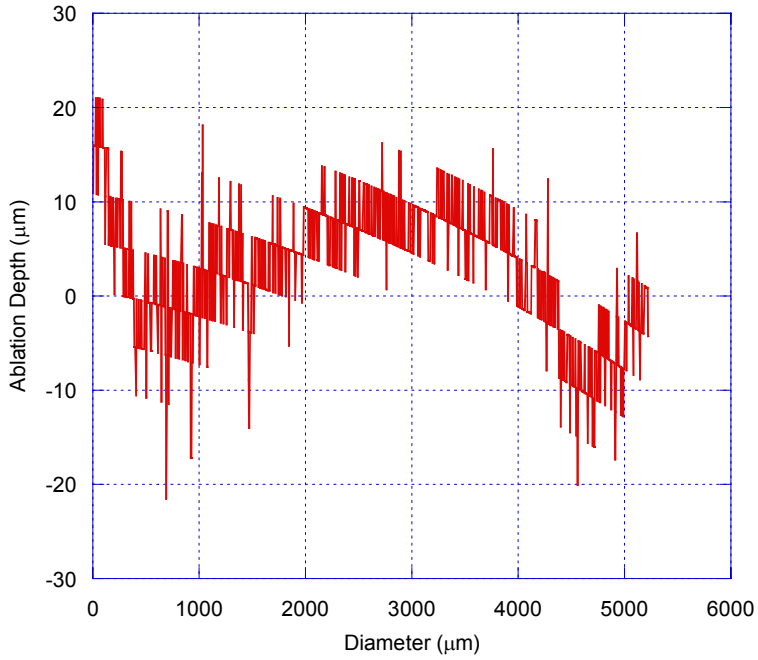

Figure 3-37. Representative differential ablation profile (stretched spiral minus reverse spiral) of a bovine eye. This differential profile is generated from the eyes in Figures 3-33 through 3-35.

Table 3-6. Maximum ablation depth for paired stretched and reverse spiral ablation

Stretched **spiral**	Reverse **spiral**
222.08	150.39
182.29	157.83
120.21	169.43
186.81	139.85
150.61	199.01
143.04	145.22
147.87	153.67
160.48	192.98
195.42	249.49

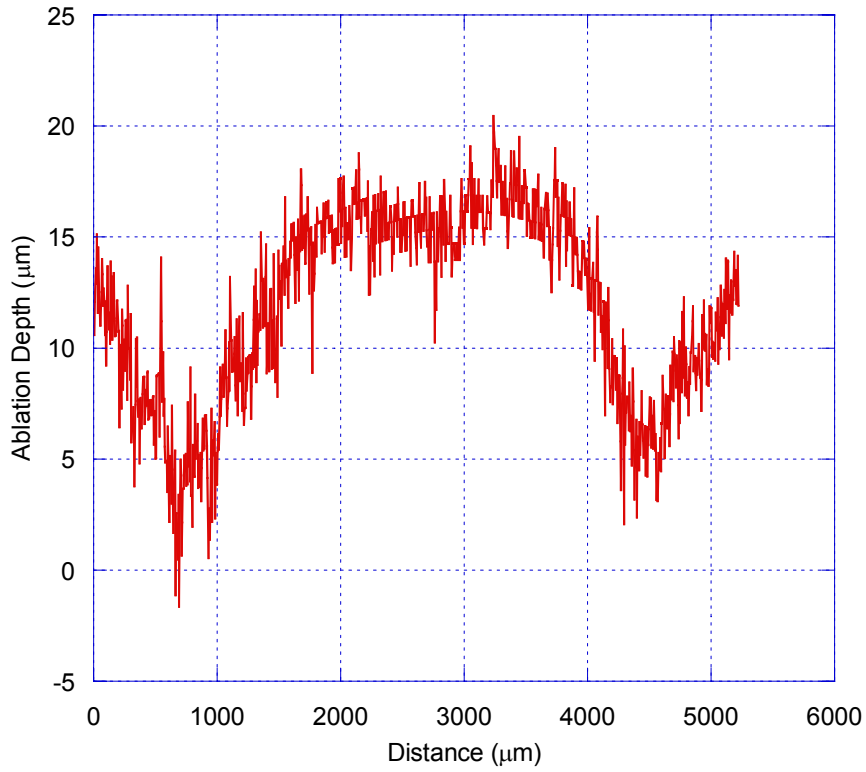

Figure 3-38. Average differential ablation profile (stretched spiral minus reverse spiral) image of a bovine eye created at a laser repetition rate of 92 Hz

CHAPTER 4
HISTOLOGY

The previous chapters have focused on the efficacy of the tissue removal. They sought to verify that changing the laser repetition rate of the surgical laser in corrective refractive surgery does not physically alter the ablation process. It must still be checked that the underlying tissue has no additional adverse damage as compared to current clinical rates. As there is less time between laser pulses for thermal energy to disperse, there is potential for an increase in tissue damage. Since the wound healing process is complex, and much research has been devoted to the topic, it is essential that increasing the laser repetition rate does not induce additional injury.

Experimental Setup and Methods

To assess any histological changes to the underlying stroma caused by varying the laser repetition rate, corneal ablations were performed over a 6-mm zone with a standard 9-diopter correction, using the experimental set-up of Figure 2-1. This is the maximum correction typically applied for this surgical system, thus any additional harm to the underlying tissue would be maximized by using this algorithm. Ablations were performed using laser repetition rates of 60, 230 and 400 Hz. For these experiments, no additional laser shots were added in the center as was done in the ablation profile study described above.

For assessment of rate effects, conventional microscopy, scanning electron microscopy (SEM), and transmission electron microscopy (TEM) were performed on corneal buttons (four at each rate), which were immediately harvested using 8-mm biopsy punches. For conventional microscopy, the buttons were dehydrated in a graded series of alcohol solutions. They were then cleared with xylene solution and fixed into a paraffin block. Corneal samples of 4-μm thickness were sectioned and stained with H&E (hematoxylin and eosin). Light microscopy images were processed and stored for each sample. For TEM and SEM analysis, corneal buttons (four for

each rate) were harvested and fixed in 2.5% glutarlaldehyde in 0.1 M cacodylate buffer and prepared for analysis. The cornea buttons were bisected and postfixed in 2% osmium tetroxide for two hours. Small pieces of the cornea were embedded in low-viscosity epoxy medium, thin sectioned, stained with uranyl acetate and lead citrate, and viewed with a JEOL 100 CX transmission electron microscope. The other half of the cornea was prepared for SEM by critical point drying. The tissue was glued to stubs, sputter coated with gold palladium, and viewed with a JEOL 25 CF scanning electron microscope. SEM and TEM images were then processed and stored for each sample. These sections were prepared and microscopy was performed by Dr. Henry Edelhauser's team at Emory University. SEM and TEM samples were analyzed at two separate locations, the ablation crater side and the ablation crater floor, as shown in Figure 4-1.

Histology Results

Conventional microscopy was performed first. Four eyes were ablated each with 60 Hz and 400 Hz. For each laser repetition rate, one eye was given a 3-diopter correction, one eye was given a 6-diopter correction, and two eyes were given a 9-diopter correction. Figure 4-2 shows representative high magnification optical microscopy images of the ablated corneas. The section on the right is from a cornea ablated at 60 Hz, while the section on the right is from a cornea ablated at 400 Hz. The arrows on the image point to the surface that was ablated.

Visible in the bottom of these images is Descemet's membrane and the endothelial layer. Descemet's membrane separates the stroma, which composes the majority of the section, from the dark thick endothethial layer. Note that the epithelial layer and Bowman's membrane are not present. The epithelial layer was mechanically removed prior to ablation, and Bowman's layer was removed by the ablation. Qualitatively, no differences were observed between the samples generated at 60 Hz and those generated at 400 Hz.

For further evaluation of potential differential damage, SEM and TEM images were analyzed. Four eyes were ablated each at 60 Hz and 400 Hz with 9-diopter corrections, the maximum correction clinically applied by the Alcon laser system. To provide higher magnification, SEM images of the extracted corneas ablated at 60 and 400 Hz were generated and are shown in Figure 4-3 at various magnifications. When comparing similar conditions for the image pairs, both ablation conditions (60- and 400-Hz laser repetition rate) appear to present similar features, suggesting that no differential response exists between the two ablation conditions.

In order to quantitatively assess any ablation rate effects, TEM analysis was performed to directly image the collagen fibrils. TEM images of corneas ablated at 60 and 400 Hz are shown in Figure 4-4 at the same magnification for direct comparison. Just as with the SEM images, no additional tissue damage is visually noticeable, including no visually observable condensing or distortion of collagen fibrils. The TEM analysis revealed no differential damage between the two ablation rates based on the observed structures.

In order to quantify information that may be represented in the TEM images, the configuration of collagen fibrils at the ablation surface was examined more closely. The TEM images (three eyes for each rate) were broken into squares normal to the ablated crater surface, and the number of collagen fibrils (i.e. dots) in each square was counted. The counts (corrected for varying magnifications) were then compared. At 60 Hz, an average of 221 fibrils/μm^2 (σ = 36 fibrils/μm^2) were observed adjacent to the ablation surface. At 400 Hz, an average of 263 fibrils/μm^2 (σ = 22 fibrils/μm^2) were observed. For a 95% confidence value (t-test), there is no statistical difference in collagen fibril density near the ablation surface between 60 and 400 Hz ablation rates.

Histology Summary

Based on conventional microscopy, no differences were observed between the samples generated at 60 Hz and those generated at 400 Hz. In the SEM samples, when comparing comparable conditions for the image pairs, both ablation conditions (60- and 400-Hz laser repetition rate) appear to present similar features, suggesting that no differential response exists between the two ablation conditions. In the TEM images, just as with the SEM images, no additional tissue damage is visually noticeable, including no visually observable condensing or distortion of collagen fibrils. The TEM analysis revealed no differential damage between the two ablation rates based on the observed structures. For a 95% confidence value (t-test), there is no statistical difference in collagen fibril density near the ablation surface between 60 and 400 Hz ablation rates. Overall, the collagen fibrils do not show any signs of disorganization, size changes or coagulation. Based on the microscopy analysis, it is concluded that no thermal damage or differential thermal damage (i.e. 60 vs. 400 Hz) is observed under these ablation conditions.

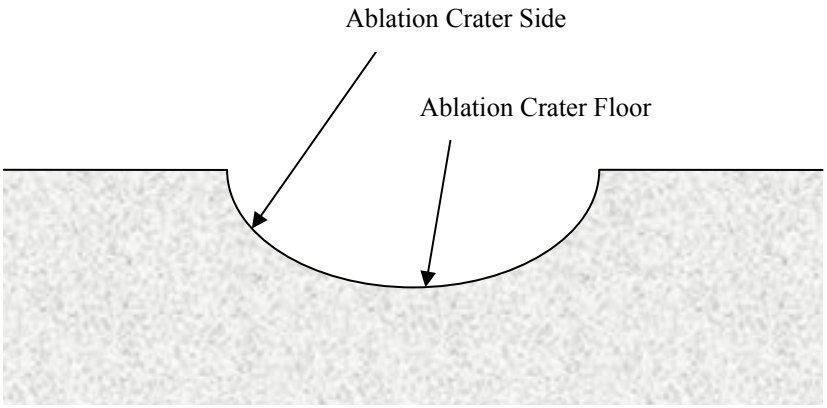

Figure 4-1. Location guide for SEM and TEM microscopy samples

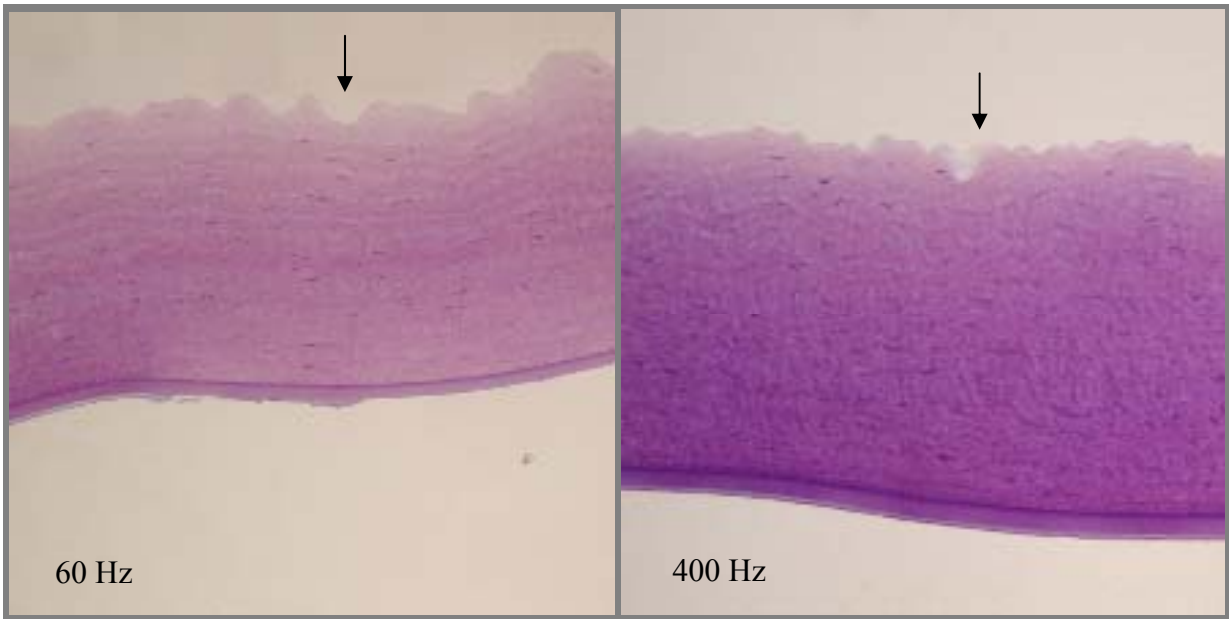

Figure 4-2. High magnification H&E-stained microscopy images of the ablation crater for laser ablations created at 60 Hz and 400 Hz.

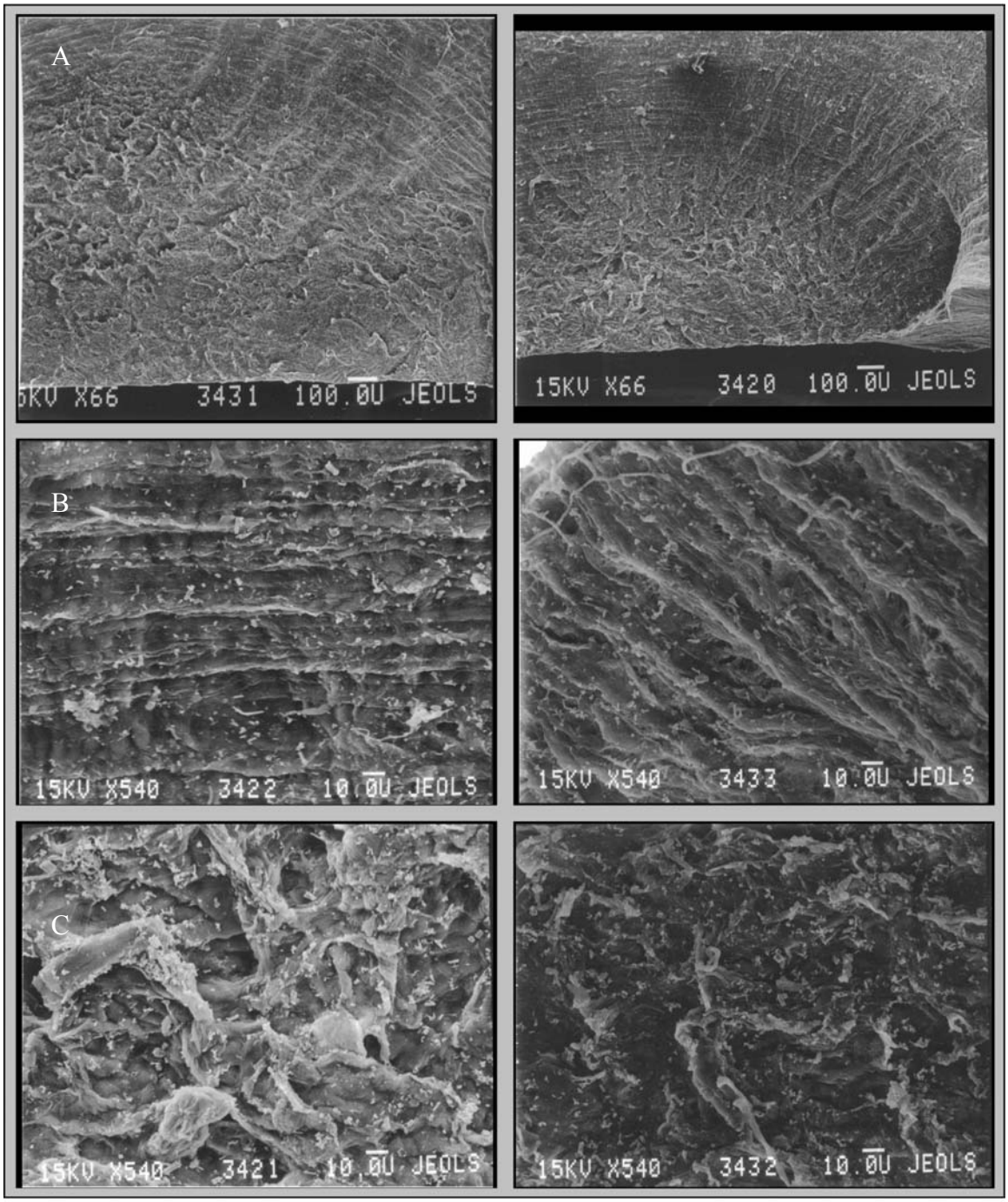

Figure 4-3. SEM images of ablation craters created at 60 Hz and 400 Hz. A) Overall ablation crater. B) Ablation crater sides. C) Ablation crater floor.

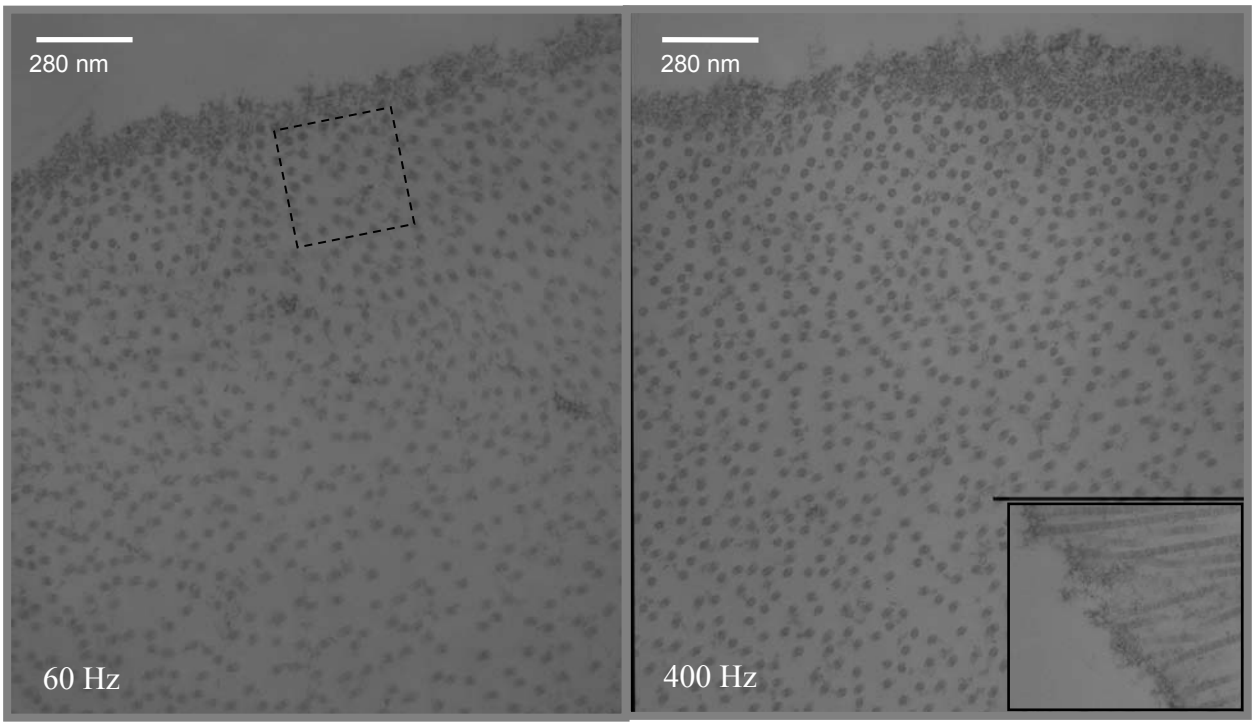

Figure 4-4. TEM images of bovine cornea cross-sections following laser ablation at 60 Hz and 400 Hz. The upper surface is the ablation surface, and the individual collagen fibrils are visible. The scale bar is 280 nm.

CHAPTER 5
SUB-ABLATIVE PERTUBATIONS

The work presented in this research proposal thus far has been of a more practical nature. However, the fundamental mechanism of tissue removal in corneal refractive surgery remains unresolved. The research presented here seeks to better understand the underlying process of corneal photoablation. Current theories suggest that below the ablation threshold, the energy deposition by the excimer laser into the corneal tissue results in a solely photothermal reaction, and that photochemical reactions only begin to occur once the threshold has been breached [5]. This experiment will examine laser-induced changes in collagen and amino acid solutions at sub-ablative conditions.

Experimental Setup and Methods

Transmission experiments were implemented to study the reaction of collagen and amino acid solutions to sub-ablative laser fluences. A sub-ablative laser beam is used to perturb the solution sample, and a lower energy probe beam is used to determine the transmission through the sample.

The change in transmission can be recorded for each pulse of the perturbing laser and analyzed to determine changes in the sample due to the sub-ablative perturbing laser pulse. In order to investigate the role of photochemical effects at low fluences, two sample types were analyzed. The first is a solution of calf-skin Type II collagen dissolved in acetic acid. The second is a solution of the three constituent amino acids (glycine, proline and hydroxyproline) in acetic acid. The latter solution is an approximation of the collagen solution without the peptide bond, noting that the peptide bond is believed to be the primary chromophore of corneal collagen in laser photorefractive surgery [5, 14]. If energies less than the threshold value result in solely photothermal reactions within the tissue, the results obtained from the two solutions should be

comparable. If the response of the two solution types gives different results, then one may conclude that the peptide bond plays a definite role in the sub-ablative reaction of corneal collagen to excimer laser pulses, pointing to a distinctive photochemical role.

These experiments were performed using alternately a 193-nm excimer laser or a 355-nm Nd:YAG laser as the sub-ablative perturbation source. In both cases, the 193-nm excimer laser was used as the probing source. In the case of the 193-nm perturbation source, the GAM excimer laser acts in a dual role. Specifically, the GAM laser will be used to both perturb the collagen sample with a sub-ablative fluence and to probe the transmission through the sample, as shown in Figure 5-1. In the case of the 355-nm perturbation source, the Big Sky frequency tripled Nd:YAG laser (355 nm) perturbed the sample, while the GAM excimer laser acted as the probe beam only. In both cases, the GAM laser beam is immediately passed through an aperture, which passes a circular, central section of the elongated beam to a quartz flat. The flat allows 95% of the beam to transmit through it, while reflecting the remaining 5% of the beam. The higher energy portion may be used as the perturbation beam, and the lower energy portion is the probe beam. For 193-nm experiments, the perturbation beam is turned at a 90^{o} angle and passes through the sample cell, which is detailed in Figure 5-3. For 355-nm experiments, this higher energy excimer beam is blocked with a beam dump, and the Nd:YAG laser beam is reduced with an aperture, then turned at 90^{o} and passed through the sample cell. The 193-nm probe beam passes through 4 mirrors on its path to the sample cell. The length of this path is designed to generate a delay relative to the 193-nm perturbation beam. Approximately one nanosencond of delay is imposed for every foot of beam travel. The optical delay path was designed to achieve 20 ns of pulse separation between the perturbing and probe laser pulses. This was necessary in order to distinguish the probe pulse from the perturbing pulse. Also, it ensured that the

perturbing pulse has ended prior to the start of the probing pulse, as the full pulse-width of the GAM laser is approximately 20 ns. In the case of 355-nm perturbation, the delay was induced using delay generators. The delayed probe beam is collimated and co-incident with the perturbing beam as they pass through the sample cell. Fast phototubes (~200 ps rise time) were used to collect the incident and transmitted light. Optical density filters were used to ensure signal linearity, and 193-nm narrow line filters were used to eliminate fluorescence signal. The detectors were connected to a LeCroy Waverunner oscilloscope, which was used to record the incident and transmitted spectra.

The transmission measurements were taken with two different timing methods. In the first, a perturbation shot was applied, and then the incident and transmitted spectra are recorded. This was repeated ten times, and the spectra were averaged. This was then repeated in intervals, with one shot between each, up to 99 shots total. This is referred to as the synchronized method. In the second, ten perturbation shots were applied to the sample, and then an average of ten incident and transmitted probe spectra was recorded. This also was then repeated in intervals, with one shot between each, up to 99 shots total. This is referred to as the unsynchronized method. The first method allows any dynamic processes that occur on the order of nanoseconds to influence the transmission signal. In the second, several seconds transpire between the perturbation and the transmission probe measurements, thusly any present dynamic processes are expected to have resolved, and the static (or permanent) results will be obtained.

Both collagen and amino acid solutions were analyzed in the sample cell. Collagen Type II derived from calf skin was used to generate the collagen solution by combining 1 mg of collagen per 1 ml of 0.5 N acetic acid. The amino acid solutions were created by placing equal parts of 100 mg each of the amino acids glycine, proline and hydroxyproline per 30 ml 0.5 N acetic acid.

The amino acid solution is essentially equal to the collagen solution less the peptide bonds. In addition, the amino acid solution is ten times more concentrated than the collagen solutions in order to boost the transmission signal, as they are lacking the anticipated primary chromophore, peptide bonds.

The incident probe beam signal was compared to the transmitted probe beam signal to determine the transmission, τ. In general terms, the transmission is defined as the following.

$$\tau = \frac{I(\ell)}{I_0} \tag{5-1}$$

In this equation, $I(\ell)$ is the intensity of the laser light after passing through the solution path length, ℓ, and I_0 is the incident laser intensity. Given the Beer-Lambert law, the absorbance may be calculated from the transmission.

$$\tau = e^{-N\sigma L} \tag{5-2}$$

$$A = 0.434 N\sigma L \tag{5-3}$$

In the above equations, N is the number density of absorbers (cm^{-3}), σ is the absorption cross-section of the absorbers (cm^2), L is the pathlength of the sample (cm), and A is the absorbance of the sample. The total change in transmission may be a result of contributions by both the acetic acid and the collagen or amino acids, such that the total transmission is the product of the transmission due to collagen and the transmission due to acetic acid. The absorbance of the collagen or amino acids may be decoupled from acetic acid and calculated from the following equation.

$$A = -\ln\left(\frac{\tau_{total}}{\tau_{aceticacid}}\right) = -\ln(\tau_{collagen}) \tag{5-4}$$

In order to obtain the transmission of acetic acid only, the experiments were also performed with 0.5 N acetic acid in the sample cell. Once the absorbance is calculated, the number density of

absorbers may be calculated, as the absorption cross-section and pathlength are known. The absorption cross-section is 1.19 E -17 cm^2 per amino acid unit [8]. Other known values include the number of bonds per collagen macromolecule (3,465) and the average atomic mass per macromolecule (308,000 g/gmol) [8]. The number of absolute absorbers may be calculated from the number density by multiplying by the sample volume. In all cases, the diameter of the probe beam is 2.6 mm. For 193-nm perturbations, experiments were performed with 0.55, 0.77, 0.93 and 1.05 mJ/pulse energy. Figure 5-4 shows a representative cross-section of the 193-nm perturbation beam. The beam has a top hat profile. The bounds of the probe beam have been drawn on the Figure to indicate that the probe beam diameter is less than that of the perturbation beam. In summary, the number of absorbers may be calculated from the transmission measurements.

The perturbing pulse had an energy range from approximately 0.5 to 1.2 mJ/pulse over a approximately 2.6-mm beam resulting in a fluence 9 to 21 mJ/cm^2, while the probing pulse had a fluence of less than 0.5 mJ/cm^2. For 355-nm perturbations, experiments were performed with 0.48 and 1.2 mJ/pulse energy. For each energy, three films of sample solution (collagen or amino acid) were analyzed along with three films of acetic acid solution, with four spots on each, for a total of 12 experiments. The number of laser pulses converts into number of cumulative photons using the relation following relation:

$$E_p = h\nu = h\frac{c}{\lambda} \tag{5-5}$$

In the above equation, E_p is the photon energy, h is Planck's constant, ν is the frequency of the laser light, c is the speed of light, and λ is the wavelength of the laser. The total pulse energy, E_T, can then be divided by the photon energy to get the number of photons per laser pulses, n.

$$n = \frac{E_T}{E_p} \tag{5-6}$$

Therefore, the number of absorbers may be calculated with respect to the number of incident photons.

Sub-Ablative Results

The results are presented in two sections. The 193-nm excimer perturbation results will be discussed first, followed by the results of 355-nm perturbation results. The results will be discussed with respect to each other in the summary section to follow.

193-nm Perturbations

An example of the raw incident and transmitted signal spectra obtained from the oscilloscope is shown in Figure 5-5. In the figure, the peak-to-peak pulse separation is 18 ns. As this separation is due to the physical delay path, there is no jitter in the time separation. In order to convert this data into transmission, the transmitted and incident probe beam signals were first summed, then the background signal was subtracted from the sums, and the ratio of the two was taken.

Using Equation 5-4, the absorbance for each sample was calculated for each time increment and pulse energy for both timing schemes (synchronized and unsynchronized). The average absorbance values of all twelve repetitions for each condition are presented in Table 5-1 with their corresponding standard deviations for collagen solutions. The results for amino acid solutions are presented in Table 5-2. It is noted that the reference acetic acid signal did not vary with number of shots applied, and was constant for each perturbation energy. From looking at these two tables, two trends are observed. First, the absorbance decreases with the number of perturbation shots for both the synchronized and unsynchronized cases. Second, the absorbance values are less for the synchronized case than the unsynchronized case.

To further analyze the data, the extinction coefficients (Nσ) were calculated by dividing the absorbance by the pathlength of 0.0084 cm. This pathlength was determined by plugging in the average collagen transmission value of approximately 0.5 into Equation 5-2 along with the values of σ (1.19E-17 cm2) and N (6.77E18 cm^{-3}) for the amino acid unit (amino acid + peptide bond). This value of N is calculated from published values of the molecular mass of an amino acid unit (308,000 g/mol) and the number of peptide bonds per collagen macromolecule (3,465). The constant values were obtained from the work of Fisher and Hahn [8]. This calculated pathlength is consistent with physical measurements of the collagen cells.

The calculated extinction coefficients have been tabulated for both timing variations and all energies with respect to the number of incident photons as calculated using Equations 5-5 and 5-6. Table 5-3 includes all values for collagen solutions, while Table 5-4 includes all values for amino acid solutions. In order to further examine the trends in the data, the extinction values have all been plotted (Figures 5-6, 5-7, 5-8 and 5-9 for collagen solutions; Figure 5-10 for amino acid solutions). For collagen solutions, there is a decrease in extinction coefficient with photons, but the extinction coefficient remains constant for amino acids. For further calculations, the average amino acid extinction coefficient for synchronized (43.58, σ=1.44) and unsynchronized series (54.82, σ=1.66) will be used. In both solutions, there is a clear offset between the synchronized and unsynchronized cases, which indicates the presence of a dynamic component. The overall downward trend of the unsynchronized data confirms that a steady-state change is induced in the collagen solutions.

The dynamic component was first analyzed in the context of the amino acid solutions. The change in extinction coefficient with respect to incident photons may be calculated from the following equation:

$$\frac{dK}{dn} = \frac{\overline{K}_{unsync} - \overline{K}_{sync}}{n} \tag{5-7}$$

In the above equation, $\frac{dK}{dn}$ is the change in extinction coefficient with respect to incident photons, $\overline{K}$ is the average extinction coefficient and n is the number of photons per pulse. The value obtained for $\frac{dK}{dn}$ is -1.24E-14 cm^{-1}/photon, σ=2.43E-15. The number density of absorbers (1.41E20 amino acid per cm^3, σ=8.68E18) is also constant and was calculated by dividing by the absorption cross-section of 4.74E-19 cm^2 for the amino acids [8]. Lastly, the number of absorbers (2.56E23 amino acid units, σ=1.95E22) was calculated by multiplying the density by the sample volume of 0.445 mm^3.

The extinction coefficients of the unsynchronized collagen series are analyzed next. From this data, the number of peptide bonds may be calculated at each time step by resolving the overall extinction coefficient into its peptide bond and amino acid contributions using the following equation:

$$K_{ext,unsync} = K_p + K_{AA} = \sigma_{AAU} N_{AAU} = \sigma_p N_p + \sigma_{AA} N_{AA} \tag{5-8}$$

In the above equation, the subscripts AAU, P and AA are used to denote amino acid unite, peptide bond and amino acid, respectively. This equation can be rearranged to the following:

$$N_P = \frac{\left(N_{AAU} - \left(\frac{\sigma_{AA}}{\sigma_{AAU}} \right) N_{AA} \right)}{\left(\frac{\sigma_P}{\sigma_{AAU}} \right)} = \frac{N_{AAU} - (0.04) N_{AA}}{(0.96)} \tag{5-9}$$

The absorption cross-section ratios for amino acids and peptide bonds are known as 0.04 and 0.96, respectively [8]. The number density of the amino acid units per each time step is easily calculated from the overall extinction coefficient by dividing by the absorption cross-section of

1.19 E -17 cm^2. The number density of the amino acids is constant, as seen from the amino acid experiments that there is no steady-state reduction of absorbers. Finally, the number of absorbers was calculated by multiplying the density by the sample volume of 0.445 mm^3. The average number density and number of absorbers of all twelve repetitions of collagen solution experiments for each condition is presented in Table 5-5 with their corresponding standard deviations with respect to the cumulative number of photons. The number densities have been plotted for each perturbation energy in Figures 5-11, 5-12, 5-13 and 5-14 for collagen solutions.

Linear regression curve fits may be applied to determine the reduction in number density per photon for each condition studied. The resulting curve fits are displayed on the plots and the R^2 values are all greater than 0.979. These slopes have been plotted verses perturbation energy in Figure 5-15. These slopes can easily be used to determine the number of photons required to break a single peptide bond by multiplying by the sample volume and taking the inverse. These results are presented in Table 5-6. In both the plot and the table, the values are consistent with each other, particularly for the last three energies. The lowest energy of 0.55 mJ/pulse was obtained by reducing the output of the GAM laser, and as the laser output is reduced, the less reliable the output energy becomes. Including the 0.55 mJ/pulse data point, the average number of photons to break a peptide bond is 28. Excluding the 0.55 mJ/pulse data point, the average number of photons to break a peptide bond is 29.

Lastly, the synchronized collagen data is analyzed to find the contribution of the peptide bond to the transient reduction of extinction coefficient. The synchronized extinction coefficient may be defined by the following equations.

$$\left(K_{ext,sync}\right)_{n+dn} = \left(K_{ext}\right)_P + \left(K_{ext}\right)_{AA} \tag{5-10}$$

$$\left(K_{ext,sync}\right)_{n+dn} = \left(\sigma_P N_P\right)_n + \frac{d(\sigma_P N_P)}{dn}\Delta n + \left(\sigma_{AA} N_{AA}\right)_n + \frac{d(\sigma_{AA} N_{AA})}{dn}\Delta n \tag{5-11}$$

This equation can be solved for $\frac{d(\sigma_P N_P)}{dn}$ and simplified into the following equation:

$$\frac{d(\sigma_P N_P)}{dn} = \frac{d(K_P)}{dn} = \left(\frac{\left(K_{ext,sync}\right)_{n+dn} - \left(K_{ext,unsync}\right)_{n+dn} - \left(\frac{N_{Coll,o}}{N_{AA,o}}\right)\frac{d(K_{AA})}{dn}\Delta n}{\Delta n} \right) \quad (5\text{-}12)$$

The term $\frac{d(K_{AA})}{dn}$ is constant and was calculated using the amino acid experiments above. $K_{ext,sync}$ and $K_{ext,unsync}$ have been calculated for each time step for each perturbation energy. The value Δn is the number of photons per pulse. Due to the different concentrations of the amino acid and collagen solutions, a correction factor was placed in front of the $\frac{d(K_{AA})}{dn}$ term to compensate. This factor is the ratio of the initial overall number density of the collagen solution to the initial overall number density of the amino acid solution. In this manner, the dynamic change in extinction coefficient due to the peptide bonds per photon was determined for each time step.

The values of $\frac{d(K_P)}{dn}$ are tabulated in Table 5-7. Additionally, these values were normalized by the number of peptide bonds. The calculated value of $\frac{d(K_{AA})}{dn}$ is -1.24E-14, σ=2.43E-15) and its normalized value is -1.09E-34, σ=2.29E-35 as determined by dividing by the number of amino acids, can be compared with these values. The change in the dynamic extinction coefficient (synchronized) per photon has two contributions: amino acids and peptide bonds. By comparing the normalized values, it is noted that on average, the portion due to amino acids is only 5% of the portion due to peptide bonds.

In an attempt to see any changes in the trends of synchronized and unsynchronized transmission during the laser pulse timing, the ratio of the transmitted to the incident peak was calculated for each time step in the laser pulse. For this exercise, 10 recorded spectra were averaged at 0.77 mJ/pulse for the synchronized and unsynchronized cases. The ratios were taken and plotted in Figure 5-16. The synchronized transmission ratio is always slightly greater than the unsynchronized ratio as expected; however, there is no clear difference in the transmitted ratio trends between the synchronized and unsynchronized cases.

With regards to the dynamic component, for both collagen and amino acid solutions, the measured number of absorbers in the sample is less in the synchronized case than in the unsynchronized case. The observation indicates transient reduction in number of absorbers in the sample that is present on the order of nanoseconds following perturbation, but has resolved on the order of tens of seconds. In the case of amino acid solutions, the dynamic reduction is the only reduction that occurs, while the steady state number of absorbers remains unchanged. In stark contrast, the collagen solutions show both a dynamic and a long-term reduction in the number of absorbers. The source of the dynamic reduction is most likely photobleaching (which is not intended to imply saturation) of the sample, wherein the sample becomes temporarily excited by the incident photons. The excited state has a reduced (or zero) cross-section. This excitation relaxes over time leaving no permanent chemical change in the solution. Recalling that the difference between the collagen and amino acid solutions is the presence of peptide bonds, the permanent change induced in the collagen samples must be due to scission of the peptide bonds in the solution. This confirms that the peptide bond is the primary chromophore in the case of sub-ablative perturbations in the range of 0.55 to 1.2 mJ/pulse.

355-nm Perturbations

An example of the raw incident and transmitted signal spectra obtained from the oscilloscope is shown in Figure 5-17. In this figure, only the probe peaks are of interest. The detectors pick up some small amount of reflections of the non-delayed 193-nm light. One detector was temporarily relocated in order to measure the time difference between the 355-nm perturbation and 193-nm probe beams, as shown in Figure 5-18. In the figure, the peak-to-peak pulse separation is 19 ns. The average pulse-to-pulse separation was calculated as 19 ns. Three timing measurements were taken before and after each film was analyzed. As this separation is created with a delay generator, there is jitter in the time separation resulting from the internal jitter of both the excimer and the Nd:YAG lasers. This jitter is approximately +/- 3 ns. In order to convert this data into transmission, the transmitted and incident probe beam signals were first summed, then the background signal was subtracted from the sums, and the ratio of the two was taken. It is again noted that the background (acetic acid) signal did not vary with number of shots applied. Amino acid solutions were not examined with the 355-nm perturbation source, as the photon energy is less than in the case of the 194-nm perturbations. As no long-term changes were noted with amino acid solutions with the more energetic perturbation source, none are anticipated with this less energetic perturbation source.

Using Equation 5-4, the absorbance for each collagen sample was calculated for each time increment and pulse energy for both timing schemes (synchronized and unsynchronized). The average absorbance values of all twelve repetitions for each condition are presented in Table 5-8 with their corresponding standard deviations.

The extinction coefficient ($N\sigma$) was next calculated by dividing the absorbance by the pathlength of 0.0084 cm. The extinction coefficient has been tabulated and plotted for both

timing variations and all energies with respect to the number of incident photons as calculated using Equations 5-5 and 5-6 (Table 5-9, Figures 5-19 and 5-20). The extinction coefficient has no slope in the 0.48 mJ/pulse case. In the case of 1.2 mJ/pulse perturbations, there is a slight downward trend, but not a significant one relative to the 193-nm perturbations. The number of photons delivered in this case is nearly twice the maximum delivered for the case of 193-nm perturbations (1.05 mJ/pulse). There is a change of less than only 2.4 cm^{-1} with 5.24E16 incident photons compared to 51.3 cm^{-1} with 4.49E16 incident photons. This corresponds to 508 incident photons required to break a bond. This is extinction coefficient reduction is only 4.5% of that observed for 1.05 mJ/pulse.

The collagen solutions for 355-m perturbations also show both a dynamic and a long-term reduction in the number of absorbers, likely due to photobleaching (which is not intended to imply saturation) of the sample, wherein the sample becomes temporarily excited by the incident photons. The excited state has a reduced (or zero) cross-section. The 355-nm permanent change induced in the collagen samples is very small compared to the changes induced by 193-nm perturbations. This change may be due to scission of the peptide bonds in the solution; however, relative to 193-nm perturbation, very few peptide bonds are broken. This is an anticipated result, as at longer wavelengths, the mechanism of ablation is suggested as thermal in nature. In an extensive review, Vogel and Venugopalan concluded that ablation at 193-nm includes both photochemical and photothermal processes, with photochemical components taking a significant role. Particularly, photochemical processes become dominant around wavelengths less than 200 nm, with thermal processes more relevant at greater wavelengths. Thus, the 355-nm perturbations results also confirm that the peptide bond is the primary chromophore in the case of sub-ablative 193-nm perturbations in the range of 0.55 to 1.2 mJ/pulse (9 to 21 mJ/cm^2).

Sub-Ablative Summary

The sub-ablative 193-nm and 355-nm perturbations yielded insight into 193-nm and 355-nm excitation of collagen and amino acids. Amino acid solutions were not permanently altered by 193-nm sub-ablative energies. For collagen solutions, an average of 28 photons at 193 nm was required to break a single peptide bond. In contrast, perturbations of collagen solutions by 355-nm resulted in only 4.5% of the extinction coefficient obtained by 193-nm perturbations. Additionally, 508 incident photons at 355-nm were required to break a bond.

A dynamic photobleaching (which is not intended to imply saturation) occurs at both 193-nm and 355-nm perturbations, wherein the sample becomes temporarily excited by the incident photons. The excited state has a reduced (or zero) cross-section. This effect is approximately 338% greater at 193 nm than at 355 nm. It is also present for both amino acid and collagen solutions. The effect resolves itself by a time scale of some seconds and does not have a long-term affect on the solutions. The source of this dynamic reduction is most likely photobleaching of the sample, wherein the sample becomes temporarily excited by the incident photons to an electronic state with a reduced absorption coefficient. This excitation relaxes over time leaving no permanent chemical change in the solution. Recalling that the difference between the collagen and amino acid solutions is the presence of peptide bonds, the permanent change induced in the collagen samples must be due to scission of the peptide bonds in the solution. This confirms that the peptide bond is the primary chromophore in the case of sub-ablative perturbations in the range of 0.55 to 1.2 mJ/pulse (9 to 21 mJ/cm^2). These results point to a photochemical mechanism of sub-ablative perturbations of collagen solution. It was previously supposed that at sub-ablative conditions only thermal mechanisms were present. This study contradicts this belief, as photothermal mechanisms are quantified.

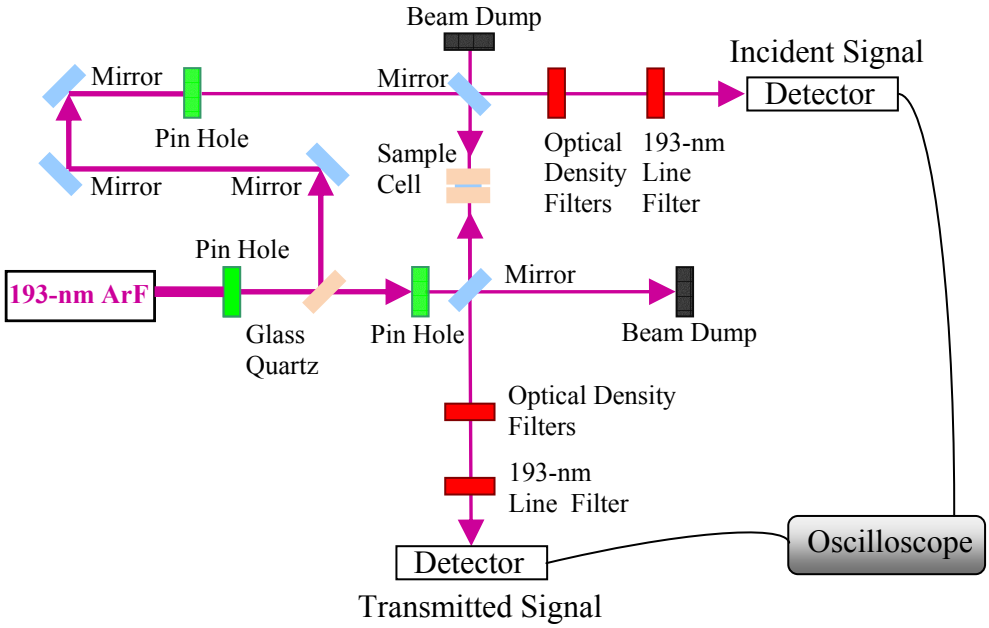

Figure 5-1. Schematic of the sub-ablative experimental setup using 193-nm perturbation

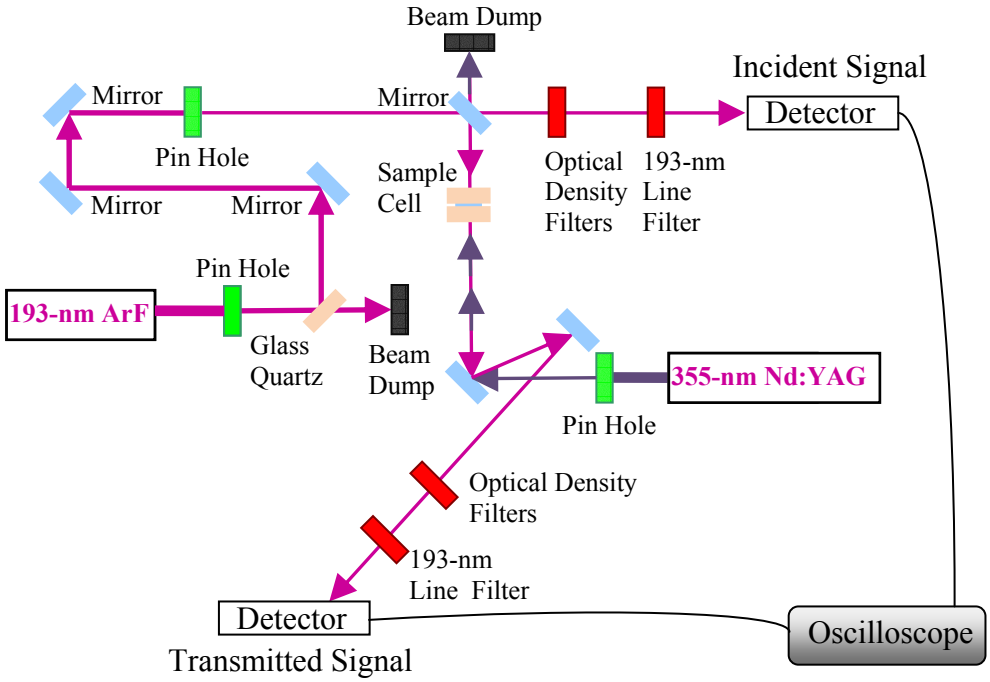

Figure 5-2. Schematic of the sub-ablative experimental setup using 355-nm perturbation

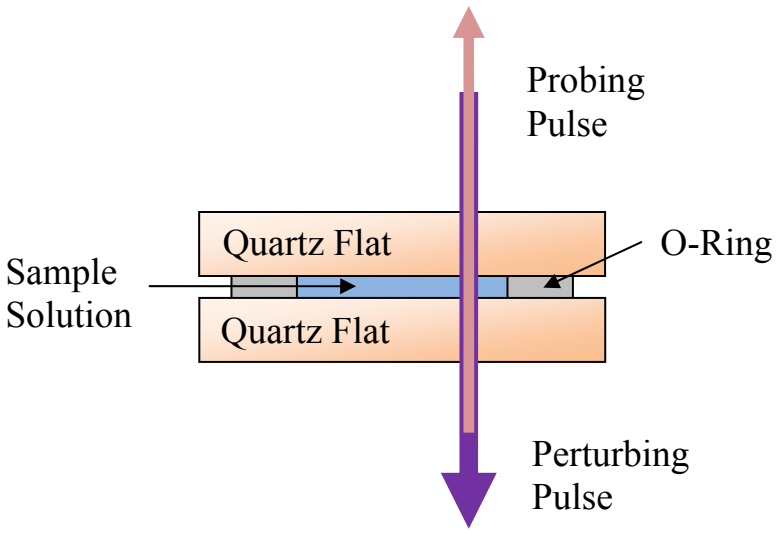

Figure 5-3. Schematic of the sample cell used in the sub-ablative experimental setup

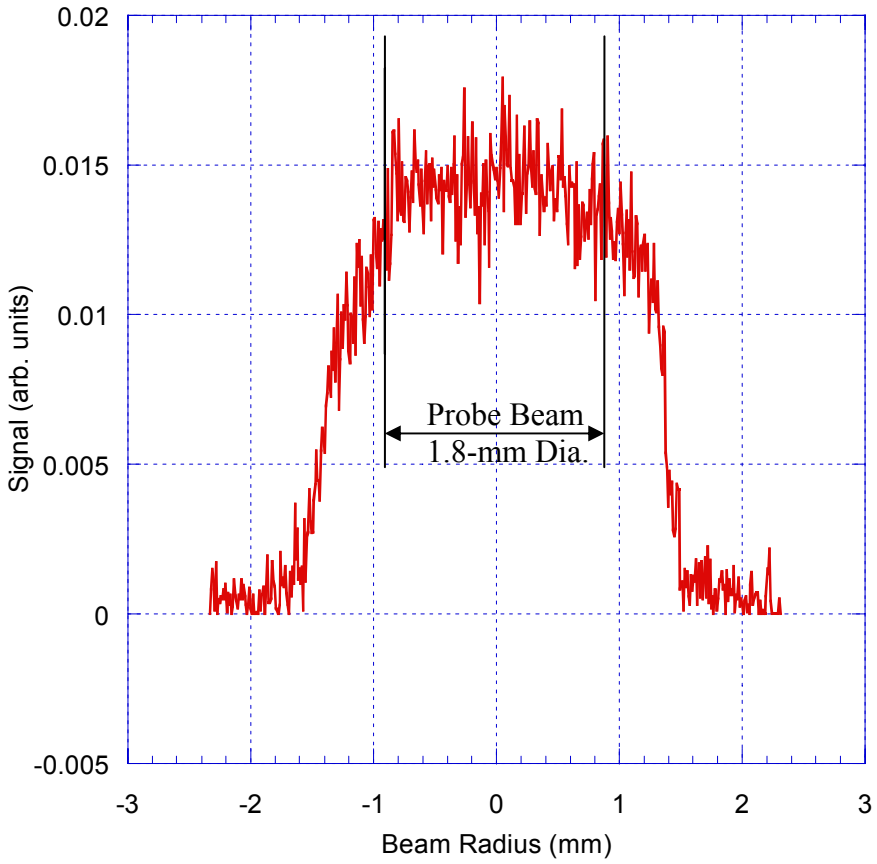

Figure 5-4. Representative profile of the 193-nm perturbation beam

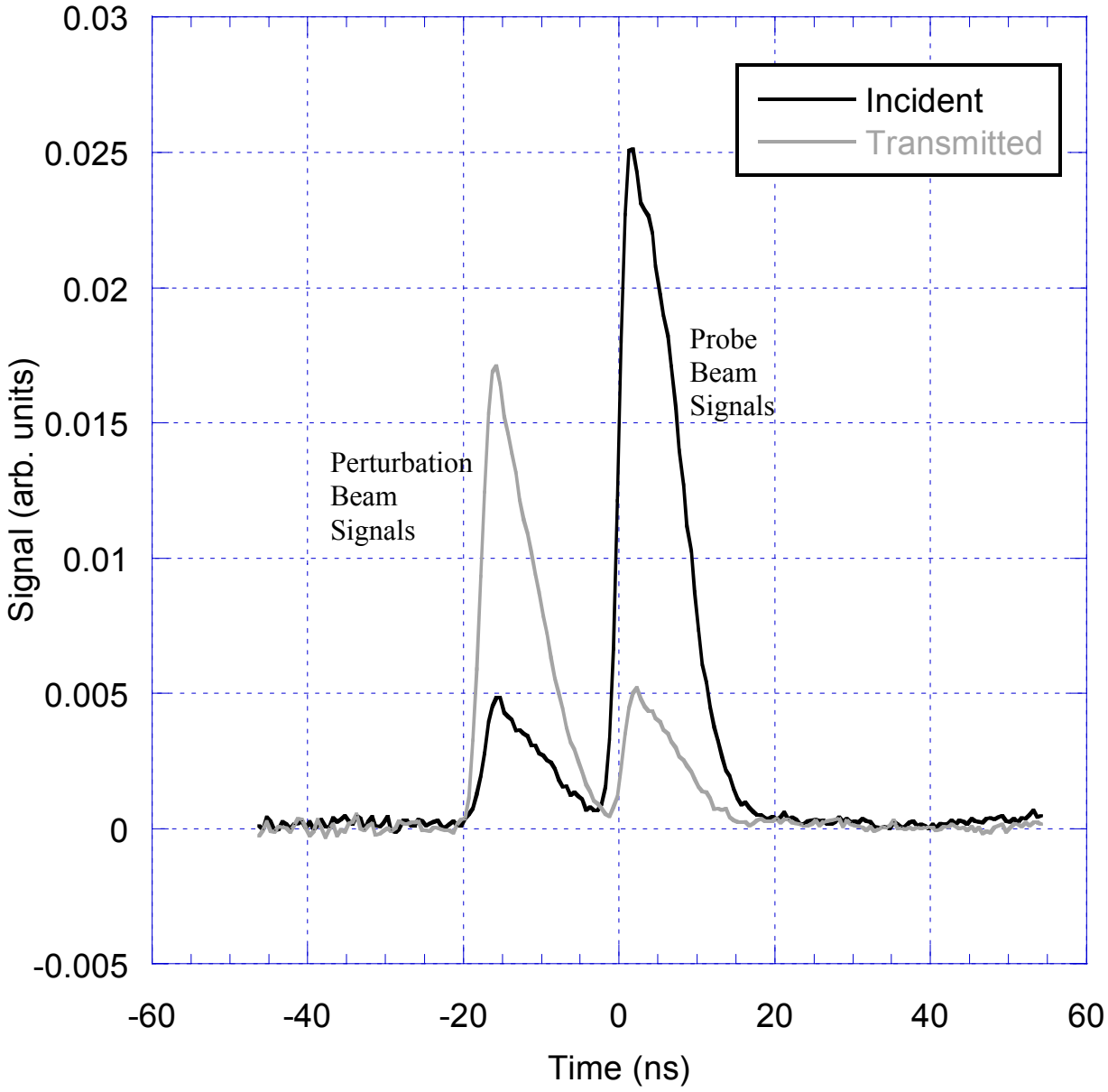

Figure 5-5. Example of oscilloscope output for 193-nm perturbation

Table 5-1. Average absorbance values and standard deviations for each pulse energy and time step with 193-nm perturbation of collagen solutions

Perturbation energy (mJ/pulse)	Number of pulses	Synchronized Average absorbance	Synchronized Standard deviation absorbance	Un Synchronized Average absorbance	Un Synchronized Standard deviation absorbance
0.55	0	0.746	0.084	0.746	0.084
	11	0.602	0.056	0.700	0.058
	22	0.579	0.057	0.669	0.060
	33	0.563	0.049	0.648	0.049
	44	0.541	0.054	0.621	0.051
	55	0.517	0.042	0.610	0.047
	66	0.503	0.050	0.578	0.051
	77	0.485	0.041	0.561	0.048
	88	0.469	0.048	0.545	0.049
	99	0.446	0.039	0.527	0.044
0.77	0	0.877	0.035	0.877	0.035
	11	0.733	0.027	0.854	0.031
	22	0.708	0.032	0.821	0.028
	33	0.669	0.026	0.779	0.033
	44	0.647	0.023	0.752	0.027
	55	0.623	0.024	0.732	0.030
	66	0.599	0.028	0.708	0.026
	77	0.584	0.024	0.680	0.027
	88	0.559	0.021	0.665	0.028
	99	0.542	0.023	0.641	0.023
0.93	0	0.849	0.082	0.849	0.082
	11	0.699	0.065	0.821	0.073
	22	0.663	0.069	0.776	0.082
	33	0.620	0.053	0.730	0.074
	44	0.590	0.056	0.695	0.071
	55	0.560	0.044	0.665	0.068
	66	0.525	0.060	0.623	0.085
	77	0.500	0.053	0.602	0.077
	88	0.484	0.060	0.572	0.077
	99	0.447	0.062	0.547	0.078
1.05	0	0.884	0.044	0.884	0.044
	11	0.684	0.039	0.844	0.041
	22	0.645	0.036	0.792	0.041
	33	0.611	0.037	0.756	0.042
	44	0.574	0.038	0.720	0.039
	55	0.547	0.039	0.686	0.035
	66	0.522	0.036	0.653	0.034
	77	0.499	0.035	0.622	0.031
	88	0.472	0.033	0.578	0.026
	99	0.453	0.040	0.570	0.027

Table 5-2. Average absorbance values and standard deviations for each pulse energy and time step with 193-nm perturbation of amino acid solutions

Perturbation energy (mJ/pulse)	Number of pulses	Synchronized Average absorbance	Synchronized Standard deviation absorbance	Un Synchronized Average absorbance	Un Synchronized Standard deviation absorbance
0.93	0	0.453	0.034	0.453	0.034
	11	0.355	0.033	0.451	0.037
	22	0.364	0.035	0.458	0.038
	33	0.363	0.035	0.461	0.041
	44	0.364	0.035	0.461	0.044
	55	0.365	0.037	0.460	0.043
	66	0.368	0.035	0.459	0.040
	77	0.366	0.038	0.459	0.045
	88	0.372	0.038	0.464	0.042
	99	0.371	0.039	0.461	0.044

Table 5-3. Average extinction coefficient (cm^{-1}) values and standard deviations for each pulse energy and time step with 193-nm perturbation of collagen solutions

Perturbation energy (mJ/pulse)	Cumulative photons	Synchronized Average extinction coefficient (cm^{-1})	Synchronized Standard deviation extinction coefficient (cm^{-1})	Un Synchronized Average extinction coefficient (cm^{-1})	Un Synchronized Standard deviation extinction coefficient (cm^{-1})
0.55	0.00E+00	89.00	10.01	89.00	10.01
	2.61E+15	71.85	6.66	83.54	6.93
	5.22E+15	69.09	6.79	79.84	7.20
	7.83E+15	67.12	5.85	77.31	5.90
	1.04E+16	64.56	6.39	74.05	6.09
	1.31E+16	61.71	5.01	72.83	5.63
	1.57E+16	59.95	5.99	69.02	6.07
	1.83E+16	57.91	4.95	66.98	5.68
	2.09E+16	56.00	5.75	65.01	5.83
	2.35E+16	53.19	4.68	62.83	5.22
0.77	0.00E+00	104.68	4.20	104.68	4.20
	3.65E+15	87.45	3.22	101.92	3.67
	7.31E+15	84.45	3.88	97.95	3.37
	1.10E+16	79.87	3.15	92.95	3.89
	1.46E+16	77.21	2.69	89.73	3.19
	1.83E+16	74.32	2.90	87.32	3.55
	2.19E+16	71.51	3.35	84.47	3.06
	2.56E+16	69.69	2.91	81.10	3.17
	2.92E+16	66.73	2.55	79.33	3.32
	3.29E+16	64.61	2.72	76.43	2.74
0.93	0.00E+00	101.27	9.81	101.27	9.81
	4.41E+15	83.35	7.72	97.91	8.74
	8.83E+15	79.12	8.21	92.62	9.73
	1.32E+16	73.94	6.34	87.14	8.87
	1.77E+16	70.40	6.63	82.97	8.43
	2.21E+16	66.86	5.25	79.37	8.09
	2.65E+16	62.59	7.16	74.31	10.13
	3.09E+16	59.68	6.30	71.78	9.20
	3.53E+16	57.68	7.11	68.25	9.20
	3.97E+16	53.37	7.43	65.22	9.30
1.05	0.00E+00	105.41	5.21	105.41	5.21
	4.98E+15	81.64	4.67	100.68	4.85
	9.97E+15	77.00	4.26	94.44	4.92
	1.50E+16	72.92	4.46	90.16	4.95
	1.99E+16	68.47	4.56	85.86	4.64
	2.49E+16	65.22	4.66	81.86	4.13
	2.99E+16	62.29	4.28	77.88	4.02
	3.49E+16	59.51	4.17	74.26	3.69
	3.99E+16	56.34	3.94	68.94	3.16
	4.49E+16	54.08	4.80	68.01	3.17

Table 5-4. Average extinction coefficient (cm^{-1}) values and standard deviations for each pulse energy and time step with 193-nm perturbation of amino acid solutions

Perturbation energy (mJ/pulse)	Cumulative photons	Synchronized Average extinction coefficient (cm^{-1})	Synchronized Standard deviation extinction coefficient (cm^{-1})	Un Synchronized Average extinction coefficient (cm^{-1})	Un Synchronized Standard deviation extinction coefficient (cm^{-1})
0.93	0.00E+00	54.07	4.12	54.07	4.12
	4.41E+15	42.37	3.90	53.78	4.41
	8.83E+15	43.37	4.15	54.68	4.55
	1.32E+16	43.30	4.21	55.02	4.94
	1.77E+16	43.48	4.22	55.00	5.22
	2.21E+16	43.58	4.46	54.91	5.16
	2.65E+16	43.88	4.22	54.80	4.78
	3.09E+16	43.62	4.48	54.79	5.36
	3.53E+16	44.34	4.59	55.39	4.99
	3.97E+16	44.25	4.65	54.97	5.21

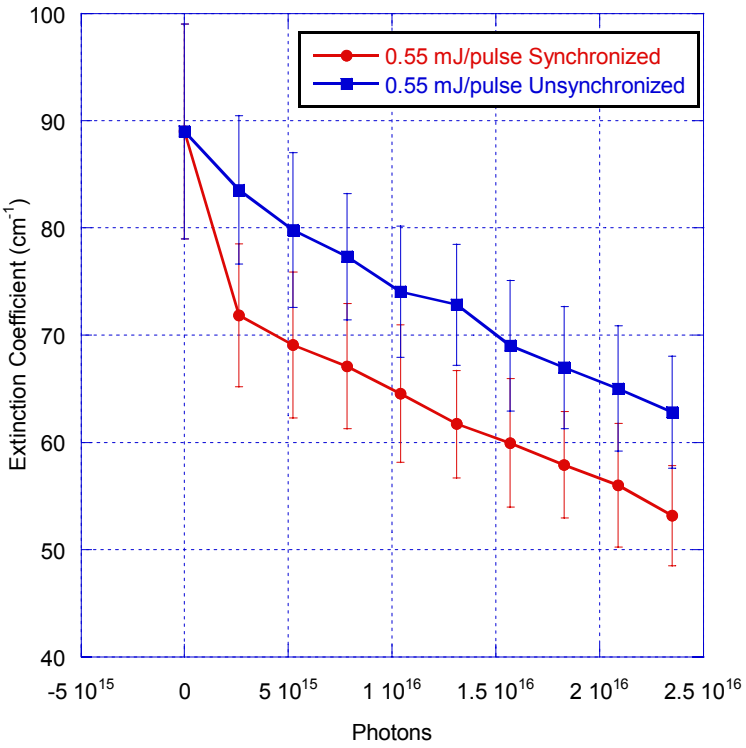

Figure 5-6. Average extinction coefficient (σN) and standard deviations for 0.55 mJ/pulse energy and time step with 193-nm perturbation of collagen solutions

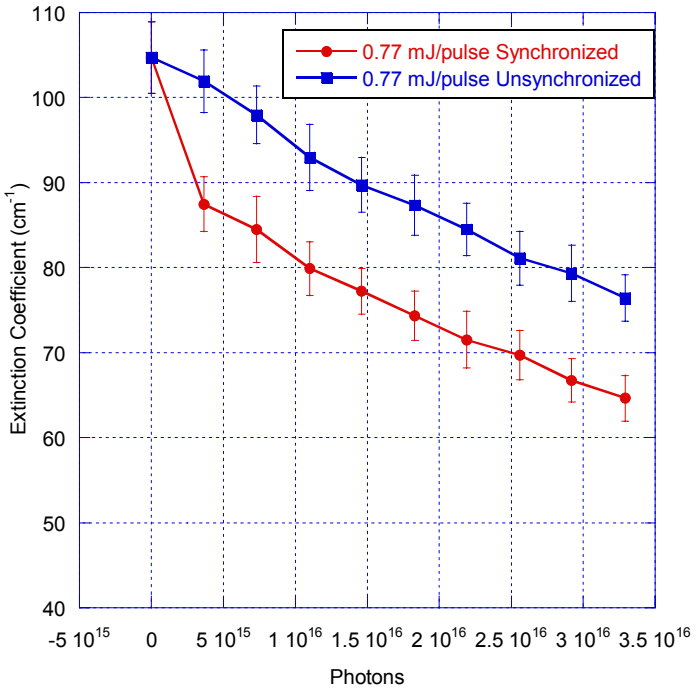

Figure 5-7. Average extinction coefficient (σN) and standard deviations for 0.77 mJ/pulse energy and time step with 193-nm perturbation of collagen solutions

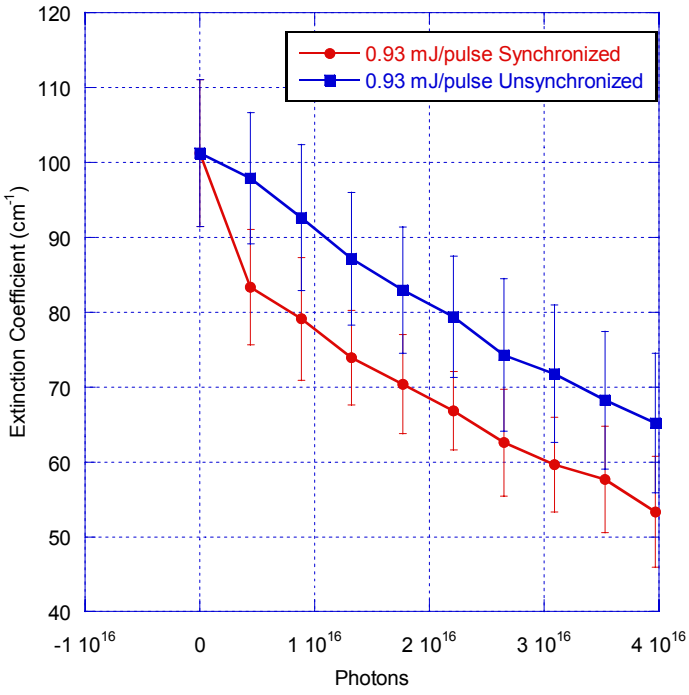

Figure 5-8. Average extinction coefficient (σN) and standard deviations for 0.93 mJ/pulse energy and time step with 193-nm perturbation of collagen solutions

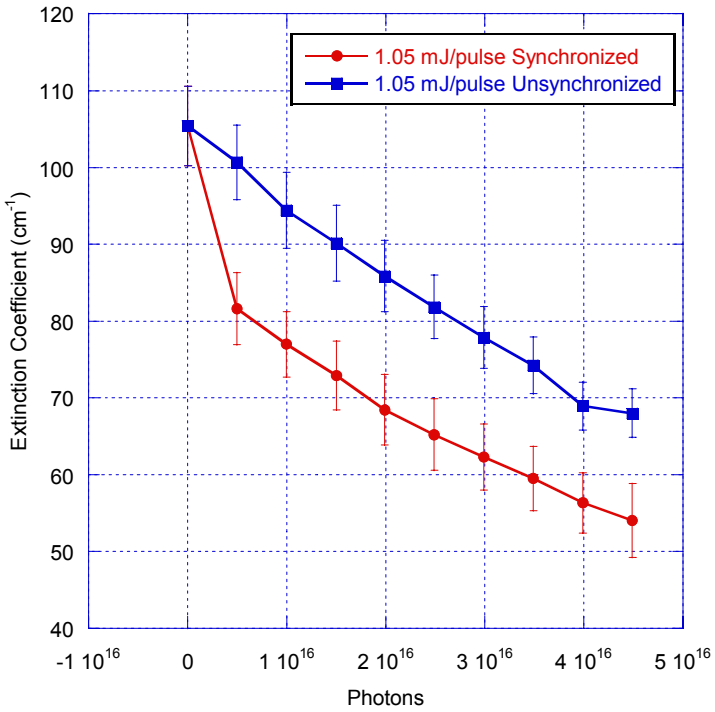

Figure 5-9. Average extinction coefficient (σN) and standard deviations for 1.05 mJ/pulse energy and time step with 193-nm perturbation of collagen solutions

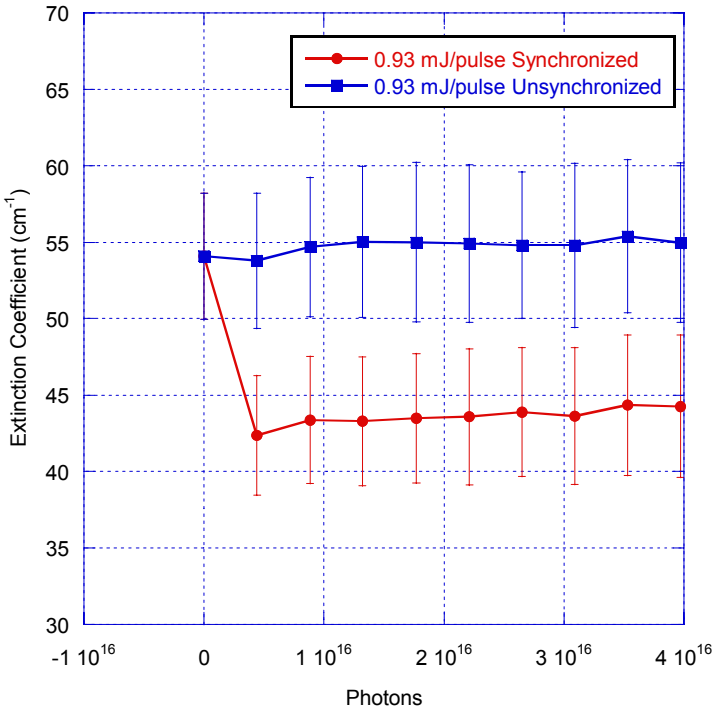

Figure 5-10. Average extinction coefficient (σN) and standard deviations for 0.93 mJ/pulse energy and time step with 193-nm perturbation of amino acid solutions

Table 5-5. Average bond number densities (peptide bonds/ml) and numbers of absorbers (peptide bonds) and standard deviations for each pulse energy and time step with 193-nm perturbation of collagen solutions

Perturbation energy (mJ/pulse)	Cumulative photons	Peptide number density (bonds/ml)	Peptide number density standard deviation (bonds/ml)	Peptide number density (bonds)	Peptide number density standard deviation (bonds)
0.55	0.00E+00	7.48E+18	8.41E+17	3.33E+15	3.74E+14
	2.61E+15	6.96E+18	7.01E+17	3.10E+15	3.12E+14
	5.22E+15	6.63E+18	6.76E+17	2.95E+15	3.01E+14
	7.83E+15	6.41E+18	5.75E+17	2.85E+15	2.56E+14
	1.04E+16	6.13E+18	5.72E+17	2.73E+15	2.55E+14
	1.31E+16	6.02E+18	5.37E+17	2.68E+15	2.39E+14
	1.57E+16	5.69E+18	5.67E+17	2.53E+15	2.52E+14
	1.83E+16	5.51E+18	5.41E+17	2.45E+15	2.41E+14
	2.09E+16	5.34E+18	5.47E+17	2.37E+15	2.44E+14
	2.35E+16	5.15E+18	5.00E+17	2.29E+15	2.23E+14
0.77	0.00E+00	8.80E+18	3.53E+17	3.91E+15	1.57E+14
	3.65E+15	8.57E+18	3.53E+17	3.81E+15	1.57E+14
	7.31E+15	8.22E+18	3.22E+17	3.66E+15	1.43E+14
	1.10E+16	7.78E+18	3.61E+17	3.46E+15	1.61E+14
	1.46E+16	7.50E+18	3.11E+17	3.34E+15	1.38E+14
	1.83E+16	7.29E+18	3.31E+17	3.24E+15	1.47E+14
	2.19E+16	7.04E+18	2.96E+17	3.13E+15	1.32E+14
	2.56E+16	6.74E+18	2.97E+17	3.00E+15	1.32E+14
	2.92E+16	6.59E+18	3.11E+17	2.93E+15	1.39E+14
	3.29E+16	6.34E+18	2.67E+17	2.82E+15	1.19E+14
0.93	0.00E+00	8.51E+18	8.24E+17	3.79E+15	3.67E+14
	4.41E+15	8.22E+18	8.39E+17	3.66E+15	3.73E+14
	8.83E+15	7.75E+18	9.05E+17	3.45E+15	4.03E+14
	1.32E+16	7.27E+18	8.48E+17	3.24E+15	3.77E+14
	1.77E+16	6.91E+18	8.01E+17	3.07E+15	3.56E+14
	2.21E+16	6.59E+18	7.68E+17	2.93E+15	3.42E+14
	2.65E+16	6.15E+18	9.31E+17	2.74E+15	4.14E+14
	3.09E+16	5.93E+18	8.80E+17	2.64E+15	3.92E+14
	3.53E+16	5.62E+18	8.67E+17	2.50E+15	3.86E+14
	3.97E+16	5.35E+18	8.75E+17	2.38E+15	3.90E+14
1.05	0.00E+00	8.86E+18	4.38E+17	3.94E+15	1.95E+14
	4.98E+15	8.46E+18	4.62E+17	3.76E+15	2.06E+14
	9.97E+15	7.91E+18	4.63E+17	3.52E+15	2.06E+14
	1.50E+16	7.54E+18	4.67E+17	3.35E+15	2.08E+14
	1.99E+16	7.16E+18	4.42E+17	3.19E+15	1.97E+14
	2.49E+16	6.81E+18	3.96E+17	3.03E+15	1.76E+14
	2.99E+16	6.46E+18	3.81E+17	2.88E+15	1.69E+14
	3.49E+16	6.15E+18	3.53E+17	2.74E+15	1.57E+14
	3.99E+16	5.68E+18	3.05E+17	2.53E+15	1.36E+14
	4.49E+16	5.60E+18	2.98E+17	2.49E+15	1.33E+14

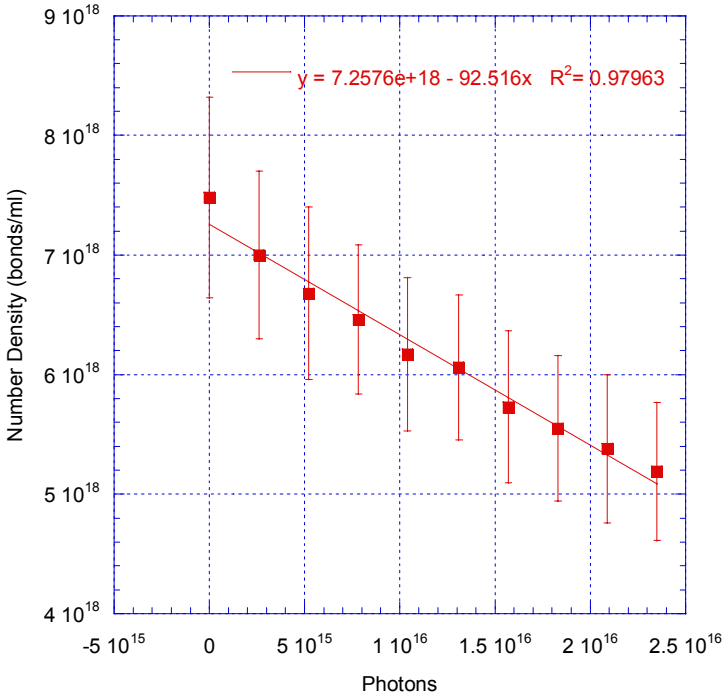

Figure 5-11. Average number densities (bonds/ml) of peptide bonds and standard deviations for 0.55 mJ/pulse energy and time step with 193-nm perturbation of collagen solutions

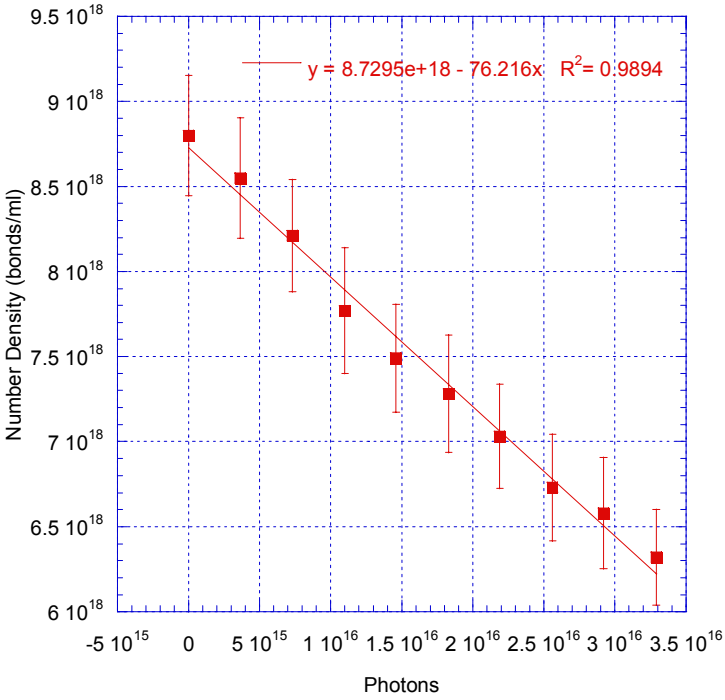

Figure 5-12. Average number densities (bonds/ml) of peptide bonds and standard deviations for 0.77 mJ/pulse energy and time step with 193-nm perturbation of collagen solutions

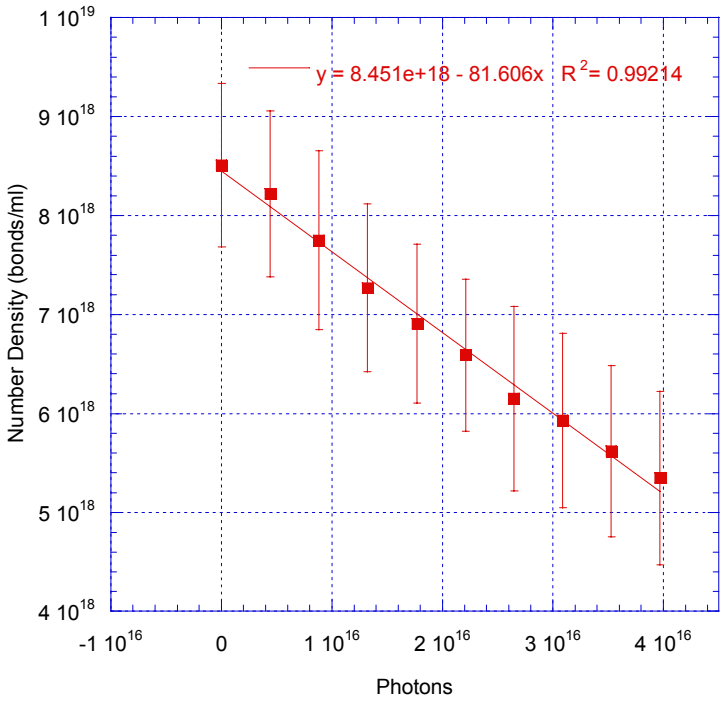

Figure 5-13. Average number densities (bonds/ml) of peptide bonds and standard deviations for 0.93 mJ/pulse energy and time step with 193-nm perturbation of collagen solutions

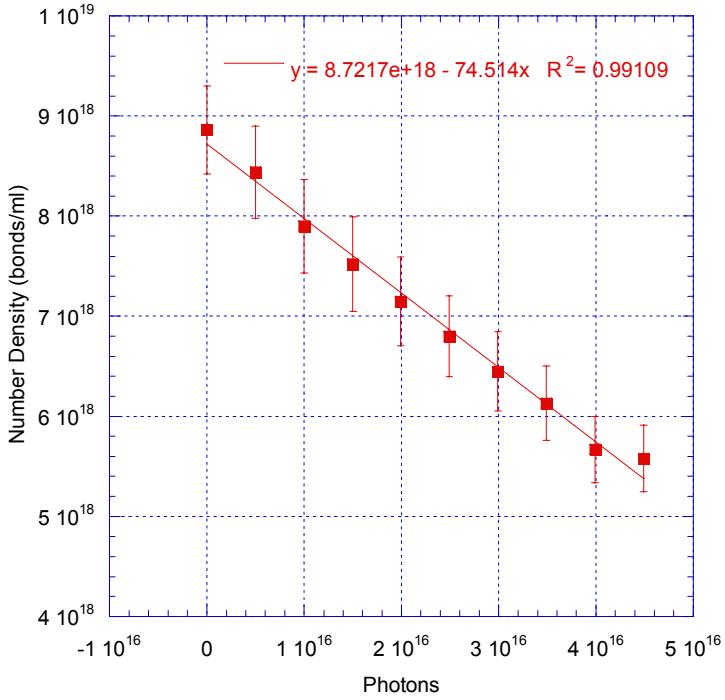

Figure 5-14. Average number densities (bonds/ml) of peptide bonds and standard deviations for 1.05 mJ/pulse energy and time step with 193-nm perturbation of collagen solutions

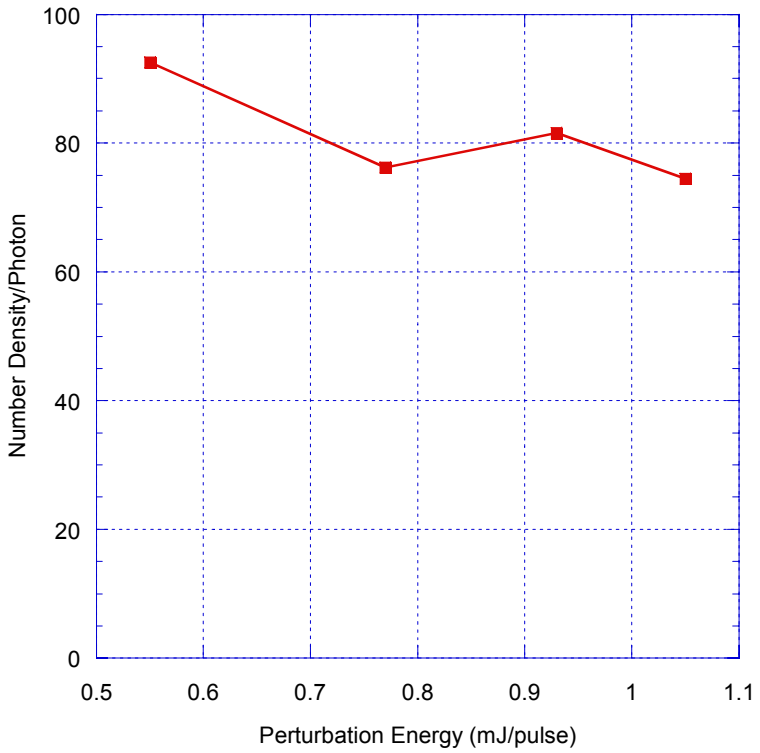

Figure 5-15. Number density change per photon for each pulse energy with 193-nm perturbation of collagen solutions

Table 5-6. Number of photons required to break a peptide bond for each pulse energy with 193-nm perturbation of collagen solutions

Perturbation Energy (mJ/pulse)	**Photons per broken peptide bond**
0.55	24.29
0.77	29.48
0.93	27.54
1.05	30.16

Table 5-7. Average number densities (peptide bonds/ml) and numbers of absorbers (peptide bonds) and standard deviations for each pulse energy and time step with 193-nm perturbation of collagen solutions

Perturbation energy (mJ/pulse)	Cumulative photons	$\frac{d(K_P)}{dn}$ (cm^{-1} per photon)	$\frac{d(K_P)}{dn}$ stand. dev. (cm^{-1} per photon)	Normalized $\frac{1}{N_{Coll}}\frac{d(K_P)}{dn}$ (cm^{-1} per photon per peptide bond)	Normalized $\frac{1}{N_{Coll}}\frac{d(K_P)}{dn}$ stand. dev. (cm^{-1} per photon per peptide bond)
0.55	0.00E+00	0.00E+00	0.00E+00	0.00E+00	0.00E+00
	2.61E+15	-2.11E-14	1.80E-14	-3.01E-33	2.59E-33
	5.22E+15	-1.93E-14	1.85E-14	-2.89E-33	2.79E-33
	7.83E+15	-1.83E-14	1.56E-14	-2.83E-33	2.43E-33
	1.04E+16	-1.70E-14	1.65E-14	-2.75E-33	2.70E-33
	1.31E+16	-2.00E-14	1.41E-14	-3.30E-33	2.35E-33
	1.57E+16	-1.62E-14	1.60E-14	-2.82E-33	2.81E-33
	1.83E+16	-1.62E-14	1.41E-14	-2.91E-33	2.56E-33
	2.09E+16	-1.61E-14	1.53E-14	-2.99E-33	2.87E-33
	2.35E+16	-1.72E-14	1.31E-14	-3.32E-33	2.56E-33
0.77	0.00E+00	0.00E+00	0.00E+00	0.00E+00	0.00E+00
	3.65E+15	-1.84E-14	6.53E-15	-2.15E-33	7.68E-34
	7.31E+15	-1.71E-14	6.87E-15	-2.08E-33	8.41E-34
	1.10E+16	-1.65E-14	6.70E-15	-2.13E-33	8.68E-34
	1.46E+16	-1.58E-14	5.58E-15	-2.11E-33	7.51E-34
	1.83E+16	-1.64E-14	6.14E-15	-2.26E-33	8.50E-34
	2.19E+16	-1.64E-14	6.07E-15	-2.33E-33	8.69E-34
	2.56E+16	-1.43E-14	5.76E-15	-2.12E-33	8.61E-34
	2.92E+16	-1.59E-14	5.60E-15	-2.42E-33	8.60E-34
	3.29E+16	-1.48E-14	5.17E-15	-2.35E-33	8.24E-34
0.93	0.00E+00	0.00E+00	0.00E+00	0.00E+00	0.00E+00
	4.41E+15	-1.52E-14	1.29E-14	-1.85E-33	1.58E-33
	8.83E+15	-1.40E-14	1.41E-14	-1.81E-33	1.83E-33
	1.32E+16	-1.37E-14	1.21E-14	-1.88E-33	1.67E-33
	1.77E+16	-1.30E-14	1.19E-14	-1.88E-33	1.73E-33
	2.21E+16	-1.29E-14	1.07E-14	-1.96E-33	1.64E-33
	2.65E+16	-1.20E-14	1.37E-14	-1.96E-33	2.25E-33
	3.09E+16	-1.25E-14	1.24E-14	-2.10E-33	2.11E-33
	3.53E+16	-1.08E-14	1.29E-14	-1.92E-33	2.31E-33
	3.97E+16	-1.22E-14	1.32E-14	-2.28E-33	2.49E-33
1.05	0.00E+00	0.00E+00	0.00E+00	0.00E+00	0.00E+00
	4.98E+15	-1.77E-14	6.61E-15	-2.10E-33	7.91E-34
	9.97E+15	-1.61E-14	6.38E-15	-2.04E-33	8.17E-34
	1.50E+16	-1.59E-14	6.54E-15	-2.12E-33	8.79E-34
	1.99E+16	-1.61E-14	6.38E-15	-2.25E-33	9.04E-34
	2.49E+16	-1.54E-14	6.10E-15	-2.26E-33	9.08E-34
	2.99E+16	-1.43E-14	5.76E-15	-2.22E-33	9.04E-34
	3.49E+16	-1.35E-14	5.46E-15	-2.20E-33	9.01E-34
	3.99E+16	-1.14E-14	4.96E-15	-2.01E-33	8.83E-34
	4.49E+16	-1.27E-14	5.64E-15	-2.27E-33	1.02E-33

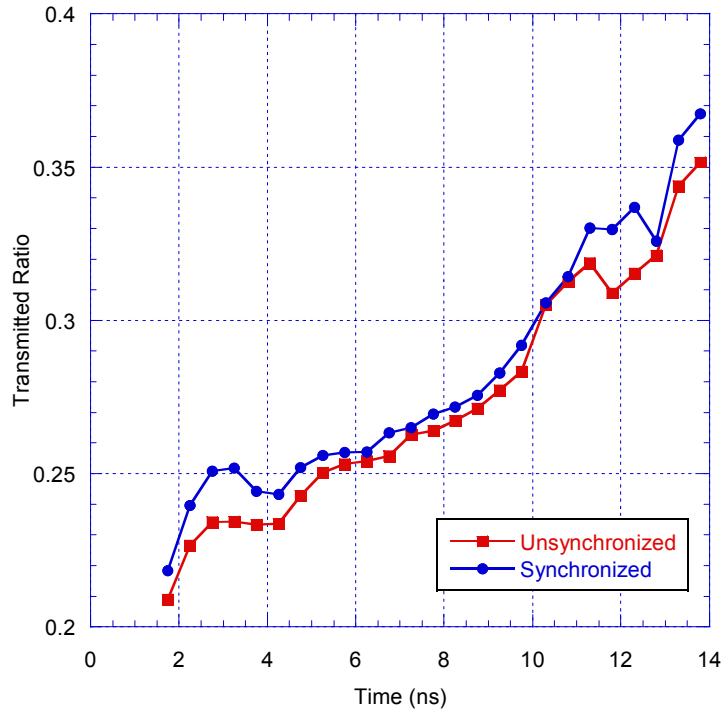

Figure 5-16. Transmission ratio with respect to time during laser pulse

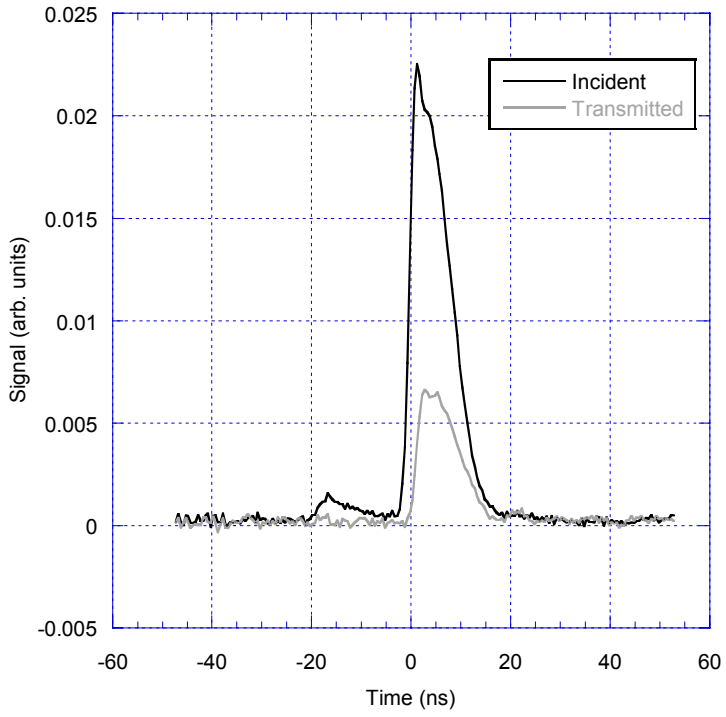

Figure 5-17. Example of oscilloscope output for 355-nm perturbation

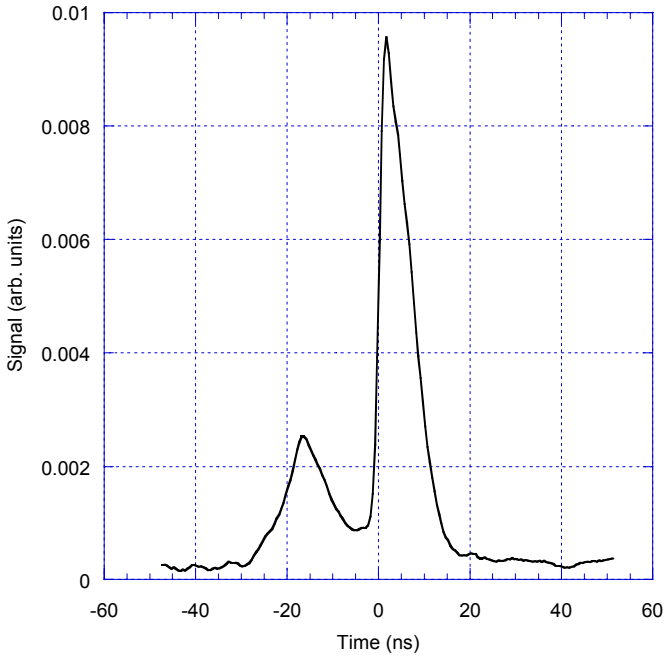

Figure 5-18. Average delay for 355-nm perturbation

Table 5-8. Average absorbance values and standard deviations for each pulse energy and time step with 355-nm perturbation of collagen solutions

Perturbation Energy (mJ/pulse)	Number of pulses	Synchronized Average absorbance	Synchronized Standard deviation absorbance	Un Synchronized Average absorbance	Un Synchronized Standard deviation absorbance
0.48	0	1.033	0.033	1.033	0.033
	11	0.999	0.037	1.042	0.031
	22	0.980	0.033	1.031	0.047
	33	0.985	0.045	1.035	0.045
	44	1.003	0.041	1.017	0.045
	55	0.976	0.042	1.033	0.029
	66	0.973	0.046	1.033	0.043
	77	0.976	0.040	1.031	0.042
	88	0.977	0.046	1.041	0.062
	99	0.954	0.049	1.012	0.033
1.2	0	0.694	0.030	0.694	0.030
	11	0.686	0.036	0.698	0.034
	22	0.686	0.032	0.692	0.034
	33	0.677	0.033	0.692	0.034
	44	0.676	0.035	0.692	0.036
	55	0.674	0.038	0.696	0.037
	66	0.669	0.037	0.676	0.035
	77	0.660	0.040	0.670	0.037
	88	0.660	0.034	0.676	0.035
	99	0.647	0.040	0.664	0.035

Table 5-9. Average extinction coefficients and standard deviations for each pulse energy and time step with 355-nm perturbation of collagen solutions

Perturbation energy (mJ/pulse)	Cumulative photons	Synchronized Average extinction coefficient (cm^{-1})	Synchronized Standard deviation extinction coefficient (cm^{-1})	Un Synchronized Average extinction coefficient (cm^{-1})	Un Synchronized Standard deviation extinction coefficient (cm^{-1})
0.48	0.00E+00	123.245	3.988	123.245	3.988
	4.19E+15	119.172	4.443	124.330	3.749
	8.38E+15	116.868	3.945	122.985	5.649
	1.26E+16	117.528	5.320	123.443	5.322
	1.68E+16	119.709	4.934	121.320	5.399
	2.10E+16	116.426	5.016	123.213	3.483
	2.51E+16	116.043	5.449	123.225	5.165
	2.93E+16	116.399	4.794	123.056	5.005
	3.35E+16	116.549	5.491	124.231	7.423
	3.77E+16	113.769	5.848	120.754	3.879
1.2	0.00E+00	82.746	3.582	82.746	3.582
	1.05E+16	81.844	4.349	83.238	4.058
	2.10E+16	81.863	3.813	82.560	4.037
	3.14E+16	80.805	3.969	82.582	4.068
	4.19E+16	80.622	4.208	82.503	4.311
	5.24E+16	80.419	4.573	82.980	4.365
	6.29E+16	79.760	4.443	80.602	4.154
	7.33E+16	78.719	4.796	79.959	4.362
	8.38E+16	78.708	4.100	80.630	4.192
	9.43E+16	77.193	4.776	79.186	4.205

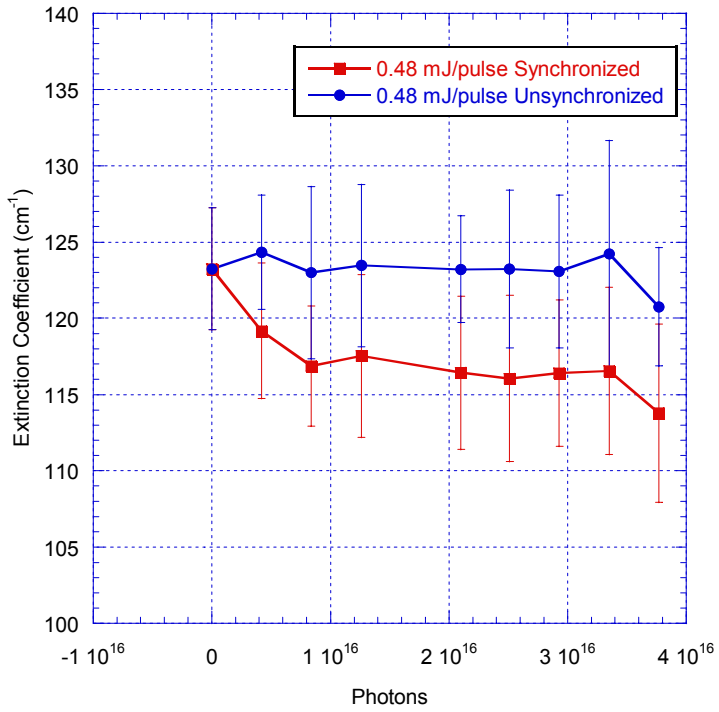

Figure 5-19. Average extinction coefficient (σN) and standard deviations for 0.48mJ/pulse energy and time step with 355-nm perturbation of collagen solutions

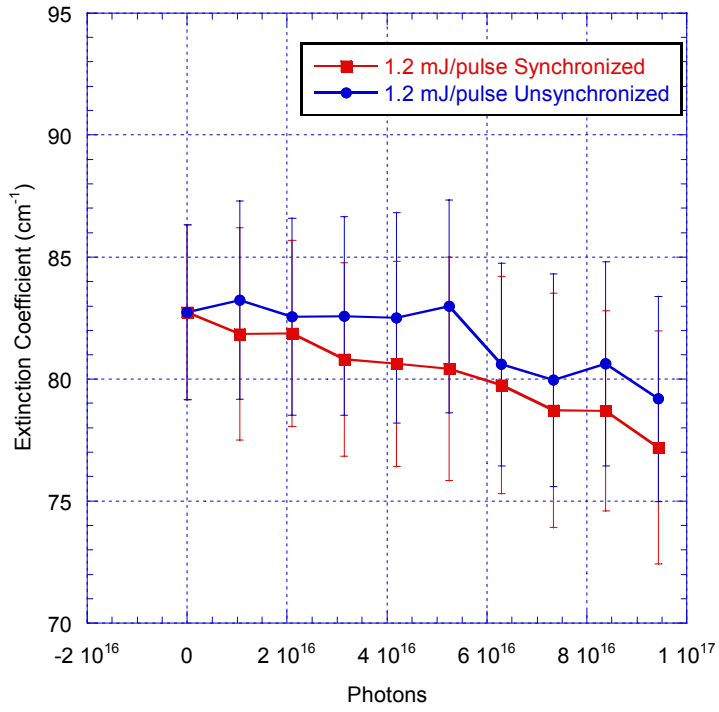

Figure 5-20. Average extinction coefficient (σN) and standard deviations for 1.2 mJ/pulse energy and time step with 355-nm perturbation of collagen solutions

CHAPTER 6
MASS SPECTROSCOPY

Mass spectrometry of the ablation plumes is an area of research in photoablation of corneas that is ripe for re-evaluation. Better technology, including an advanced surgical laser with a clean energy distribution and a new mass spectrometry system shall allow for a better experimental setup. Knowledge of the plume contents may lead to a better understanding of the process as a whole, notably in conjunction with the collagen and amino acid studies.

Experimental Setup and Methods

Mass spectrometry was performed with Hiden Analytical's HPR20-QIC atmospheric gas analysis system. This quadrupole mass spectrometer is compact, and has a "sniffer" probe that allows direct sampling of the ablation plume from the corneal surface at atmospheric pressure. This machine has a sensitivity of about 15 ppb and a mass detection range of up to 200 amu, and was operated at 3×10^{-5} torr. Bovine eyes were harvested as described in Chapter 2 above, and the same delivery system was used to generate ablations of the corneas, as shown in Figure 6-1. The probe of the portable mass spectrometer was mounted approximately 2 mm above the corneal surface at the edge of the 6-mm ablation zone. Treatments of 9 diopters at 100 Hz were applied to the bovine corneas while the mass spectrometer probe sampled the air, bringing the sample to the mass spectrometer using a heated quartz capillary tube. Two ablations were applied for each cornea. For a range of 1 to 100 amu, 7 scans from were recorded with 0.25-amu resolution for each of 12 ablations (6 eyes). For a range of 101 to 150 amu, 7 scans were recorded with 0.25-resolution for each of 4 ablations (2 eyes). Background scans were also recorded from the same location in order to determine the baseline contribution from the local environment. Background spectra were recorded with the laser operating in order to include any

effects of laser-air interaction, such as ozone formation. A set of 7 background scans was taken for each ablation.

Mass Spectrometry Results

The background scans are presented first. The average background for all scans and all eyes over the entire mass range (1–150 amu) studied is shown in Figure 6-2. It is clear from the plot that the components of the environmental air are below 45 amu. Thusly, Figure 6-3 focuses on that mass range. In this figure, all peaks have been labeled with their corresponding molecular component. Any additional components relative to this background signal may indicate ablation products.

Just as with the background scans, the signals obtained during corneal ablations from all scans and all eyes were averaged together. The results are shown in Figure 6-4. There are three peaks of interest in this figure, at 17, 18 and 42 amu. The peaks at 17 and 18 are OH and H_2O, respectively; their increase is due to water released as an ablation product. This is consistent with previous results which indicate the presence of water vapor in the ablation products [68]. The third peak at 42 amu, as shown in Figure 6-5, is unique to the ablation spectra; therefore, a candidate to originate from an ablation product.

An analysis of the collagen structure (Figure 6-6) shows one possibility for the origin of the 42-amu component: a fragment of glycine containing 2 carbons, 2 hydrogens and 1 oxygen unit. This unit is depicted in Figure 6-7. As the peptide bond is the expected primary chromophore, a NH grouping at 29 amu is expected to be present with this fragment. An additional contribution to the 29 amu signal is not present in the ablation series as compared to the background series. However, the expected contribution due to a NH ablation product is very small relative to the contribution from the surrounding air.

Mass Spectrometry Summary

Mass spectroscopy of ablation plumes has shown a large amount of water present in the ablation products, as well as a possible 42-amu fragment of glycine containing 2 carbon units, 2 hydrogen units and one oxygen unit. This data is consistent with the findings of Hahn *et al* in 2004, which found that water vapor is the predominant constituent in the ablation plume. The 42-amu fragment is consistent with peptide bonds being the primary chromophore, as the glycine-proline peptide bond must be broken in the creation of this fragment. This fragment was not found in previous mass spectroscopic analyses of corneal photoablation [74, 75].

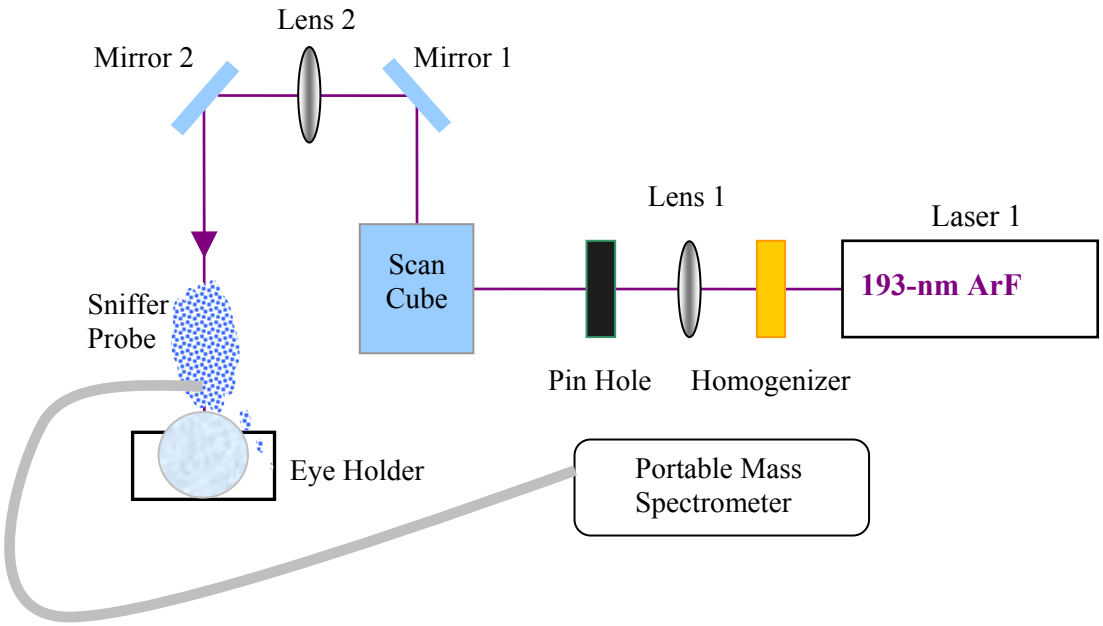

Figure 6-1. Experimental setup for mass spectrometry

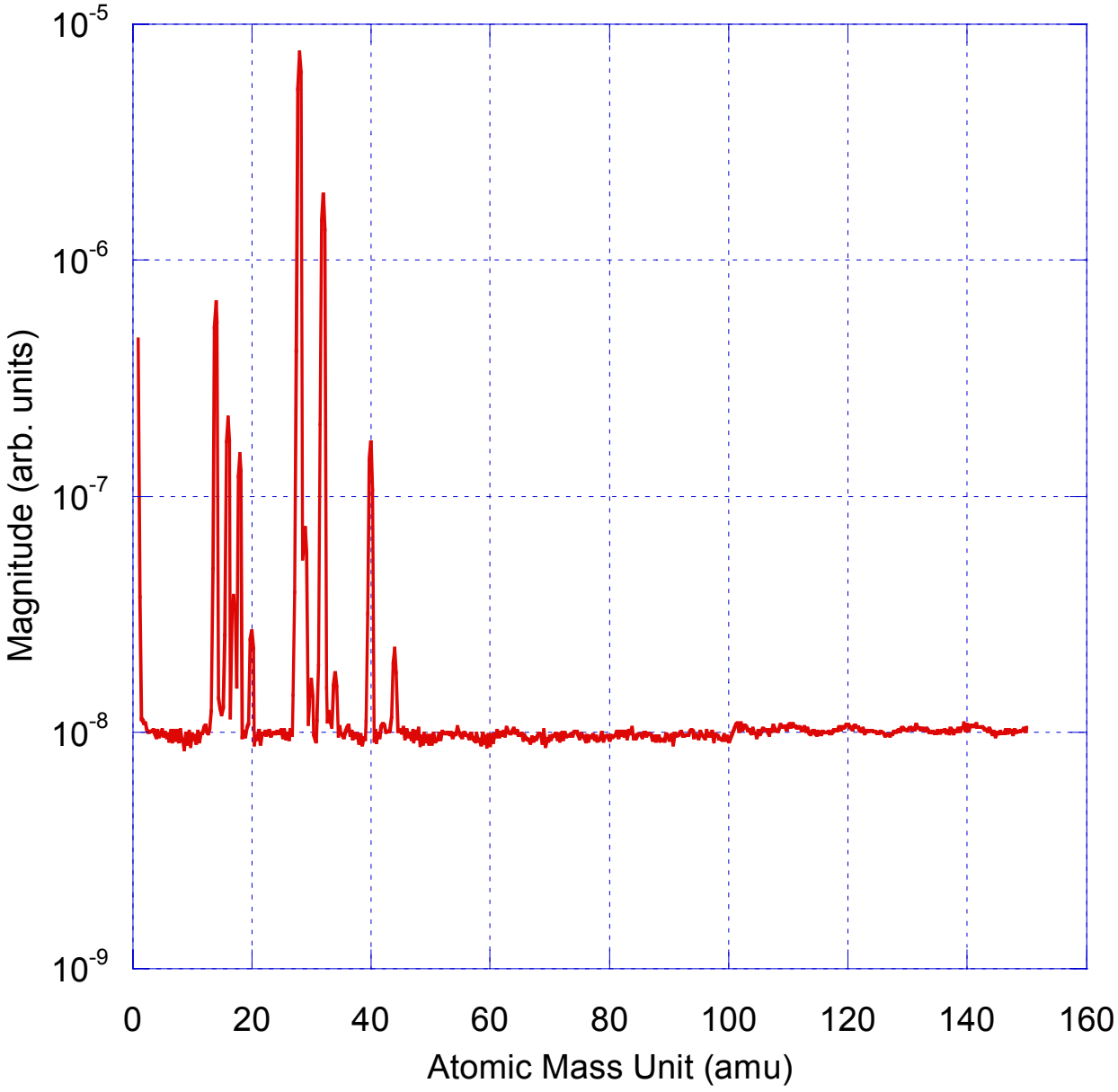

Figure 6-2. Average background spectra over entire analyzed range

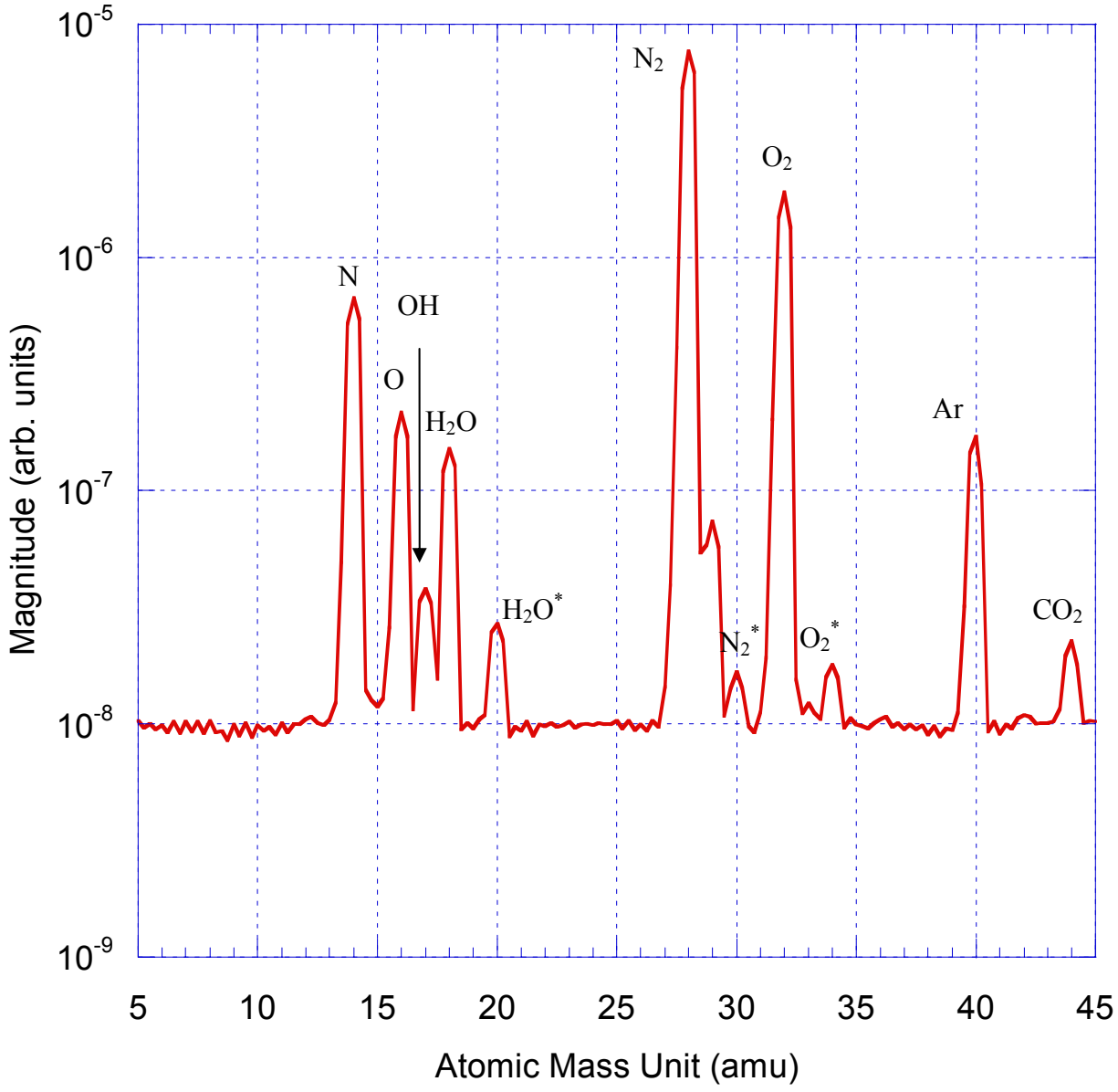

Figure 6-3. Average background spectra over range of activity

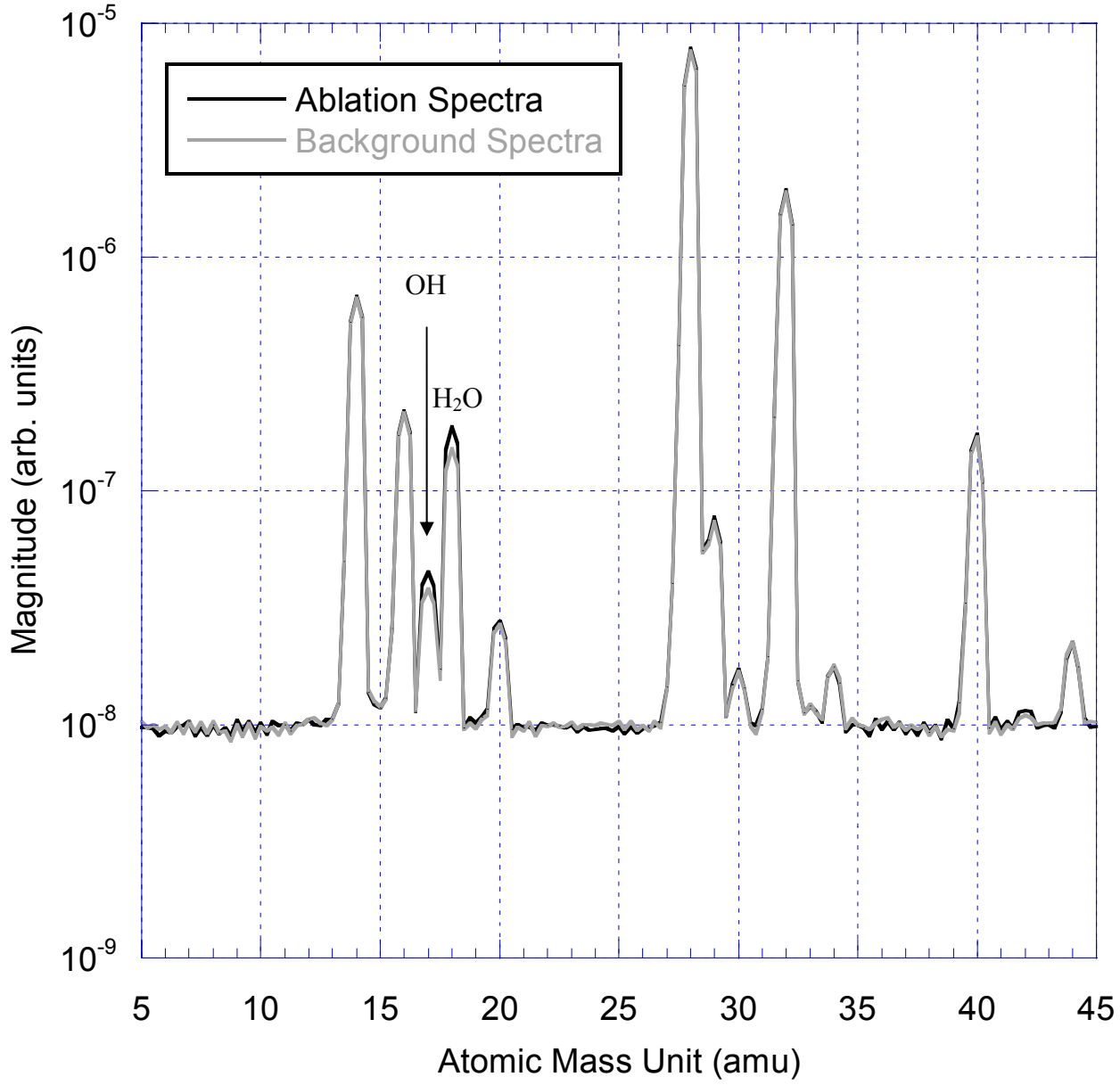

Figure 6-4. Average background and ablation spectra

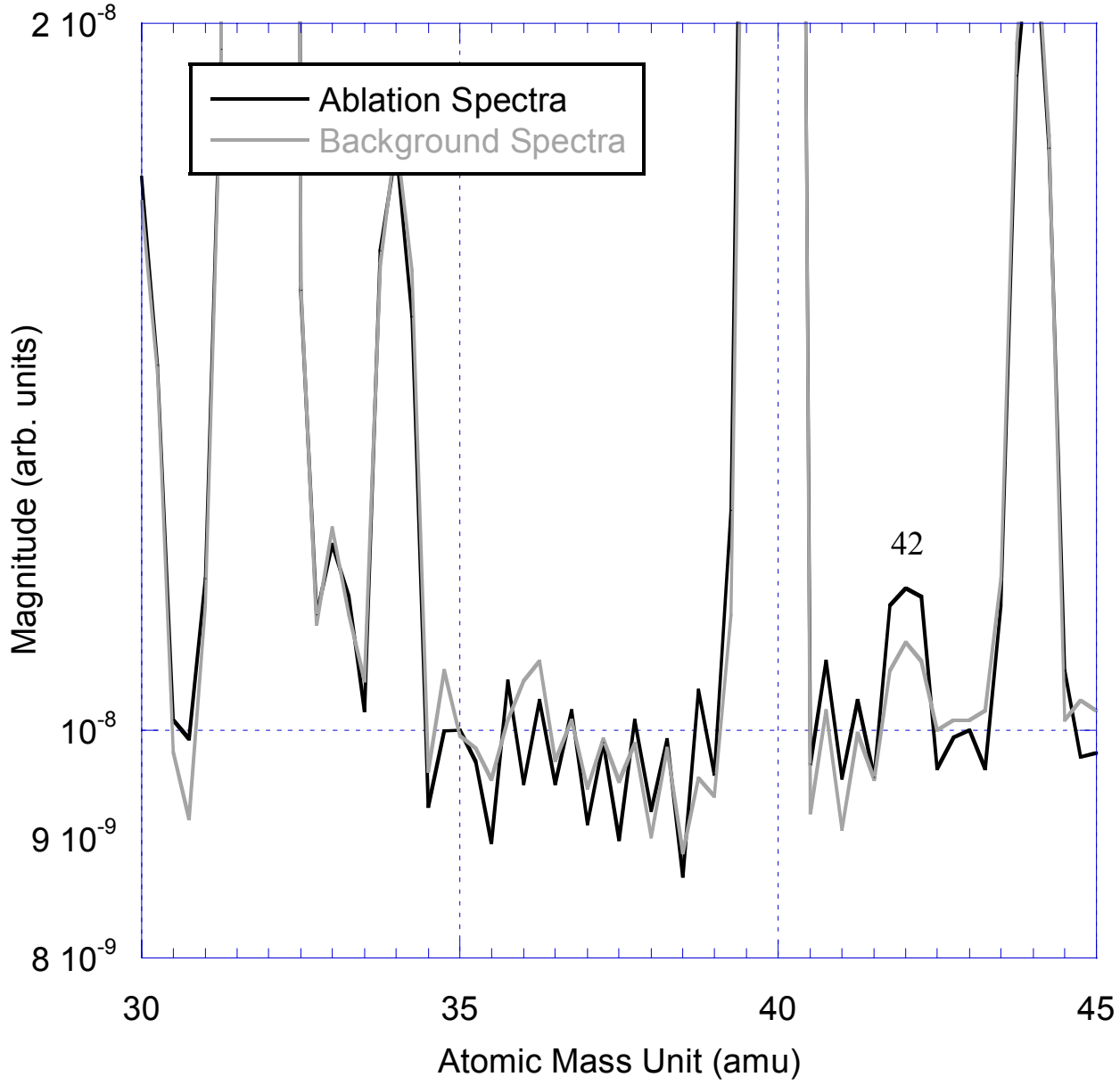

Figure 6-5. Average background and ablation spectra focused around 42 amu peak

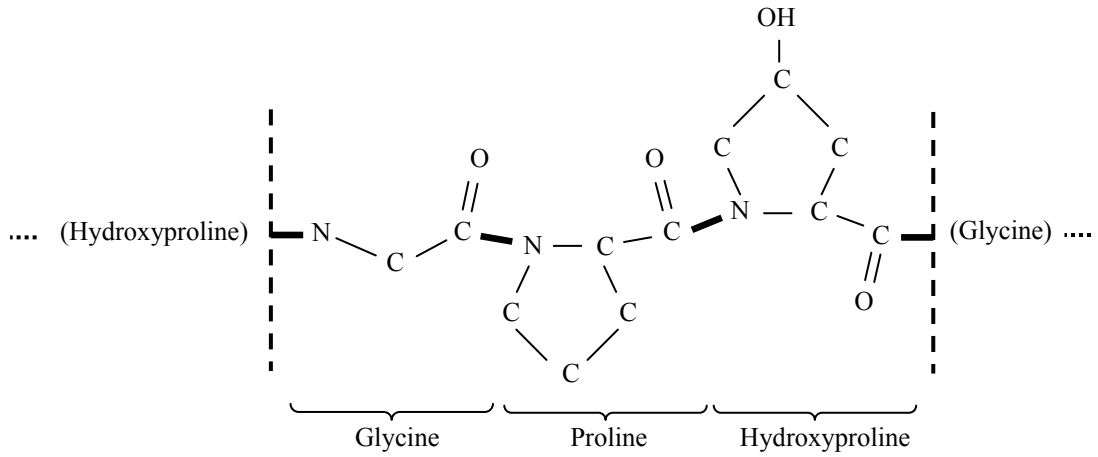

Figure 6-6. Simplified collagen structure of the human cornea taken from reference 8

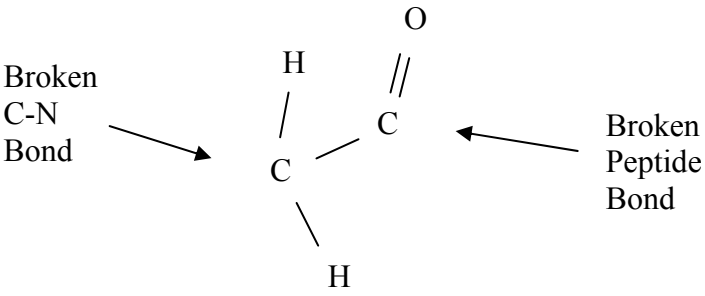

Figure 6-7. Structure of the 42-amu molecular fragment

CHAPTER 7
CONCLUSIONS AND FUTURE WORK

This chapter presents the important conclusions of the preceding chapters and places the results of each experiment in context with each other. Additionally, recommendations for future work are given.

Conclusions

The current experiments have examined the potential effects of laser repetition rate on corneal ablation over a range of clinically relevant conditions. Experiments have assessed a comprehensive range of parameters, including plume dynamics, corneal ablation profiles, and high-resolution microscopy of collagen structure, which in aggregate lead to the conclusion that no observable effects of laser repetition rate are present for the comparison of 60 and 400 Hz:

- The plume dynamics studies (imaging and transmission) indicate that the bulk of the plume evolves away from the corneal surface on a time scale of several ms, and is largely gone by 2.5 ms (the pulse-to-pulse time spacing for 400 Hz ablation. Thus attenuation of the laser pulse by the previous plume is negligible up to about 400 Hz, as confirmed by the ablation profile study.

- The ablation rate in bovine corneas was calculated to be between 0.95 and 0.98 μm/pulse for a total pulse energy of 2.7 mJ and a Gaussian beam profile.

- The ablation rate of PMMA was calculated to be approximately 0.18 μm/pulse. The ablation threshold, 25 mJ/cm^2, was determined using a unique method of comparing the edge of the ablation profile with the beam fluence profile.

- The ablation rate in bovine corneas was constant for 60 and 400 Hz. The shapes and the depths of the ablation profiles were likewise consistent.

- No differential tissue damage was noted in microscopy (visible, SEM, TEM) images of 400 Hz as compared to 60 Hz, including no disorganization, collagen size changes or coagulation. The numbers of fibrils in the TEM images were counted and no statistical difference in collagen fibril density near the ablation surface between 60 and 400 Hz was observed.

Additional conclusions may also be drawn from the set of experiments with regard to the implementation of the laser ablation system:

- The addition of a small vacuum (suction) to the corneal surface, which approximated the plume evacuator used by surgeons, did not alter the ablation profiles obtained from the excimer system.

- Reversing the algorithm of the excimer laser showed no alteration to the ablation profiles achieved on PMMA. While a trend was noted of over-ablation by the reversed pattern was seen, this trend was dominated by large standard deviations, such that no statistical difference was documented.

The sub-ablative 193-nm and 355-nm perturbations yielded insight into 193-nm and 355-nm excitation of collagen and amino acids. These perturbations are also discussed in the context of photoablation mechanism.

- Amino acid solutions were not permanently altered by 193-nm sub-ablative energies.

- An average of 28 photons at 193 nm was required to break a single peptide bond.

- Perturbations of collagen solutions by 355-nm resulted in only 4.5% of the extinction coefficient obtained by 193-nm perturbations, resulting in 508 bonds being required to break a single peptide bond.

- A dynamic photobleaching occurs at both 193-nm and 355-nm perturbations. This effect is greater at 193 nm than at 355 nm. It is also present for both amino acid and collagen solutions. The effect resolves itself by a time scale of tens of seconds and does not have a long-term affect on the solutions.

- The source of the dynamic reduction is most likely photobleaching of the sample, wherein the sample becomes temporarily excited by the incident photons to an electronic state with a reduced absorption coefficient. This excitation relaxes over time leaving no permanent chemical change in the solution.

- Recalling that the difference between the collagen and amino acid solutions is the presence of peptide bonds, the permanent change induced in the collagen samples must be due to scission of the peptide bonds in the solution. This confirms that the peptide bond is the primary chromophore in the case of sub-ablative perturbations in the range of 0.55 to 1.2 mJ/pulse (9 to 21 mJ/cm^2).

- It was previously supposed that at sub-ablative conditions only thermal mechanisms were present. This study contradicts this belief, as photothermal mechanisms are definitely existent.

Mass spectrometry experiments were used to analyze the ablation products present in the ablation plume. The main constituent present was found to be water, with a small amount of a 42-amu fragment of possibly glycine containing 2 carbon units, 2 hydrogen units and one oxygen unit.

In summary, investigation of the relative effects of excimer laser repetition rate on the overall corneal ablation processes (i.e. plume dynamics, ablation rates and corneal pathology) revealed no measurable difference under conditions typical of refractive procedures. This study suggests that increases in ArF laser repetition rates for clinical applications (up to ~400 Hz) appear feasible, and therefore justify the pursuit of additional clinical studies.

The exact mechanism of photoablation remains a topic of research [5, 81]. Several interesting findings in the current study are relevant and provide insight as to the overall process of excimer laser ablation of corneal tissue, namely the TEM analysis and the transmission experiments. First the finding of a persistent, diffuse component of the ablation plume as measured by 193-nm absorption, suggests molecular fragments from the ablation process itself. This finding is supportive of a photochemical mechanism, in which amino acid fragments are created within the tissue matrix and subsequently ejected with the plume. Secondly the lack of any noticeable damage or perturbation to the collagen fibrils immediately underlying the ablation zone, as seen in the TEM histology experiments, speaks to the precision of excimer laser tissue etching. The lack of any indication of thermal damage in the microscopy images indicates a photochemical process. Together, such results are consistent with the photochemical model of ArF laser ablation of corneal stromal tissue, in which the high excimer laser photon energy (6.4 eV) can directly cleave protein strands (i.e. peptide bonds), forming transient species, in a very dynamic laser-tissue interaction process [14].

Ishihara and co-workers have studied the surface temperature of cornea during ablation, and found that the peak surface temperature increases with laser fluence. At 180 mJ/cm^2, they reported a value of 240^{o}C surface temperature, and at fluences near 300 mJ/cm^2, the temperature is as high as approximately 325^{o}C. These results suggest a photothermal component to the ablation mechanism. However, additional measurement by this group determined that the increase in temperature decreases rapidly on a time scale of a few hundred microseconds for 193-nm irradiation. This quick dissipation of surface temperature supports the current findings of no differential thermal damage, as the pulse-pulse time scale is on the order of several ms [66, 82]. Thusly, the thermal energy is expected to dissipate on a time scale much less than that of the laser repetition rate. Ishihara and co-workers also found that the surface temperature relaxes more quickly for 193-nm irradiation as compared to 248-nm irradiation noting that a thermal component of ablation is considered to increase with increasing wavelength, notably so in the infrared spectral region [82]. Overall, the reduced surface temperature observed with 193-nm irradiation seems to indicate a mechanism that is less reliant on thermal excitation.

Additional insight into the present findings may be gained by contrasting the results with a previous study of laser repetition rate effects of CO_2 lasers on tissue. The ablation mechanism of CO_2 laser-tissue interaction is considered a purely thermal process. For this type of ablation, thermal damage and the resulting ablation rate have been found to significantly increase with laser repetition rate [83, 84]. This is in stark contrast to the results of the current study, which do not indicate any differential tissue damage or a change in ablation depth with repetition rate. This difference may be explained in the context of thermal relaxation times. This time is on the order of tens of ms for the case of CO_2 ablation and on the order of tens of microseconds for ArF ablation. Thus, the critical laser repetition rate for 193-nm excimer laser ablation is in the range

of tens of kilohertz, much greater than the range examined in the current study, while the CO_2 laser ablation has a critical laser repetition rate of approximately 20 Hz. This supports the findings of no differential thermal tissue damage [84]. Although the exact partitioning between photochemical and photothermal influences remains unknown, the role of the photothermal component does not have an altering influence as the laser repetition rate is increased to 400 Hz. The current findings are consistent with a primarily photochemical process with the 193-nm excimer, which is consistent with the literature [5].

Future Work

There are several additional experiments that may be performed in order to further shed light on the mechanisms of laser-tissue interaction. They are briefly summarized in the following:

- Repeat the mass spectrometry experiments utilizing a more sensitive instrument in order to uncover further peaks due to molecular fragments of amino acid chains.
- Repeat the sub-ablative experiments on bipeptide solutions. Bipeptides are combinations of only two amino acids. Performing these experiments on glycine-proline, glycine-hydroxyproline and proline-hydroxyproline solutions may distinguish which peptide bonds are more likely to break during sub-ablative perturbations.
- Repeat the sub-ablative experiments with ablative energies. The results could be compared with those found here for sub-ablative perturbations in order to glean any information on the differences in mechanisms between the two. The experimental setup may need modification, in order to ablate the solution sample and not the sample cell.
- Repeat the sub-ablative perturbation experiments concurrent with fluorescence measurements in order to examine fluorescence changes that may occur due to the so-called “photobleaching” effect. This set of experiments may lead to additional insight into the dynamic response of solution samples to incident energy.
- Repeat the sub-ablative experiments with a femtosecond laser. The ultra-short pulses result in nonlinear (multiphoton) absorption, in contrast to the longer (nanosecond) pulses employed in this work [85]. The use of a femtosecond source would allow the study of the resulting nonlinear effects.

- It has been shown in Chapter 5 that even at low 193-nm fluences, bonds are broken within collagen. At a threshold fluence, the stress buildup due to these broken bonds results in ejection of material from the substrate. Solid mechanics modeling may be performed of the stresses induced by volumetric expansion as a result of broken bonds in order to determine the critical volumetric stress required for ablation to occur.

APPENDIX A
MATLAB EDGE FINDER

```
function find_eye_edge_midpoint

%prompt= 'Enter number of standard deviations';
prompt= 'Enter percentage above dark mean';
numlines=1;
defaultanswer= 0.5;
standDevs = inputdlg(prompt,'Input required:',1,{num2str(defaultanswer)});
standDevs = str2num(standDevs{1});

saveTo = questdlg...
    ('Would you like to add new eye data to an existing file?');

if strcmp(saveTo, 'Yes');
    [saveFile,savePath] = uigetfile('*.mat', 'Select data file');
    load(fullfile(savePath, saveFile))
    fileList = eyeData.fileList;
%    originalImage = eyeData.originalImage;
%    croppedImage = eyeData.croppedImage;
    cropRegion = eyeData.cropRegion;
    edgeList = eyeData.edgeLocation;
elseif strcmp(saveTo, 'No')
    [saveFile, savePath] = uiputfile('*.mat', 'Save eye edge data to:');
    fileList = cell(0);
end

if ~exist('saveFile') | isempty(saveFile)
    return
end

theSwitch = 'Yes';

while strcmp(theSwitch, 'Yes')

    [fileName,pathName] = uigetfile('*.asc', 'Select file to process');
    if isempty(fileName)
        break
    end

    thisFile = fullfile(pathName, fileName);

    I = strmatch(thisFile, fileList, 'exact');

    if isempty(fileList)
        I = 1;
    elseif ~isempty(I)
        overWrite = questdlg...
            ('File has already been processed. Re-do?', 'Yes', 'No');
        if strcmp(overWrite, 'No')
            continue
        end
    else
        I = length(fileList) + 1;
    end
```

```
    fileList{I} = thisFile;

    [thisImage] = dlmread(thisFile, '\t');
    thisImage = thisImage';
    rows = 1:size(thisImage,1);
    cols = 1:size(thisImage,2);

%    originalImage{I} = thisImage;

    figure(1)
    imagesc(cols, rows, thisImage)
    set(gca, 'ydir', 'normal')
    set(gcf, 'name', [fileName ' - Original'])

    isOK = 'No';

    while strcmp(isOK, 'No')
        figure(1)
        fprintf('Select the crop region.\n')
        p = ginput(2);
        cutRows = rows(floor(min(p(:,2))):ceil(max(p(:,2))));
        cutImage = thisImage(cutRows,:);

        figure(4)
        imagesc(cols,cutRows, cutImage)
        set(gca, 'ydir', 'normal')
        set(gcf, 'name', [fileName ' - Cropped'])

        isOK = questdlg({'Is this crop acceptable?'; ...
            '(Note:  Program needs 50 pixels of eye to average)'}, ...
            'Input required:', 'Yes', 'No', 'Yes');
    end
%    croppedImage{I} = cutImage;
    cropRegion{I} = cutRows;

    doneYet = 'No';

    while strcmp(doneYet, 'No')
        for index = 1:size(cutImage,2)
            theMean = nanmean(cutImage(1:50,index));
            theMean2 = nanmean(cutImage(end-50:end,index));
%            theSTD = nanstd(cutImage(1:50,index));
%            cutOff = theMean + standDevs*theSTD;
            cutOff = standDevs*(theMean2-theMean)+theMean;
            overCut = find(cutImage(:,index) > cutOff);
            diffs = diff(overCut);
            firstGoods = find(diffs == 1);
            if firstGoods(2) == (firstGoods(1)+1)
                edgeLocation(index) = ...
                    mean(cutRows(overCut(firstGoods(1):firstGoods(1)+1)));
            else
                edgeLocation(index) = ...
                    mean(cutRows(overCut(firstGoods(2):firstGoods(2)+1)));
            end
        end
```

```
        figure(4)
        hold on
        l = plot(cols, edgeLocation, 'k');

        doneYet = questdlg('Is this edge acceptable?', 'Input required:', ...
            'Yes', 'No', 'Yes');

        if strcmp(doneYet, 'No')

            prompt='Enter number of standard deviations';
            numlines=1;
            defaultanswer= 4;
            standDevs = inputdlg(prompt,'Input
required:',1,{num2str(standDevs)});
            standDevs = str2num(standDevs{1});

            delete(l)
        end
    end

    edgeList{I} = edgeLocation;

    eyeData.fileList = fileList;
%    eyeData.originalImage = originalImage;
%    eyeData.croppedImage = croppedImage;
    eyeData.cropRegion = cropRegion;
    eyeData.edgeLocation = edgeList;

    save(fullfile(savePath,saveFile), 'eyeData')
    close all

    theSwitch = questdlg('Would you like to do another file?', ...
        'Input required:', 'Yes', 'No', 'Yes');
end

save(fullfile(savePath,saveFile), 'eyeData')
clc
```

APPENDIX B
MATLAB RESULTS COMPILER

```
function compile_results

[dataFile, dataPath] = uigetfile('*.mat', 'Select data file');

if isempty(dataFile)
    return
end

load(fullfile(dataPath, dataFile))

fileList = eyeData.fileList;

for index = 1:length(fileList)
    [junk, thisFile] = fileparts(fileList{index});
    thisFile = lower(thisFile);
    %findEye = findstr(thisFile, 'eye');
    findSpace = findstr(thisFile, ' ');
    eyeNumber(index) = str2num(thisFile(findSpace(1)+1:findSpace(2)-1));

    findPre = findstr(thisFile, 'pre');

    if isempty(findPre)
        findPost = findstr(thisFile, 'post');
        %runNumber(index) = str2num(thisFile(findPost+4:end));;
        runNumber = 1;
        timeNumber(index) = 2;
    else
        timeNumber(index) = 1;
        %runNumber(index) = str2num(thisFile(findPre+3:end));
        runNumber = 1;
    end

    edgeData(:,index) = eyeData.edgeLocation{index}';
end

eyeList = unique(eyeNumber);

for eyeIndex = 1:length(eyeList)
    thisEyePres = find((eyeNumber == eyeList(eyeIndex)) & ...
        (timeNumber == 1));
    preAll = edgeData(:,thisEyePres);

    fprintf(['For eye number ' num2str(eyeList(eyeIndex)) ' there are ' ...
        num2str(size(preAll,2)) ' "pre" samples.\n']);

    preMean(:,eyeIndex) = preAll;
    %preStd(:,eyeIndex) = (std(preAll'))';

    thisEyePosts = find((eyeNumber == eyeList(eyeIndex)) & ...
        (timeNumber == 2));

    postAll = edgeData(:,thisEyePosts);
```

```
    fprintf(['For eye number ' num2str(eyeList(eyeIndex)) ' there are ' ...
        num2str(size(postAll,2)) ' "post" samples.\n']);

    postMean(:,eyeIndex) = postAll;
    %postStd(:,eyeIndex) = (std(postAll'))';
end

for index = 1:length(eyeList);
    index
    pPre(:,index) = (polyfit([1:1024]', preMean(:,index), 2))';
    %pPost(:,index) = (polyfit([1:1024]', postMean(:,index), 2))';
    fitPre(:,index) = polyval(pPre(:,index), [1:1024]');
    %fitPost(:,index) = polyval(pPost(:,index), [1:1024]');

    theDiff(:,index) = fitPre(:,index) - postMean(:,index);
    diffP(:,index) = (polyfit([1:1024]', theDiff(:,index), 2))';
    diffFit(:,index) = polyval(diffP(:,index), [1:1024]');

    rawDiff(:,index) = preMean(:,index) - postMean(:,index);

    SST = sum((preMean(:,index) - mean(preMean(:,index))).^2);
    SSR = sum((fitPre(:,index) - mean(preMean(:,index))).^2);
    RsquarePre(index) = SSR./SST;

    SST = sum(sum((theDiff(:,index) - mean(theDiff(:,index))).^2));
    SSR = sum(sum((diffFit(:,index) - mean(theDiff(:,index))).^2));
    RsquareDiff(index) = SSR./SST;
end

[dataFile2, dataPath2] = ...
    uiputfile('*.txt', 'Select output file: Pixel Fit Values');

fID = fopen(fullfile(dataPath2, dataFile2), 'w');
fprintf(fID, 'Pixel Fit Values\n');
titleVector = ['\t'];
fprintf(fID, 'Pixel\t');
for index = 1:length(eyeList)
    fprintf(fID, ['Eye ' num2str(eyeList(index)) '\t\t\t\t']);
    titleVector = [titleVector 'Pre\tPost\tRaw Diff.\tPre Fit/Post Raw
Diff.\t'];
end
fprintf(fID, '\n');
fprintf(fID, [titleVector '\n']);
for index = 1:1024;
    fprintf(fID, [num2str(index) '\t']);
    for index2 = 1:length(eyeList)
        fprintf(fID, [num2str(preMean(index,index2)) '\t' ...
            num2str(postMean(index,index2)) '\t' ...
            num2str(rawDiff(index,index2)) '\t' ...
            num2str(theDiff(index,index2)) '\t']);
    end
    fprintf(fID, '\n');
end
fclose('all')
```

```
[dataFile3, dataPath3] = ...
    uiputfile('*.txt', 'Select output file: Parabolic Fit Parameters');
fID = fopen(fullfile(dataPath3, dataFile3), 'w');
fprintf(fID, 'Parabolic Fit Parameters\n');
fprintf(fID, 'y = a*x^2 + b*x + c\n');
fprintf(fID, 'Eye\tPre\n');
fprintf(fID, '\ta\tb\tc\tRsquare\n');
for index = 1:length(eyeList)
    fprintf(fID, [num2str(eyeList(index)) '\t' ...
        num2str(pPre(1,index)) '\t' num2str(pPre(2,index)) '\t' ...
        num2str(pPre(3,index)) '\t' num2str(RsquarePre(index)) '\n']);
end
fclose('all')
```

APPENDIX C
EQUIPMENT LISTING

This appendix includes the manufacturers and model numbers for essential components implemented in the experiments outlined in Chapters 2–6.

Table C-1: Manufacturers and Model numbers of experimental components

Component	**Manufacturer**	**Model**
ArF Excimer Laser	TuiLaser	FTLasikStar
ArF Excimer Laser	GAM Laser, Inc.	EX5
Nd:YAG **L**aser	Big Sky Technologies, Inc.	Ultra UL120111
Scan Cube	Scanlab	38966
Phototube Detectors	Hamamatsu Photonics	R1193U-02
L2 Focusing Lens	Lambda Research Optics, Inc.	24459
193-nm Interference Filter	Melles Griot	03FIU 101
193-nm Beam Homogenizer	MEMS Optical	Custom Part
Delay Generators	Stanford Research Systems, Inc.	DG535
355-nm Edge Filter	Semrock	Razoredge LP01-355RU-25
Digital Oscilloscope	LeCroy	Waverunner LT372
iCCD Camera	Andor Technology	DH734-25F-03
iCCD Camera	Princeton Instruments, Inc.	7397-0072
Mass Spectrometer	Hiden Analytical Ltd.	HPR 20
White-Light Interferometer	Zygo	NewView

LIST OF REFERENCES

1. LASIK Surgery News. *LASIK by the Numbers*. [updated 3 July 2008; cited 24 July 2008]. Available from http://lasiksurgerynews.com/news/eye-vision-statistics.shtml.

2. S. D. Klyce and R. W. Beuerman, "Structure and function of the cornea," in *The Cornea* (Butterworth-Heinemann, Boston, 1998).

3. M. H. Niemz, *Laser-Tissue Interactions* (Springer, New York, 1996).

4. E. W. Kornmehl, R. K. Maloney, and J. M. Davidorf, *LASIK: A Guide to Laser Vision Correction* (Addicus Books, Nebraska, 2006).

5. A. Vogel and V. Venugopalan, "Mechanisms of pulsed laser ablation of biological tissues," Chem. Rev. **103**, 577–644 (2003).

6. S. Lerman, "The cornea," in *Radiant Energy and the Eye* (Macmillan, New York, 1980).

7. C. Boote, S. Dennis, R. H. Newton, H. Puri, and K. M. Meek, "Collagen fibrils appear more closely packed in the prepupillary cornea: Optical and biomechanical implications," Invest. Ophth. Vis. Sci. **44**, 2941–2948 (2003).

8. B. T. Fisher and D. W. Hahn, "Measurement of small-signal absorption cross section of collagen for 193-nm excimer laser light and the role of collagen in tissue ablation," Appl. Optics **43**, 5443–5451 (2004).

9. J. Pearce and S. Thomsen, "Rate process analysis of thermal damage," in *Optical-Thermal Response of Laser-Irradiated Tissue* (Plenum Press, New York, 1995).

10. V. Venugopalan, N. S. Nishioka, and B. B. Mikic, "The effect of laser parameters on the zone of thermal injury produced by laser ablation of biological tissue," J. Biomech. Eng. – T ASME **116**, 62–70 (1994).

11. M. B. McDonald and D. Chitkara, "Principles of excimer laser photoablation" in *The Cornea* (Butterworth-Heinemann, Boston, 1998).

12. E. E. Manche, J. D. Carr, W. W. Haw, and P. S. Hersh, "Excimer laser refractive surgery," Western J. Med. **169**, 30–38 (1998).

13. R. A. Eiferman, K. P. O'Neill, D. R. Forgey, and Y. D. Cook, "Excimer laser photorefractive keratectomy for myopia: Six-month results," Refract. Corneal Surg. **7**, 344–347 (1991).

14. B. T. Fisher and D. W. Hahn, "Development and numerical solution of a mechanistic model for corneal tissue ablation with the 193 nm argon fluoride excimer laser," J. Opt. Soc. Am. A. **24**, 265–277 (2007).

15. C. A. Puliafito, K. Wong, and R. F. Steinert, "Quantitative and ultrastructural studies of excimer laser ablation of the cornea at 193 and 248 nanometers," Lasers Surg. Med. **7**, 155–159 (1987).

16. D. S. Aron-Rosa, J. L. Boulnoy, F. Carre, J. Delacour, M. Gross, M. Lacour, J. C. Olivo, and J. C. Timsit, "Excimer laser surgery of the cornea: Qualitative and quantitative aspects of photoablation according to the energy density," J. Cataract Refr. Surg. **12**, 27–33 (1986).

17. M. W. Berns, L. Chao, A. W. Giebel, L. H. Liaw, J. Andrews, and B. VerSteeg, "Human corneal ablation threshold using the 193-nm ArF excimer laser," Invest. Ophth. Vis. Sci. **40**, 826–830 (1999).

18. M. Campos, X. W. Wang, L. Hertzog, M. Lee, T. Clapham, S. L. Trokel, and P. J. McDonnell, "Ablation rates and surface ultrastructure of 193 nm excimer laser keratectomies," Invest. Ophth. Vis. Sci. **34**, 2493–2500 (1993).

19. F. E. Fantes and G. O. Waring, "Effect of excimer laser radiant exposure on uniformity of ablated corneal surface," Lasers Surg. Med. **9**, 533–542 (1989).

20. H. J. Huebscher, U. Genth, and T. Seiler, "Determination of excimer laser ablation rate of the human cornea using in vivo Scheimpflug videography," Invest. Ophth. Vis. Sci. **37**, 42–46 (1996).

21. M. S. Kitai, V. L. Popkov, V. A. Semshishen, and A. A. Kharizov, "The physics of UV laser cornea ablation," IEEE J. Quant.Elect. **27**, 302–307 (1991).

22. R. R. Krueger and S. L. Trokel, "Quantitation of corneal ablation by ultraviolet laser light," Arch. Ophthalmol. **103**, 1741–1742 (1985).

23. P. P. Van Saarloos and I. J. Constable, "Bovine corneal stroma ablation rate with 193-nm excimer laser radiation: Quantitative measurement," Refract. Corneal Surg. **6**, 424–429 (1990).

24. Food and Drug Administration. *FDA-Approved Lasers for LASIK*. [updated 6 March 2008; cited 24 July 2008]. Available from http://www.fda.gov/cdrh/LASIK/lasers.htm.

25. P. J. Dougherty, K. L. Wellish, and R. K. Maloney, "Excimer laser ablation rate and corneal hydration," Am. J. of Ophthalmol. **118**, 169–176 (1994).

26. M. H. Feltham and F. Stapleton, "The effect of water content on the 193 nm excimer laser ablation," Clin. Exp. Ophthalmol. **30**, 99–103 (2002).

27. W.-S. Kim and J.-M. Jo, "Corneal hydration affects ablation during laser in situ keratomileusis surgery," Cornea **20**, 394–397 (2001).

28. B. T. Fisher, K. A. Masiello, M. H. Goldstein, and D. W. Hahn, "Assessment of transient changes in corneal hydration using confocal Raman spectroscopy," Cornea **22**, 363–370 (2003).

29. J. R. Jiménez, R. G. Anera, L. Jiménez del Barco, and E. Hita, "Influence of laser polarization on ocular refractive parameters after refractive surgery," Opt. Lett. **29**, 962–964 (2004).

30. J. R. Jiménez, R. G. Anera, L. Jiménez del Barco, E. Hita, and F Pérez-Ocón, "Correction factor for ablation algorithms used in corneal refractive surgery with gaussian-profile beams," Opt. Express **13**, 336–343 (2005).

31. J. R. Jiménez, F. Rodriquez-Marin, R. G. Anera, and L. Jiménez, "Deviations of Lambert-Beer's law affect corneal refractive parameters after refractive surgery," Opt. Express **14**, 5411–5417 (2006).

32. R. G. Anera, J. R. Jimenez, L. Jimenez del Barco, and E. Hita, "Changes in corneal asphericity after laser refractive surgery, including reflection losses and nonnormal incidence upon the anterior cornea," Opt. Lett. **28**, 417–419 (2003).

33. R. G. Anera, C. Villa, J. R. Jimenez, R. Gutierrez, and L. Jimenez del Barco, "Differences between real and predicted corneal shapes after aspherical corneal ablation," Appl. Optics **44**, 4528–4532 (2005).

34. USA Eyes. *The Odds You Will See 20/20 After Lasik, All-Laser Lasik, PRK, LASEK, Epi-Lasik, CK, P-IOL, RLE, etc*. [updated 8 April 2006; cited 24 July 2008]. Available from http://www.usaeyes.org/faq/subjects/odds.htm.

35. T. Moller-Pedersen, H. D. Cavanagh, W. M. Petroll, and J. V. Jester, "Stromal wound healing explains refractive instability and haze development after photorefractive keratectomy," Ophthalmology **107**, 1235–1245 (2000).

36. J. V. Jester, T. Moller-Pedersen, J. Huang, C. M. Sax, W. T. Kays, H. D. Cavanagh, W. M. Petroll, and J. Piatigorsky, "The cellular basis of corneal transparency: Evidence for corneal crystallins," J. Cell Sci. **112**, 613–622 (1999).

37. K. B. Kim, L. M. Shanyfelt, and D. W. Hahn, "Analysis of dense-medium light scattering with applications to corneal tissue: Experiments and Monte Carlo simulations," J. Opt. Soc. Am. A. **23**, 9–21 (2006).

38. USA Eyes. *Enhancement Surgery For Lasik, PRK, LASEK, Epi-Lasik, CK, etc.* [updated 8 April 2006; cited 24 July 2008]. Available from http://www.usaeyes.org/faq/subjects/enhancement.htm.

39. R. Srinivasan, "Kinetics of the ablative photocomposition of organic polymers in the far ultraviolet (193 nm)," J. Vac. Sci. Technol. **1**, 923–926 (1983).

40. G. R. Van Hecke and K. K. Karukstis, *A Guide to Lasers in Chemistry* (Jones and Bartlett Publishers, Boston, 1998).

41. J. H. Brannon, J. R. Lankard, A. I. Baise, F. Burns, and J. Kaufman, "Excimer laser etching of polyimide," J. Appl. Phys. **58**, 2036–2043 (1985).

42. G. Gorodetsky, T. G. Kazyaka, R. L. Melcher, and R. Srinivasan, "Calorimetric and acoustic study of ultraviolet-laser ablation of polymers," Appl. Phys. Lett. **46**, 828–830 (1985).

43. G. M. Davis and M. C. Gower, "Excimer laser lithography—intensity-dependent resist damage," IEEE Electr. Device L. **7**, 543–545 (1986).

44. P. E. Dyer and J. Sidhu, "Excimer laser ablation and thermal coupling efficiency to polymer-films," Appl. Phys. **57**, 1420–1422 (1985).

45. N. Bityurin, B.S. Luk'yanchuk, M.H. Hong, and T.C. Chong, "Models for laser ablation of polymers," Chem. Rev. **103**, 519–552 (2003).

46. T. Lippert and J. T. Dickinson, "Chemical and spectroscopic aspects of polymer ablation: Special features and novel directions," Chem. Rev. **103**, 453–485 (2007).

47. M. Prasad, P. F. Conforti, and B. J. Garrison, "Coupled molecular dynamics—Monte Carlo model to study the role of chemical processes during laser ablation of polymeric materials," The J. Chem. Phys. **127**, 1–13 (2007).

48. C. Dorronsoro, D. Cano, J. Merayo-Lloves, and S. Marco, "Experiments on PMMA models to predict the impact of corneal refractive surgery on corneal shape," Opt. Express **14**, 6142–6156 (2006).

49. R. Srinivasan and B. Braren, "Ultraviolet laser ablation of organic polymers," Chem. Rev. **89**, 1303–1316 (1989).

50. B. T. Fisher and D. W. Hahn, "Determination of excimer laser ablation rates of corneal tissue using wax impressions of ablation crater and white-light interferometry," Ophthal. Sur. La. Im. **35**, 41–51 (2004).

51. D. N. Nikosgosyan and H. Gorner, "Laser induced photodecomposition of amino acids and peptides: Extrapolation to corneal collagen," IEEE J. Sel. Top. Quant. **5**, 1107–1115 (1999).

52. G. Paltauf and P. E. Dyer, "Photomechanical processes and effects in ablation," Chem. Rev. **103**, 577–644 (2003).

53. F. Manns, P. Milne, and J. M. Parel, "Ultraviolet corneal photoablation," J. Refract. Surg. **18**, 1–5 (2002).

54. X. H. Hu, Q. Fang, M. J. Cariveau, X. Pan, and G. W. Kalmus, "Mechanism study of porcine skin ablation by nanosecond laser pulses at 1064, 532, 266, and 213 nm," IEEE J. Sel. Top. Quant. **37**, 322–328 (2001).

55. G. H. Pettit and R. Sauerbrey, "Pulsed ultraviolet laser ablation," Appl. Phys. A **56**, 51–63 (1993).

56. V. N. Tokarev, J. G. Lunney, W. Marine, and M. Sentis, "Analytical thermal model of ultraviolet laser ablation with single-photon absorption in the plume," J. Appl. Phys. **78**, 1241–1246 (1995).

57. E. Sutcliffe and R. Srinivasan, "Dynamics of UV laser ablation of organic polymer surfaces," J. Appl. Phys. **60**, 3315–3322 (1986).

58. R. Srinivasan, B. Braren, D. E. Seeger, and R. W. Dreyfus, "Photochemical cleavage of a polymeric solid—details of the ultraviolet-laser ablation of poly(methyl metacrylate) at 193-nm and 248-nm," Macromolecules **19**, 916–921 (1986).

59. B. Lukyanchuk, N. Bityurin, S. Anisimov, N Arnold, and D. Bauerle, "The role of excited species in ultraviolet-laser materials ablation III. Non-stationary ablation of organic polymers," Appl. Phys. A **62**, 397–401 (1996).

60. P. T. Staveteig and J. T. Walsh, Jr, "Dynamic 193-nm optical properties of water," Appl. Optics **35**, 3392–3402 (1996).

61. M. N. Ediger, G. H. Pettit, R. P Weiblinger, and C. H Chen, "Transmission of corneal collagen during ArF excimer laser ablation," Laser. Surg.Med. **13**, 204–210 (1993).

62. M. N. Ediger, G. H. Pettit, and D.W. Hahn, "Enhanced ArF laser-absorption in a collagen target under ablative conditions," Laser. Surg.Med. **15**, 107–111 (1994).

63. G. H. Pettit and M. N. Ediger, "Corneal-tissue absorption coefficients for 193- and 213-nm ultraviolet radiation," Appl. Optics **35**, 3386–3391 (1996).

64. A. D. Yablon, N. S. Nishioka, B. B. Mikic, and V. Venugopalan, "Measurements of tissue absorption coefficients by use of interferometric photothermal spectroscopy," Appl. Optics **38**, 1259–1272 (1999).

65. C. R. Munnerlyn, M. E. Arnoldussen, A. L. Munnerlyn, and B. A. Logan, "Theory concerning the ablation of corneal tissue with large-area, 193-nm excimer laser beams," J. Biomed. Opt. **11**, 32–64 (2006).

66. M. Ishihara, T. Arai, S. Sato, Y. Morimoto, M. Obara, and M. Kikuchi, "Measurement of the surface temperature of the cornea during ArF excimer laser ablation by thermal radiometry with a 15-nanosecond time response," Laser Surg. Med. **30**, 54–59 (2002).

67. J. Noack, R. Tonnies, K. Hohla, R. Birngruber, and A. Vogel, "Influence of ablation plume dynamics on the formation of central islands in excimer laser photorefractive keratectomy," Ophthalmology **104**, 823–830 (1997).

68. D. W. Hahn, M. N. Ediger, and G. H. Pettit, "Dynamics of ablation plume particles generated during excimer laser corneal ablation," Laser. Surg.Med. **16**, 384–389 (1995).

69. C. A. Puliafito, D. Stern, R. R. Krueger, and E. R. Mandel, "High-speed photography of excimer laser ablation of the cornea," Arch. Ophthalmol. **105**, 1255–1259 (1987).

70. K. Nahen and A. Vogel, "Plume dynamics and shielding by the ablation plume during Er:YAG laser ablation," J. Biomed. Opt. **7**, 165–178 (2002).

71. A. Thorne, U. Litzen, and S. Johansson, *Spectrophysics: Principles and Applications* (Springer, New York, 1999).

72. HyperPhysics. *Michelson Interferometry.* [updated 2006; cited 24 July 2008]. Available from http://hyperphysics.phy-astr.gsu.edu/hbase/phyopt/michel.html.

73. Zygo Corporation. *NewView 100 Operation Manual OMP-0348K*. (April 1996).

74. G. Kahle, H. Stadter, T. Seiler, and J. Wollensak, "Gas chromatographic and mass spectroscopic analysis of excimer and erbium: yttrium aluminum garnet laser-ablated human cornea," Invest. Ophth. Vis. Sci. **33**, 2180–2184 (1992).

75. O. Kermani, H. J. Koort, E. Roth, and M. U. Dardenne, "Mass spectroscopic analysis of excimer laser ablated material from human corneal tissue," J. Cataract Refr. Surg. **14**, 638–641 (1988).

76. C. Grivas, H. Niino, and A. Yabe, "Laser ablation mechanism and plume dynamics of polyarylsulfone films studied by laser ionization time-of-flight mass spectrometry," Appl. Phys. A **69**, S159–S163 (1999).

77. M. Tsunekawa, S. Nishio, and H. Sato, "Multiphoton ionization mass spectrometric study of laser ablation of polymethylmethacrylate and polystyrene at 308 nm," Jpn. J. Appl. Phys. Vol. **34**, 218–225 (1995).

78. S. G. Hansen, "Study of ultraviolet-laser ablation products of several polymers using time-of-flight mass spectroscopy," J. Appl. Phys. **66**, 1411–1422 (1989).

79. G. H. Pettit and M. N. Ediger, "Pump/Probe transmission measurements of corneal tissue during excimer laser ablation," Laser Surg. Med.**13**, 363–367 (1993).

80. E. Rebollar, G. Bounos, M. Ouija, C. Domingo, and M. Castillejo, "Influence of polymer molecular weight on the UV ablation of doped poly(methyl methacrylate)," Appl. Surf. Sci. **88**, 1203–1210 (2005).

81. V. Venugopalan, N. S. Nishioka, and B. B. Mikic, "The thermodynamic response of soft biological tissue to pulsed ultraviolet laser irradiation," Biophys. J. **69**, 1259–1271 (1995).

82. M. Ishihara, T. Arai, S. Sato, Y. Morimoto, M. Obara, and M. Kikuchi, "Nanosecond-time-response temperature measurements using radiation thermometry during 193 nm and 247 nm pulsed light irradiation: Comparison of corneal surface temperature histories," Proc. SPIE **4257**, 298–302 (2001).

83. M. Gerstmann, A. Sagi, A. Avidor-Zehavi, A. Katzir, and S. Akselrod, "Model simulation of biological damage in tissue exposed to CO_2 laser irradiation," Opt. Eng. **32**, 291–297 (1993).

84. V. Venugopalan, N. S. Nishioka, and B. B. Mikic, "The effect of CO_2 laser pulse repetition rate on tissue ablation rate and thermal damage," IEEE T. Bio.-Med. Eng. **38**, 1049–1052 (1991).

85. A. Vogel, J. Noack, G. Huttman, and G. Paltauf, "Mechanisms of femtosecond laser nanosurgery of cells and tissues," Appl. Phys. B **81**, 1015–1047 (2005).

BIOGRAPHICAL SKETCH

Leia Shanyfelt was born in Florida, in 1978. She was raised in Florida, graduating from Citrus High School in 1996. She graduated from the University of Florida in 2001, with her Master of Science degree in mechanical engineering, specializing in thermal science. Her thesis topic used experimental and theoretical models of light scattering in dense structures to better understand haze formation in human eyes resulting from photorefractive surgery. She then moved to South Carolina to work at the Department of Energy's Savannah River Site. There, she was employed by Bechtel, a private construction firm, as a design engineer. She returned to the University of Florida, in 2005. In 2008, she received her PhD under the advisement of Dr. David Hahn. Leia is the daughter of Phillip and Nancy Coffey and the wife of Daniel Shanyfelt.